UDK 669+666+678+53

ISSN 1580-2949
MTAEC9, 44(2)49–102(2010)

MATER. TEHNOL.	LETNIK VOLUME 44	ŠTEV. NO. 2	STR. P. 49–102	LJUBLJANA SLOVENIJA	MAR.–APR. 2010

VSEBINA – CONTENTS

PREGLEDNI ČLANKI – REVIEW ARTICLES

IZVIRNI ZNANSTVENI ČLANKI – ORIGINAL SCIENTIFIC ARTICLES

STROKOVNI ČLANKI – PROFESSIONAL ARTICLES

UDK 541.64.057:66 ISSN 1580-2949
Pregledni članek/Review article MTAEC9, 44(2)51(2010)

NEKAJ MOŽNIH POSTOPKOV IZDELAVE HIDROFOBNIH IN OLEOFOBNIH POLIMERNIH MEMBRAM TER NJIHOVA UPORABA

HYDROPHOBIC AND OLEPHOBIC MEMBRANE USAGE AND PRODUCTION PROCESSES

Darko Drev[1], **Jože Panjan**[2]
[1]Inštitut za vode RS, Hajdrihova 28c, 1000 Ljubljana, Slovenia
[2]Univerza v Ljubljani, Fakulteta za gradbeništvo in geodezijo, Jamova ul. 2, 1000 Ljubljana, Slovenia
darko.drev@gmail.com

Prejem rokopisa – received: 2009-09-17; sprejem za objavo – accepted for publication: 2009-12-07

Pri nekaterih vrstah uporabe so zelo zaželene hidrofobne in oleofobne lastnosti membran. To daje takšnim membranam odločilno prednost pred drugimi materiali. Na podlagi prikazanega postopka izdelave PTFE-membran je razvidno, da njihove pore ne morejo biti manjše od pribl. 0,01µm. To pomeni, da tovrstne membrane ne moremo uporabljati pri zelo finih filtracijah (ultrafiltracija, reverzna osmoza). Poleg politetrafluoretilena imajo zelo izražene hidrofobne in oleofobne lastnosti tudi polisiloksani. Tako kot obstajajo omejitve pri izdelavi PTFE-membran, so tudi pri polisiloksanih (silikonih). Polisiloksanskih membran žal ni mogoče izdelati po klasičnem postopku inverzije faz. Kot zelo grobi nadomestki za drage PTFE-membrane so se uveljavili tudi razni oleofobni in hiodrofobni premazi na osnovi mehanskih pen in emulzij. V obeh primerih mora biti v osnovno matrico vgrajen ustrezni hidrofobni in oleofobni material (na primer fluorkarbon). Odprtost strukture in velikost por pri tovrstnih materialih še zdaleč ni primerljiva s PTFE-membranami. V tem članku je opisan nov postopek izdelave asimetričnih polisiloksanskih membran, ki je osnova za rešitev nastalega problema. Na podlagi takšnega postopka bi bilo morda možno izdelati tudi zelo fine asimetrične polisiloksanske membrane, ki bi imele veliko primerjalno prednost pred vsemi drugimi polimernimi materiali.

Ključne besede: membrana, oleofobno, hidrofobno, filtracija

Hydrophobic and oleophobic membrane properties are very desirable for certain filtration process, giving them an advantage over other materials. A polytetrafluoroethylene (PTFE) membrane production process is presented, revealing a minimum membrane pore size of approximately 0.01µm. It follows that such membranes are not suitable for very fine filtration uses (ultrafiltration, reverse osmosis). In addition to PTFE, polysiloxanes are also marked by enhanced hydrophobic and oleophobic properties. However, polysiloxane membranes suffer from severe production process limitations as their production has thus far not been possible via classical phase inversion processes. Thus, several oleophobic and hydrophobic coatings based on mechanic foams and emulsions have been introduced as a crude replacement for expensive PTFE membranes. These require the introduction of a suitable hydrophobic or oleophobic material such as fluorocarbon into the polymer matrix. However, the degree of the resulting membrane opennes and pore size are not comparable to those of PTFE membranes. In this paper, I present a new production process for asymetric polysiloxane membranes that provides the basis of a solution to this problem. This process could allow the creation of very fine asymetric polysiloxane membranes that would have a large comparative advantage to polymers existing today.

Keywords: membrane, oleofobic, hydrophobic, filtration

1 UVOD

C. E. Reid in E. J.Breton sta leta 1959 objavila članek o izdelavi in uporabi polimernih membran po postopku inverzije faz [13]. V njem sta objavila odkritje, da se lahko uspešno izločajo elektroliti iz vodnih raztopin z membrano iz acetata celuloze. Po tem postopku se tudi danes izdelujejo zelo fine membrane za ultrafiltracijo, nanofiltracijo in reverzno osmozo. Tehnologija izdelave PTFE–membran, ki so na trgu poznane kot membrane Gore-tex, izvira iz patenta W. L. Gore and Associates, Inc., Neweark, iz leta 1971 [5]. Pozneje so se na trgu pojavile nekatere podobne PTFE–membrane ter razni nadomestki na osnovi suspenzij, mehanskih pen, foto polimerizacije, radioaktivnega obsevanja folij, itd. Vendar pa do sedaj z nobenim drugim postopkom in materialom niso uspeli izdelati membran s podobnimi karakteristikami, kot jih imajo PTFE–membrane.

V članku obravnavamo konkretne preizkuse izdelave hidrofobnih in oleofobnih membran, ki smo jih izvedli na podlagi razpoložljivih podatkov (patenti, literatura, podatki proizvajalcev surovin, podatki proizvajalcev tehnološke opreme, izdelki na trgu, itd.) in lastnih zamisli. K inovativnim prispevkom pri tem lahko prištejemo nov način kaširanja PTFE–membran in folij na tekstilno podlogo [8] ter postopek izdelave asimetrične mikroporozne polisiloksanske membrane [9]. Ker postopka nista bila zaščitena kot EU– ali US–patenta, se lahko prosto uporabljata zunaj Slovenije. Predpostavljamo, da pri laminiranju PTFE–membran uporabljajo podobno tehnologijo, kot je opisana v tem članku. Asimetričnih polisiloksanskih membran pa še ni na trgu, zato sklepamo, da teh raziskav še ni nihče implementiral v praksi.

Polimerne hidrofobne in ofeofobne membrane so najpomembnejše za mikrofiltracijo. Razlog za to je velika odprtost strukture ter hidrofobne in oleofobne lastnosti. V zadnjem desetletju so postale nepogrešljive v oblačilni in obutveni industriji. Veliko se uporabljajo tudi pri industrijskem odpraševanju, tekočinski filtraciji, bioloških čistilnih napravah itd. [1,2,14]. Zaradi relativno velikih por pa niso primerne za fino filtracijo (ultrafiltracija, nanofiltracija, reverzna osmoza).

Pri izbiri materialov za izdelavo polimernih membran je pomembno vedeti, kakšno vrsto membrane želimo izdelati, ter za kaj jo bomo uporabljali. Iz PTFE ne moremo izdelati membrane po postopku inverzije faz, temveč po postopku biaksialnega raztegovanja folije. Tako ne dobimo zelo finih por, kot jih lahko na primer pri polivinilacetatni ali polisulfonski membrani. Vendar pa imajo PTFE-membrane zelo veliko odprtost površine ter hidrofobne in oleofobne lastnosti. Polimerne membrane so v večini primerov premalo mehansko stabilne, zato potrebujejo tudi ustrezen nosilni material [1,2,11]. PETF–membrane se največkrat laminirajo na različne tekstilne podloge [8].

Tabela 1: Prepustnost kisika pri različnih polimernih folijah [4]
Table 1: Oxygen permeability of different plastic films [4]

Polimerni sloj	Prepustnost 10^9 cm^3 cm/(s cm^2 kPa)
Dimetilsilikonska guma	45,01
Fluorsilikon	8,25
Nitrilna guma	6,37
Naravna guma	1,80
Butilna guma	0,105
Polistiren	0,090
Polietilen HD	0,075
Najlon 6	0,003
Polietilentereftalat	0,0014
Politetrafluoretilen	0,003

Posamezne polimerne folije imajo različne prepustnosti za različne pline, kar je prav tako pomembna lastnost pri izbiri materiala za membrano [3,4,10,12]. V **tabelah 1 in 2** so prikazane prepustnosti polimernih folij za kisik, ogljikov dioksid in vodno paro.

2 EKSPERIMENTALNI DEL

2.1 Mikroporozni sloji

Pri membranskih filtrih z mikroporoznimi sloji se formira mikroporozna plast neposredno na tekstilno podlago. Na tekstilni material se nanaša mikroporozna polimerna mehanska pena, ki se mora po nanosu ustrezno utrditi. Princip formiranja mehanske pene je relativno enostaven [6,7]: na specialnem stroju se pod tlakom umešava zrak v polimerno disperzijo. Nastane mehanska pena, podobna smetani za kavo. Kakovost in obstojnost mehanske pene je odvisna od gostote

Tabela 2: Prepustnost različnih polimernih folij za H_2O, O_2 in CO_2 pri 25 µm, 90 % RV in 38 °C (3)
Table 2: Permeability of different plastic films for H_2O, O_2 and CO_2 at 25 µm, 90 % RV and 38 °C

Folija	Prepustnost H_2O pare ($g/m^2 \times 24$ h)	Prepustnost O_2 (10^5 cm^3/m^2 24 h Pa) 25 µm	Prepustnost CO_2 10^5 cm^3/m^2 24 h Pa) 25 µm
PES	25–30	40–50	300-350
PC	77–93	4559	27351
Ionomer	25–35	6000–7000	6000–7000
EVA	50–60	11000–14000	40000–50000
Najlon 1,1	40–80	507	1925
CA	100–320	2000–3000	15 702
Regenerirana celuloza	5–15	677	987
Orientirani PS	70–150	4500–6000	13169
PVDC	1,5–5,0	8-25	51
MehčaniI PVC	15–40		
Trdi PVC	30–40	150–350	450–1000
Orientirani PE	7	2000–2500	7500–8500
PP	10–12	3748	10130
PE HD	5	1600–2000	30000–40000
PE LD	15–20	650–8500	30000–40000

Pojasnilo kratic:
PTFE = politetrafluoretilen
PES = poliester
EVA = etilvinilacetat
CA = celulozniacetat
PS = polisulfon
PVDC = polivinilidenklorid
PVC = polivinilklorid
PP = polipropilen
PE HD = visokomolekularni polietilen
PE LD = nizkomolekularni polietilen
Najlon 6, Najlon 11 = vrsti poliamida

disperzije, površinske napetosti, viskoznosti in drugih razmer pri delovanju stroja.

Postopek izdelave filter medijev na bazi tekstilne podlage in mikroporoznega polimernega sloja obsega naslednje tehnološke faze [11]:

- pripravo polimerne disperzije
- formiranje polimerne mehanske pene (**slika 1**)
- nanos polimerne mehanske pene na tekstilno podlago (**slika 2**)
- sušenje in kalandriranje (**slika 2**)
- utrjevanje (kondenzacija) polimernega nanosa (**slika 3**)

Na **sliki 4** je elektromikroskopski posnetek mikroporozne mehanske pene, ki je bila izdelana na podlagi navedene recepture in opisanega postopka.

Primer recepture za izdelavo mikroporoznih premazov:

- 400 mas. d. DICRYLAN FL
- 300 mas. d. DICRYLAN 7331
- 300 mas. d. DICRYLAN PMC
- 100 mas. d. Helizarinweiß RTN
- 100 mas. d. SCOTCHGARD FC 251
- 100 mas. d. DICRYLAN–STABILIZATOR FO

Vmešavanje zraka: 210 g/L
Sušenje: 70–110 °C
Kondenzacija: 150 °C

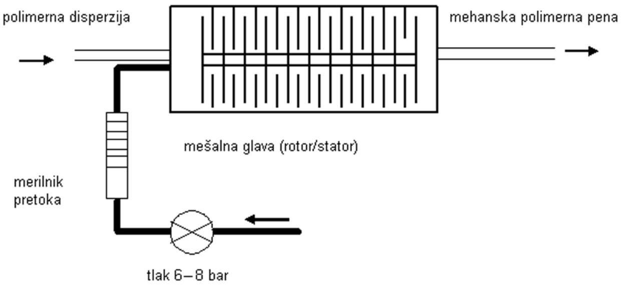

Slika 1: Shematski prikaz stroja za formiranje mehanske pene
Figure 1: Plan of the machine for mechanical foam

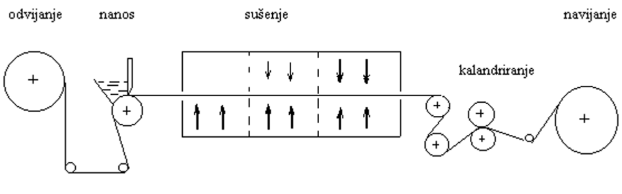

Slika 2: Nanos, sušenje in kalandriranje
Figure 2: Application, drying and calendering

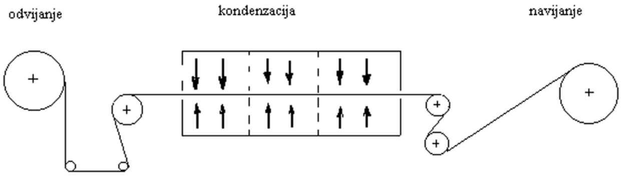

Slika 3: Kondenzacija
Figure 3: Condensation

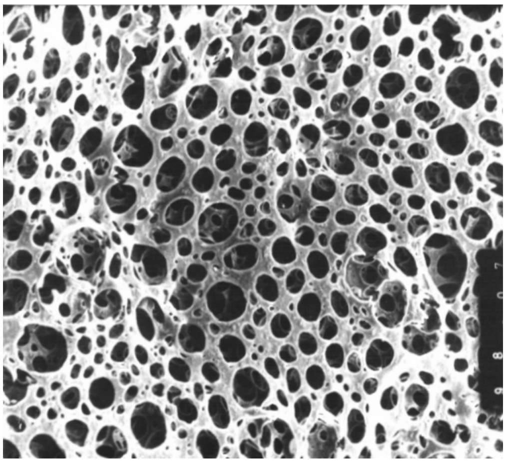

Slika 4: Fotografija mikroporozne mehanske pene, izdelane na osnovi poliakrilatne disperzije in fluorkarbona, povečava 190–kratna
Figure 4: Photo of microporous mechanical foam produced on the basis of polyacrylate dispersion and pluorocarbon, magnification 190–times

2.2. Izdelava PTFE–membran

Po tem postopku se izdelujejo membrane iz polimernega prahu PTFE (5). V patentu (W. L. Gore) so zaščiteni le osnovni principi, tehnološki postopek pa je obsežnejši in obsega naslednje faze:

- ovlaženje PTFE–prahu z ustreznim drsnim sredstvom;
- homogenizacija navlaženega materiala;
- oblikovanje predoblikovanca ustreznega profila z ekstrudiranjem;
- oblikovanje folije s kalandriranjem;
- biaksialno raztegovanje folije;
- odstranjevanje drsnega sredstva iz folije;
- utrditev folije.

V **tabeli 3** so prikazani materiali, ki smo jih uporabljali pri laboratorijskih in pilotnih preizkusih. Na **sliki 5** pa je prikazana kompletna tehnološka shema izdelave PTFE–membran.

Tabela 3: Uporabljene surovine za izdelavo PTFE–membran
Table 3: The raw materials used to manufacture PTFE–membranes

Proizvajalec	PTFE–prah	Drsno sredstvo
DU POINT Fluoropolymer Division	Teflon 669 N, 62 N, 636 N	
ICI Plastics Division	Fluon, CD1	
HOECHST AG Werk Gendorf	Hostaflon TF 2028, TF 2027, TF 2025	
SHELL Industrial Chemicals		Shellsol T, Shellsol K, Shell Sinarol II

V odvisnosti od raztegovanja folije so lahko pore v membrani manjše ali večje [5]. V **tabeli 4** so podane različne vrste Gore–tex–membran, ki so nastale zaradi različne stopnje raztegovanja. Postopek biaksialnega raztegovanja je najzahtevnejši del proizvodnje PTFE, saj je potrebna velika hitrost raztegovanja za dosego ustrezne poroznosti (podatki iz patenta).

Tabela 4: Prikaz strukture in lastnosti različnih Gore–tex–membran
Table 4: Illustration of the structure and properties of different Gore–tex–membranes

velikost por µm	debelina mm	poroznost %	pretok zraka* ml/ (min cm^2)	prestop vode** bar
0,02	0,080	50	2,3	24,00
0,20	0,060	78	72,0	2,75
0,45	0,080	84	190,0	1,35
1,00	0,080	91	370,0	0,48
3,00	0,025	95	930,0	0,13
5,00	0,025	95	3.870,0	0,07
10,00 – 15,00	0,013	98	11.300,0	0,03

* prepustnost zraka pri ΔP 0,01 bar
**minimalna prepustnost vode

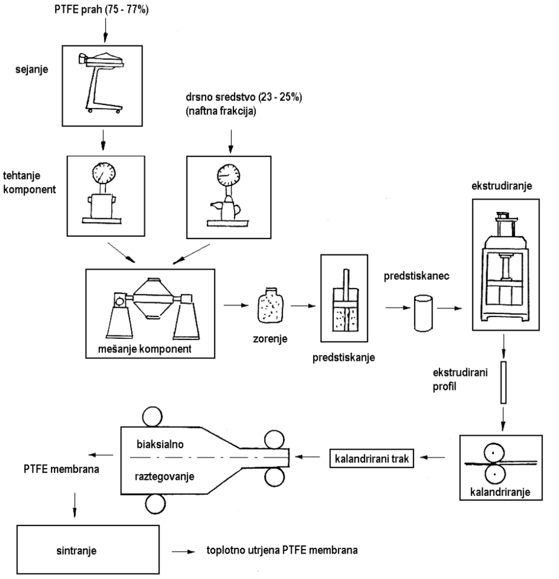

Slika 5: Postopek izdelave PTFE–membran
Figure 5: The process of manufacturing PTFE–membranes

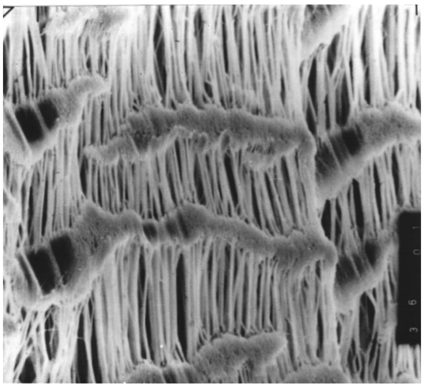

Slika 6: Naša PTFE–embrana, ki je raztegnjena samo v eni smeri (elekt. mikroskop, povečava 1900–kratna)
Figure 6: Our PTFE–membrane stretched in one direction only (elect. microscope, magnification 1900–times)

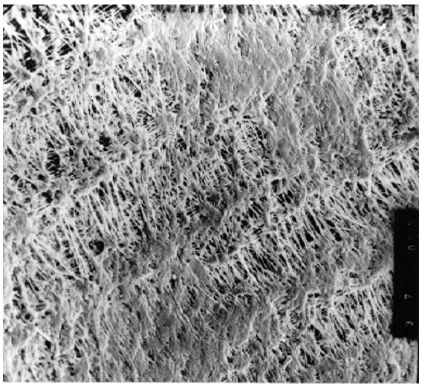

Slika 7: Gore-tex PTFE–membrana na PES–filcu 500 g/m^2, (elekt. mikroskop, povečava 1900–kratna)
Figure 7: Gore-tex PTFE–membrane felt in the PES 500 g/m^2, (elect. microscope, magnification 1900–times)

Na **sliki 6** je prikazan vzorec PTFE–membrane, ki smo jo raztegovali samo v eni smeri. Na **sliki 7** pa je prikazan vzorec Gore–tex–membrane, ki je laminiran na poliestrskem filcu. S slike je razvidno, da je membranska struktura delno zaprta z lepilom. To pomanjkljivost smo odpravili tako, da smo na tekstilna vlakna nanesli v zelo tanki plasti ustrezno lepilo in na tako pripravljeno podlogo laminirali PTFE–membrano [8].

2.3 Koagulacijski postopek izdelave polimernih membran

S spreminjanjem tehnoloških parametrov lahko izdelamo polimerne membrane z različnimi karakteristikami. Če polimerno raztopino nanesemo na površino ali na nekakšen drug način, formiramo plast polimerne raztopine (v obliki cevčice) tako, da je na eni strani izparevanje topila, na drugi pa neprepustna plast, se tvori koncentracijski gradient (**sliki 8 in 10**). Pri koagulaciji zato nastane asimetrična struktura membrane [1,2]. Na tistem delu, kjer je manj topila, nastanejo fine pore, na preostalem delu pa gobasta struktura.

Koagulacija se opravlja v netopilu za polimer, ki je istočasno dobro razredčilo za topilo, v katerem je raztopljen polimer (**slika 9**). Pogosto se uporablja kot koagulacijsko sredstvo voda ali vodna para. Za raztapljanje polimernih materialov pa se uporabljajo v glavnem organska topila.

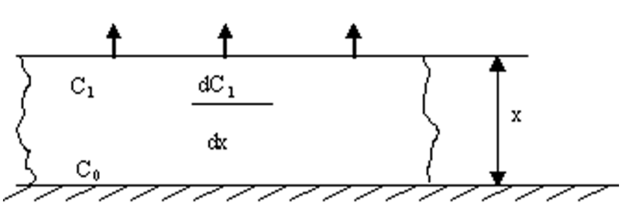

Slika 8: Izparevanje topila pri sloju tanke polimerne plasti
Figure 8: Evaporation in thin layer of polymer layers

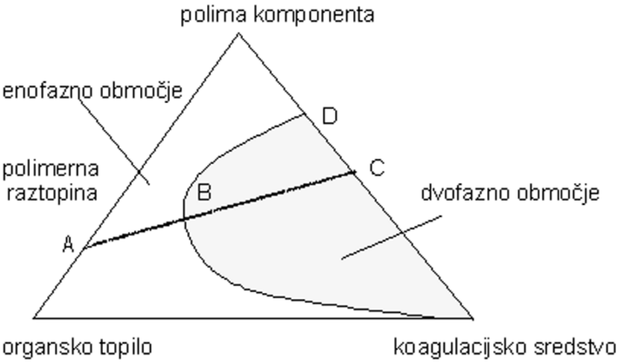

Slika 9: Diagram koagulacije polimerne membrane
Figure 9: Diagram of coagulation of polymeric membrane

V laboratorijskih razmerah smo izdelovali membrane po naslednjem postopku:

- priprava polimerne raztopine,
- nanašanje tankega sloja na ravno ploščo (stekleno),
- izparevanje pod kontroliranimi pogoji, da se tvori koncentracijski gradient,
- koagulacija (voda, organska topila),
- ekstrakcija organskih topil (voda, organska topila),
- sušenje v sušilniku.

Na **sliki 10** je shematsko prikazan laboratorijski postopek izdelave asimetričnih polimernih mambran, ki smo ga uporabljali pri laboratorijskih preizkusih.

2.4 Možni postopek izdelave asimetričnih polisiloksanskih membran

Po tem postopku formiramo asimetrično membrano z inverzijo faz. Mehansko stabilnost pa dosežemo kasneje z zamreženjem [9]. Zato je pomembno, da uporabljamo takšen postopek zamreženja, da se ne poškoduje asimetrična struktura membrane.

Polimerne verige imajo navadno od 200 do 800 enot. Končne skupine (X) so najpogostejše:

- (OH) za kondenzacijsko zamreženje
- (CH_2 = CH–) za adicijsko zamreženje
- (CH_3–) za peroksidno zamreženje

Kot reaktivne skupine (Y) se najpogosteje uporabljajo (CH_2 = CH–)– skupine. Zamreževalci morajo imeti najmanj tri funkcionalna mesta, preko katerih se opravlja zamreževanje. Najpogostejši zamreževalci so:

- metil–vodik–siloksani z več vodikovimi atomi v molekuli
- tri ali tetraalkoksilani
- triaminoalkilsilani

Reakcijo zamreženja sprožimo s katalizatorji, ki skrajšajo reakcijski čas. Kondenzacijsko zamreženje, ki se odvija pri sobni temperaturi ob prisotnosti zračne vlage, za naše namene ni primerno, ker nastanejo pri tem reakcijski produkti, ki lahko poškodujejo relativno nestabilno strukturo membrane. Pri tem postopku se uporabljajo linearni silikoni s končnimi skupinami –OH. Kot zamreževalci pa se uporabljajo:

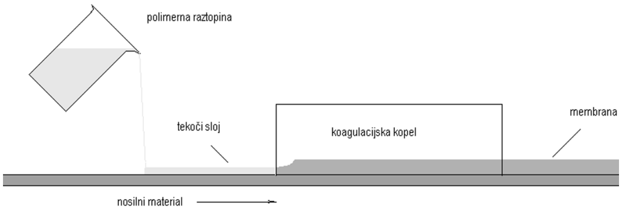

Slika 10: Shematski prikaz izdelave polimernih asimetričnih membran po postopku inverzije faz
Figure 10: Production of asymmetric polymeric membranes by phase inversion process

- H– silikoni
- estri silicijeve kisline

Kot katalizator se najpogosteje uporablja organski kompleks kositra, ki je raztopljen v ustreznem topilu. Kondenzacija poteka tako, da se odcepljajo vodik, voda in alkohol. Reakcijska hitrost je odvisna od reaktivnosti zamreževalca, katalizatorja in temperature. Pri temperaturi med 120 °C in 180 °C je čas zamreženja med 30 s in 3 min. Zamreženje poteka tudi pri sobni temperaturi, vendar pa je čas bistveno daljši (do 24 h).

Postopek peroksidnega zamreženja je najstarejši. Pri tem postopku je lahko veriga siloksan s CH_3 – končnimi skupinami ali pa s CH_2 = CH– stranskimi skupinami. Zamreževalec v tem primeru največkrat ni potreben, ker peroksidni katalizator aktivira CH_3 – skupino siloksanske verige in nastane preko nje zamreženje. Kot katalizatorji se najpogosteje uporabljajo različni peroksidi (benzoilperoksid).

Adicijski postopek je najprimernejši za dokončno utrditev relativno nestabilne strukture membrane. Pri tem postopku se uporabljajo linearni silikoni s končnimi vinilnimi skupinami (CH_2 = CH–). Zamreževalci imajo proste – H atome. Kot katalizatorji se uporabljajo čisti metali. Pri tem postopku ne nastanejo stranski produkti, ki bi lahko poškodovali membransko strukturo. Adicijsko zamreženje se začne pri temperaturi med 90 °C in 100 °C in se nato med 140 °C in 170 °C močno poveča. Reakcijska hitrost zamreženja je pri 150 °C od 15s do 30 s in pri 120 °C od 30s do 60 s.

Zamreženje se lahko doseže tudi radioaktivnim obsevanjem. Radikali, ki so potrebni za zamreženje, se namreč lahko dobijo tudi s pospešenimi elektroni. Takšen postopek je primeren predvsem pri kontinuirnem tehnološkem postopku zamreženja silikonske membrane.

Postopek zamreženja poteka po naslednjem mehanizmu:

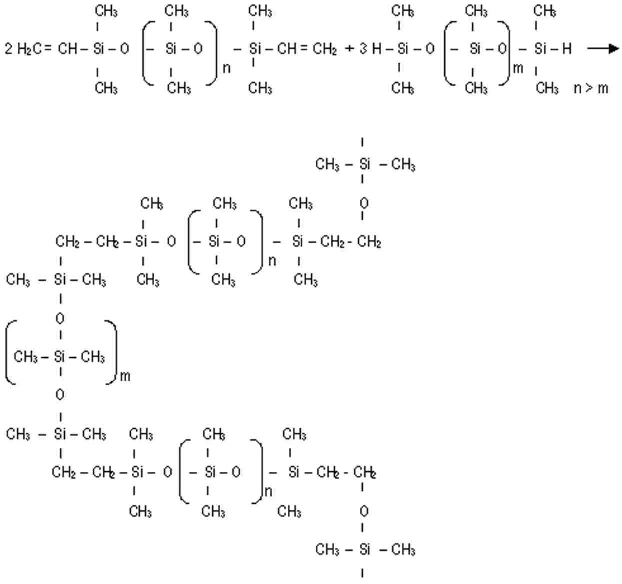

Tehnološki postopek izdelave sestavljajo naslednje tehnološke faze (9):

- tehtanje in mešanje komponent;
- razredčitev do primerne viskoznosti;
- odstranitev mehurčkov, če je raztopina preveč viskozna (vakumiranje);
- oblikovanje tankega sloja raztopine (ravna plast, formiranje cevnega profila);
- v laboratorijskih razmerah je najenostavnejše nanašanje z ustreznim nožem na stekleno ploščo;
- sušenje oziroma tvorba koncentracijskega gradienta (odvisno od vrste topil, debeline sloja, temperature itd.);
- koagulacija (inverzija faz), pri čemer nastanejo asimetrične polisiloksanske (silikonske) membrane;
- odvisna je od vrste polimernih materialov, topil v polimerni plasti ter vrste koagulacijskega sredstva;
- zamreženje nastale polimerne membrane;
- odvisno je od polimernih materialov in vrste zamreženja.

Preizkuse smo izvedli v laboratorijskih razmerah. Na ravno stekleno ploščo smo nanesli pribl.0,1 mm debel sloj polisiloksanske raztopine. Pri sobni temperaturi smo spreminjali čas sušenja v odvisnosti od razmerja topil metiletilketon/toluen. V primeru, da je topilo samo toluen, je čas sušenja bistveno daljši kot pri raztopini s precejšnjim deležem metiletilketona. Ko je nastal zaželen koncentracijski gradient, smo izvršili inverzijo faz v cikloheksanonu, ki je netopilo za polisiloksan. Cikloheksanon pa je dobro topilo za toluen in metiletilketon. Nastalo membrano smo nato osušili in s postopnim dvigovanjem temperature tudi utrdili z zamreženjem.

Veliko enostavneje lahko poteka postopek izdelave asimetričnih polisiloksanskih (silikonskih) membran pri izbiri drugih topil in vodi kot koagulacijskem sredstvu.

3 DISKUSIJA

Hidrofobne in oleofobne membrane imajo velike prednosti pred drugimi polimernimi in kompozitnimi membranami. Zaradi hidrofobnosti zadržujejo vodo tudi z relativno velikimi porami. Oleofobnost pa zagotavlja, da se na površini ne nabirajo razne nečistoče. Pri oblačilih se takšne membrane uporabljajo za vodo nepropustna oblačila, ki pa prepuščajo paro (Gore–tex). Pri filtrih za odpraševanje preprečujejo nabiranje oblog na filterskem mediju. Podobno velja tudi pri membranskih modulih [14], ki se uporabljajo pri komunalnih čistilnih napravah. Asimetrične membrane z zelo fino strukturo bi lahko imele celo vrsto novih aplikacij, ki jih drugi polimerni materiali ne morajo ponuditi. Te aplikacije bi lahko temeljile na zelo veliki prepustnosti plinov. Polisiloksanska folija brez membranske strukture je več kot 100–krat bolj prepustna za CO_2, O_2, N_2 kot druge. Če bi imela folija še asimetrično membransko strukturo, bi bila ta prepustnost še mnogo večja. Ker pa je polisiloksan hidrofoben, bi preprečil prepuščanje vode. Morda je možno na osnovi asimetrične polisiloksanske membrane izdelati umetne škrge, ki bi omogočale uporabo kisika iz vode in odvajanje ogljikovega dioksida v njo. Sposobnost prepuščanja plinov in zadržavanje vode, ki jo imajo hidrofobne membrane, bi lahko uporabili tudi v raznih drugih separacijskih postopkih. Če imajo membrane še oleofobne lastnosti, so še toliko bolj uporabne. Zato ni čudno, da so v zadnjem času začeli uporabljati membranske filterske module na osnovi PTFE, PVDT in še nekaterih drugih membran v kombinaciji z biološkimi čistilnimi napravami s suspendirano biomaso [14]. V tem primeru se doseže bistveno večja koncentracija biomase v bazenu in je zato potreben mnogo manjši volumen. Poleg tega ne potrebujemo bazena za kasnejše usedanje ter posebne stopnje sterilizacije. Membrana z velikostjo por 0,2 μm zadrži poleg velikih delcev tudi vse bakterije.

4 SKLEP

Glavna slabost sedanjih hidrofobnih in oleofobnih membran je njihova omejenost za zelo fino filtracijo. Razlog za to je v tehnologiji izdelave tovrstnih membran. Zelo fine membrane z veliko odprtostjo strukture se namreč izdelujejo po postopku inverzije faz. Po tem postopku žal ni možno izdelati PTFE–membrane. Tudi polisiloksanskih membran z asimetrično strukturo por še ni na trgu. Morda bo postopek, ki je opisan v tem članku, spodbudil proizvajalce membran, da bi razmišljali o predlagani tehnološki rešitvi.

5 REFERENCE

[1] Handbook of Industrial Membrane Technology, Edited by: Porter, M. C., 1990 William Andrew Publishing/Noyes

[2] Rösler, H. W., Membrantechnologie in der Prozessindustrie – Polymer membranwerkstoffe, 77, No5, 2005, Chemie Ingenier Technik

[3] Müller, K., Kunststoffflaschen und Verschlüssen-Messung und Modellierung der Stofftransportvorgänge, Ph. Thesis, Technische Universität München, 2003

[4] Zhang, H., The permeability characteristics of silicone ruber, society for the advancement of material and process engineering, 2006

[5] W. L. Gore and Associates Inc., Patent za izdelavo PTFE membran, 1972, Auslegenschrift 21 23 316

[6] Wilson, A. J., Foams, Physics, chemistry and structure, 1989

[7] Kornev, K. G., Neimark, A. N., Rozhkov, Foam in porous: thermodynamic and hydrodynamic peculiartis, Advances in colloid and interface science, 82 (**1999**)

[8] Drev, D., Nov način kaširanja PTFE membran in folij na tekstilno podlogo. Patent 9200375, z dne 18. 10. 1994. Ljubljana: Urad Republike Slovenije za varstvo industrijske lastnine, 1994

[9] Drev, D., Postopek izdelave asimetrične mikroporozne polisiloksanske membrane. Patent 21544. Ljubljana: Urad RS za intelektualno lastnino, 2005

[10] Zheng, J. P., Charbel, P. T., Kwok, H. S., Microporous silicon as a light trapping layer for photodiodes, Electrochemical and Solid-state Letters, 3 (**2000**) 7, 338–339

[11] Drev, D., Filtri za otprašivanje s mikroporoznim polimernim slojevima = Dust filtering with microporous polymer layers. Polimeri, 18 (**1997**) 5–6, 228–232

[12] United States Environmental Protection Agency, Office of water, membrane filtration guidance manual, EPA 815-R-06-009, November 2005

[13] Glate, J., The early history of reverse osmosis membrane development, Desalination, 117 (**1998**), 297–309

[14] Pinnekamp, J., Weitergehende Reinigung in kommunalen Kläranlagen mittels MBR-Technologie, Institut für Siedlungswasserwirtschaft der RWTH Aachen, oktober 2008

UDK 669:666:616.31:739
Pregledni članek/Review article

ISSN 1580-2949
MTAEC9, 44(2)59(2010)

LIQUID METAL/CERAMIC INTERFACES IN DENTAL PRACTICE AND JEWELLERY MANUFACTURING

STALJENE VMESNE POVRŠINE MED KOVINO IN KERAMIKO V ZOBOZDRAVSTVU IN PRI IZDELAVI NAKITA

Karlo T. Raić[1], Rebeka Rudolf[2], Aleksandar Todorović[3], Dragoslav Stamenković[3], Ivan Anžel[2]

[1]University of Belgrade, Faculty of Technology and Metallurgy, Karnegijeva 4, 11120 Belgrade, Serbia
[2]University of Maribor, Faculty of Mechanical Engineering, Smetanova 17, 2000 Maribor, Slovenia
[3]University of Belgrade, School of Dentistry, Clinic for Prosthodontics, 11000Belgrade, Serbia
karlo@tmf.bg.ac.rs

Prejem rokopisa – received: 2009-10-19; sprejem za objavo – accepted for publication: 2009-12-12

Metal-ceramic fusing has been the essential step in obtaining materials that benefit from both ceramic and metal constituents, i.e. where the combined properties of metal and ceramic layers are desirable. When considering fusing methods, soldering and active metal brazing are the most effective. These processes involve braze melting and flowing between the two pieces of material.

In the first part the phenomena occurring on the boundary between the ceramics and the active filler metal during the metal-ceramics joining are discussed. Three interconnected sub-processes are considered: (1) wetting of the ceramic surface, (2) chemical reactions at the interface and (3) diffusion with a moving interface. Then, the appearances at the grain boundary grooves of the ceramic surface are presented as phenomena on the catalytic surface.

In the second part, examples from dental practice and jewellery manufacturing are used for comparative analysis. Finally, we discuss the composition and properties of the soldering and brazing alloys used for dental practice and jewellery manufacturing.

Key words: metal-ceramic bonding, brazing, soldering, dentistry, jewellery

Zlitje kovine in keramike je temeljna stopnja za nastanek materiala, ki pridobi lastnosti obeh sestavnih delov, kjer je želena kombinacija lastnosti plasti kovine in keramike. Od metod zlitja sta lotanje in aktivno spajkanje najbolj učinkoviti. Procese sestavljata taljenje in pretok taline med obema materialoma.

V prvem delu razpravljamo o procesih na meji med keramiko in aktivnim polnilnim materialom med spajanjem kovine in keramike. Obravnavamo tri povezane procese: (1) omočljivost keramične površine, (2) kemične reakcije na vmesni površini in (3) difuzijo s premikajočo se mejno površino. Nato obravnavamo nastanek žlebov na mejah zrn na katalitični površini. V drugem delu uporabljamo primere iz dentalne prakse in izdelave nakita za primerjalno analizo. Na koncu je razprava o sestavi in lastnostih spajk in lotov, ki se uporabljajo v dentalni praksi in pri izdelavi nakita.

Ključne besede: vezava keramika-kovina, lotanje, spajkanje, zobozdravstvo, nakit

1 INTRODUCTION

The joining of metals to ceramics has been widely practiced in fabricating structural components to utilise the favourable characteristics of the engineering ceramics. Ceramics offer a huge array of mechanical, thermal and electrical properties.[1–5] These range from low thermal conduction in ceramics such as alumina, to high thermal conduction, e. g. diamond, and from low density electrical insulators to superconducting ceramics. Piezo-ceramics offer the almost unique ability to convert electrical energy into mechanical movement, and vice versa. Materials such as beta-alumina and zirconia, which exhibit ionic conduction, are used as sensors. These materials have found application in a wide range of industries, as well as in medicine. A common thread of the applications is that, at some point, the ceramic component interfaces with something else – another part of the component made from another material, usually metal. At this point, some kind of attachment or joint is required.

Soldering and active metal brazing are the most effective when considering fusing methods. This process basically involves braze melting and flowing between the two pieces of material. This is commonly referred to as 'wetting' and is absolutely critical – particularly when brazing ceramics. There are many materials that can be fused together to produce joints between materials – those that melt above ≈450 °C are classed as brazes, and materials melting below ≈450 °C are called solders.

There are two basic methods to encourage wetting: to apply something to the surface of the ceramics so that the braze will wet, or, to put something in the braze that will induce wetting. Surface treatments include metallisation, metal coating and metal hydride treatment, while braze modification involves a process known as active metal brazing. In either case the actual brazing operation takes place either in a controlled atmosphere, such as nitrogen or argon, or a vacuum better than 10^{-4} N m^{-2}.

During active brazing or soldering, samples are heated in a furnace to melt braze or solder which is placed between them. The active element in braze or solder, such as Ti, reacts chemically with the components to enable wetting and the formation of a strong bond. While active brazing can produce strong bonds, the high reactivity of the active metal requires the use of a vacuum furnace in an inert atmosphere to prevent oxidation. In addition, the high melting temperature of active brazes can lead to large thermal stresses on cooling, and fracture or de-bonding of the ceramic. Reactive solders reduce mismatch in thermal strains on cooling by lowering the process temperatures, but significant thermal stresses can still be present. Ideally, a strong metallic bond could be formed at/near room temperature, to avoid large thermal stresses between the components.

2 LIQUID METAL/CERAMIC INTERFACES

The phenomena occurring on liquid metal/ceramic interfaces are of the greatest importance for metal-ceramics joining techniques. An interdisciplinary task in which different fields of materials science must participate together with transport phenomena is shown in **Table 1**.[4–9] Therefore, in this paper, various approaches are explained which are necessary to treat transport phenomena on ceramic surfaces. In that sense, three steps are considered: (1) wetting of real ceramic surface, (2) chemical reactions at the interface and (3) diffusion with a moving interface.

Table 1: Aspects of investigation
Tabela 1: Teme raziskave

GENERAL VIEW	
– physical interface processes (reversible physical forces) – chemical interface processes (irreversible reactions) – phase diagrams – thermodynamic design	
transport phenomena (macro scale)	
(i) momentum ⇒ slow motion of liquid metal (ii) heat ⇒ inner/outer (unsteady and/or steady state transport) (iii) mass ⇒ diffusion with homo/heterogeneous chemical reaction (unsteady state phenomena)	
MICROSRUCTURAL VIEW	
ceramic	*liquid metal*
– surface structure, pores, cracks	– structure
– grain size	– composition
– non-bonded areas	
transport phenomena (micro scale)	
diffusivity: at the interface and into the bulk	
mass transfer during homo/heterogeneous appearances	
ATOMISTIC VIEW	
ceramic	*liquid metal*
(covalent or ionic binding)	(metallic bonding)
– phase boundary structure – bonding forces – interfacial energy – epitaxy	
basic equations of transport phenomena ⇔ electronic structure of metal/ceramics interface	

2.1 Wettability of real ceramic surface

In real systems, wettability is quite complex.[3–5,7–13] Even sometimes, something as simple as surface roughness can have complex and contradictory effects on wettability. Furthermore, chemical segregation in both the solid and liquid phases can have a huge effect on surface and interfacial energies and, hence, wettability. Also, it is difficult to estimate the extent of wetting because interfacial reactions change the wetting characteristics as time elapses. The relationship between wetting and interfacial reactions is not well understood, i.e. molten copper shows a high contact angle and low wettability against ceramics such as Si_3N_4, SiC and ZrO_2, although molten aluminium exhibits a low contact angle and high wettability against ceramics. On the other hand, the wetting of an MgO/Al system progresses through three phases: (I) vibratory phase or a chemically quasi-equilibrium phase; (II) constant phase and (III) decreasing phase or a chemically reactive phase. The rate in the decreasing of the contact angle in phase III depends on temperature and the bulk and/or surface properties of the ceramics, since the decrease is caused by the interfacial reactions.

Most wetting studies are based on the contact angle, which was first defined empirically by Young. This equation is a balance of the horizontal forces due to surface tensions acting upon a liquid drop in contact with a solid. Young observed that in most cases when a liquid is placed on a solid, the liquid remains as a drop with a definite contact angle between the liquid and solid phases (**Figure 1**).

The physico-chemical principles underlying wetting action are to be found in standard texts. If the liquid metal is (or is not) under pressure, it will come to rest on a real (porous and/or rough) ceramic surface in some position, determined by the advancing smooth surface-liquid metal contact angle and the shape of the pores in the surface. The surface of practical importance is usually grids formed of roughly spherical atom positions and/or grain boundaries.

One can start from the well known Young-Dupré Eq. (1) and the relationship given by Cassie and Baxter,[13] modified with two coefficients (h^{LS} and h^{SA}),[7–9] Eq. (2):

$$W_{ad} = \gamma_M \, (1 + \cos \varphi) \qquad (1)$$

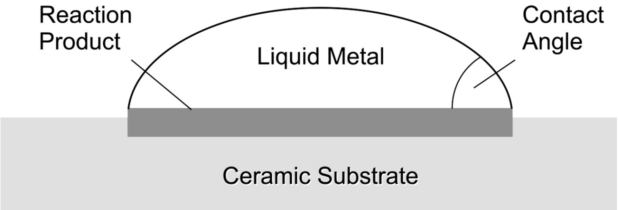

Figure 1: Sessile drop configurations assumed for the most reactive wetting models showing a complete reaction product layer
Slika 1: Konfiguracija premične kapljice, privzeta pri največ modelih reaktivnega omočenja, ki prikazuje plast reakcijskega produkta

$$\cos \varphi = h^{LS} f_1 \cos \alpha - h^{SA} f_2 \qquad (2)$$

where, W_{ad} – work of adhesion, J/m^2; γ_M – surface energy of the metal; φ: apparent contact angle (measured by sessile drop method); α – advancing (receding) contact angle (a not yet well understood parameter); f_1 – the total area of solid-liquid interface; f_2 – the total area of liquid-air (or furnace atmosphere) interface. Areas f_1 and f_2 can be derived from the value α and the dimensions of the grids formed of roughly spherical atom positions (lattice image) and/or surface grain boundaries. (f_1 and f_2 are the reflections of real or simulated surface image), h^{LS} – coefficient of net liquid-solid heterogeneity influence, h^{SA} – coefficient of net liquid-air (furnace atmosphere) heterogeneity influence.

The microstructural parameters that may have an influence on the properties of the metal/ceramic interface (reflected on h^{LS} and h^{SA}) are: (i) structure of the hetero-phase boundary, (ii) characteristic defects such as steps, faces and dislocations at or to the interfaces, (iii) possible chemical reactions, (iv) reaction products, (v) chemical gradients and segregation of impurities at the interface.[14]

While the wettability models predict whether wetting will occur for a given system, they do not predict the rate of wetting. Theoreticall modelling the spreading kinetics is complex. Even for nonreactive systems, modelling is complicated by surface irregularities, surface contamination, the formation of precursor films, and other surface anomalies. The spreading kinetics of reactive systems is further complicated by interfacial reactions at the solid-liquid and liquid-vapour interfaces (e.g., oxidation). The verification of a spreading mechanism is further hindered by a lack of experimental data. The interfacial reactions and the spreading kinetics are very rapid, making the collection of spreading kinetics and reaction-rate data challenging. Typical spreading kinetics for copper-titanium alloys on alumina is shown in **Figure 2.**[15]

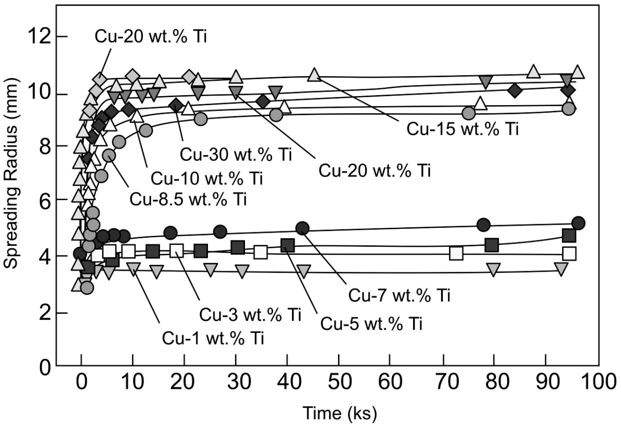

Figure 2: An example of rapid spreading kinetics in the spreading data for 1.2 g samples of copper-titanium alloys on alumina at 1120 °C[15]

Slika 2: Primer hitre kinetike o širjenju 1,2 g zlitine baker-titan na korundu pri 1120 °C[15]

2.2 Chemical reactions at liquid metal/ceramic interface

To explain the action of a polycrystalline surface it is assumed that reactant molecules of liquid metal are somehow changed, energized, or affected, to form intermediates in the regions close to the surface. In one theory the intermediate is viewed as an association of a reactant molecule with a region of the surface, in other words the molecules are somehow attached to the surface. In another theory molecules are thought to move down into the liquid metal close to the surface and be under the influence of surface forces. In this view the molecules are still, but are nevertheless modified. In still a third theory it is thought that an active complex, a free radical, is formed at the solid surface. This free radical then moves back into the main liquid stream, triggering a chain of reactions with fresh molecules before finally being destroyed. In the contrast with the two theories which consider the reaction to occur in the vicinity of the surface, this theory views the surface simply as a generator of free radicals, with the reaction occurring in the main body of liquid metal.[7–9]

On the other hand, in order to obtain knowledge of the reactivity, it is very important to respect the changes of the standard free energy for the formation of nitrides, carbides and oxides against temperature. From these thermodynamic data, when metal was placed in contact with nitride, carbide, or oxide ceramics, we are able to predict whether the metal could decompose the ceramic to form a nitride, carbide, or oxide phase.

2.3 Diffusion with a moving interface

The observed process, in conjunction with chemical reactions at a solid/liquid boundary, involves diffusion steps. One result of these transient processes is the motion of the boundary between the phases.[8] In the general situation, two phases are in contact as in **Figure 3**. The moving phase boundary is at $x = X$, and at this boundary Co and $C^* = C(X, t)$ represents the equilibrium

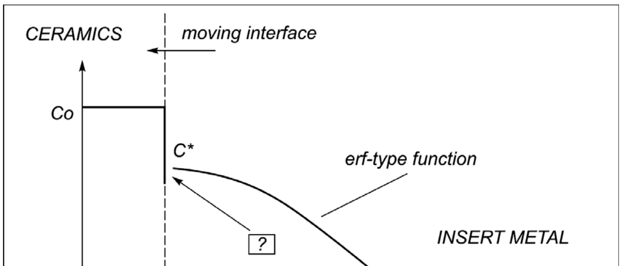

Figure 3: The concentration profile during transient diffusion[8]

Slika 3: Profil koncentracije med tranzientno difuzijo[8] concentration of, e.g. Al_2O_3, that coexist in ceramics and melted metal respectively at the temperature under consideration.

In the insert metal phase, Fick's second law applies:

$$dC/dt = D\, d^2C/dx^2,\ x > X \qquad (3)$$

where C is the Al_2O_3 concentration during transient diffusion, D the diffusion coefficient of the Al_2O_3 in melted metal, assumed to be independent of composition. The next condition is that the concentrations on either side of the interface are related by the equilibrium expression of the form:

$Co = KC^*$, where K is the partition ratio between the phases.

The material balance at the interface takes the form:

$$-D\,(dC/dx)_{x=X} = (C^* - Co)\; dX/dt \qquad (4)$$

Equ. 4 describes the locus of X with time. Relationship between Co and C^*:

$$\pi^{-0.5}\,[C^*/(C^* - Co)] = \beta \exp \beta^2 \operatorname{erf} \beta \qquad (5)$$

when

$$X = 2\beta\,(2D)^{0.5} \qquad (6)$$

is well known. The function of β, $\beta \exp \beta^2 \operatorname{erf} \beta$ may be evaluated from standard handbooks. So the D can be calculated if Co, C^*, X and t are measured. The illustrative calculated surface diffusivities for selected metal/alumina systems with groove widths (w) from 1 μm to 10 μm, are given in **Table 2**.

Table 2: Surface diffusivities for selected metal/alumina systems[10]
Tabela 2: Površinska difuzivnost za izbrane sisteme kovina/korund[10]

System	Temperature (K)	Surface Diffusion, wD ($m^3\ s^{-1}$)
Ni/Al_2O_3	1773	$4.4 \cdot 10^{-19}$
Au/Al_2O_3	1373	$1.8 \cdot 10^{-24}$
Cu/Al_2O_3	1423	$2.8 \cdot 10^{-22}$
Al/Al_2O_3	1373	$1.1 \cdot 10^{-19}$

Groove widths (w)

3 PHENOMENA AT GRAIN BOUNDARY GROOVES

Various processes may cause resistance to the overall reaction which occurs at the liquid-solid interface.[6,9] For an element of single groove between two grains (**Figure 4**) one can visualize: (i) *Liquid metal film resistance*. Reactants diffuse from the main body of the liquid metal to the exterior surface of the solid ceramic specimen. (ii) *Groove diffusion resistance*. Reactants move through the groove into the ceramic. Most of the reaction takes place within the groove. (iii) *Surface phenomena resistance*. At some point in their wandering reactant molecules become associated with the surface of the ceramic. They react to give products which are then released to the liquid phase within the groove. (iv) *Groove diffusion resistance for products*. Products then diffuse out of the groove. (v) *Liquid metal film resistance for products*. Products then move from the mouth of the groove into the main liquid stream. (vi) *Resistance to heat flow*. For reactions accompanied by heat release or absorption the flow of heat into or out of the reaction zone may not be fast enough to keep the liquid metal/solid ceramic specimen isothermal. If this happens, the specimen will cool or heat, strongly affecting the rate. Thus the heat transfer resistance across the liquid film or within the ceramic could influence the rate of reaction.

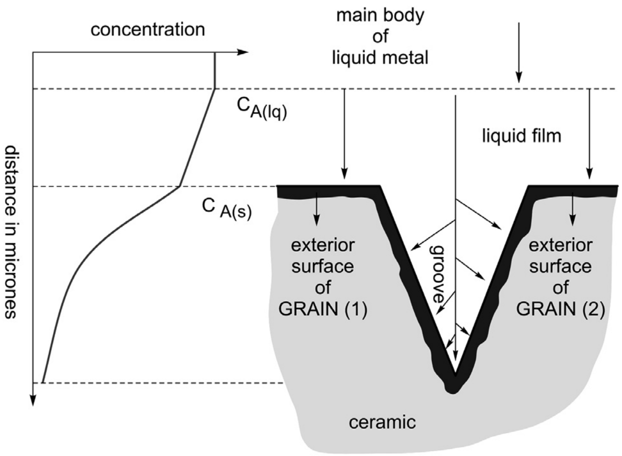

Figure 4: Phenomena around an element of single groove between two grains[9]
Slika 4: Pojavi okoli elementa enostavnega žleba med dvema zrnoma[9]

Usually, the reaction layer grew rapidly in the first minute. After approximately a few minutes, further increase in the reaction layer thickness becomes gradual and parabolic in time. In this way, the growth of product layer can be observed as a two-step process: an initial rapid thickening rate and a second parabolic rate, assumed to be diffusion controlled.[11]

Rapid initial layer growth can be related to the substrate/ceramics surface roughness. On the other hand, slower growth is assisted by capillarity. It is well known that capillary mass transport manifests itself with developing a grain boundary groove on the surface of a polycrystalline material wherever a boundary intersects an interface between a solid and another phase. Mass transport can involve several mechanisms: interfacial diffusion, volume diffusion on either side of the interface, and interfacial reaction (solution-precipitation). Depending on the physical characteristics of the system and groove size, one of these mechanisms will be rate controlling, resulting in characteristic groove shapes and growth kinetics.

The rate of reaction for the solid ceramic substrate/liquid metal sample may depend on:

1. Surface kinetics, which may change with development of the grain boundary grooves.
2. Grain boundary groove (GBG) resistance which sets up internal concentration gradients. The effects of

"volume diffusion" and "surface diffusion" on groove development are given in ref.[10]

3. Interface ΔT or temperature gradient at the liquid metal/solid ceramics interface. This is caused by heat release or absorption during reaction.
4. Film diffusion resistance or concentration gradients across the liquid metal film.

The surface kinetics and grain boundary groove (GBG) diffusion cannot be treated as steps in series as they enter the rate equation together. So for a 1st order reaction on a flat plate specimen, analysis gives the rate of reaction:

$$-r_{\mathrm{A}}''' = k'''C_{\mathrm{As}}\,\varepsilon \tag{7}$$

with

$$\varepsilon = (\tanh M_{\mathrm{T}})/M_{\mathrm{T}} \tag{8}$$

Where, ε: effectiveness factor = (actual reaction rate within GBG)/(rate if not slower by GBG diffusion), M_{T}: Thiele modulus, $M_{\mathrm{T}} = L(k'''/D_{\mathrm{eff}})^{1/2}$; D_{eff}: effective diffusion coefficient in porous solids [$\mathrm{m}^3_{\mathrm{liquid(metal)}}/\mathrm{m}_{\mathrm{solid(ceramic)}}$ s], L: characteristic size of ceramic sample/specimen, usually flat plate [L = (volume of sample)/(exterior surface) = thickness/2].

The "effective diffusivity" must be measured experimentally; it depends generally on the concentration of active species, temperature and on the groove structure. The actual mechanism for diffusion in grooves is complex, since the groove dimensions may be smaller than the mean path of the diffusing molecules.

We have no GBG resistance when: $M_{\mathrm{T}} < 0.4$ here $\varepsilon = 1$ and $-r_{\mathrm{A}}''' = k'''C_{\mathrm{As}}$; and strong GBG diffusion effects when: $M_{\mathrm{T}} > 4$ here $\varepsilon = 1/M_{\mathrm{T}}$ and $-r_{\mathrm{A}}''' = [(k'''\,D_{\mathrm{eff}})^{1/2}\,C_{\mathrm{As}}]/L$ (see **Figure 5**). The presented description is similar to the phenomena on a catalytic particle[6].

5 DENTAL PRACTICE

Dental materials may be classified as preventive materials, restorative materials or auxiliary materials.[16–21] Preventive materials include pit and fissure sealants, sealing agents that prevent leakage, materials that are used primarily for their antibacterial effects, and liners, bases, cements, etc. In some cases a preventive material may also serve as a restorative material that may be used for a short-term application.

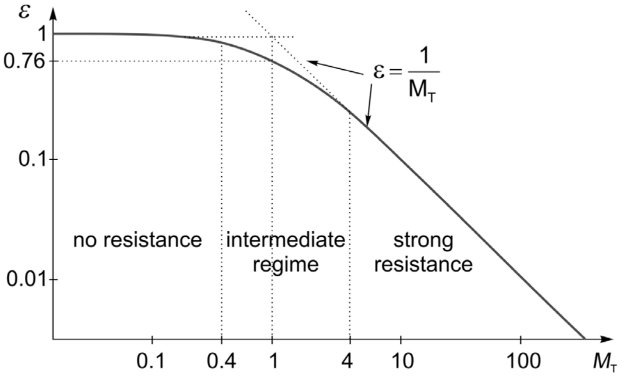

Figure 5: Effectiveness factor (ε) v. Thiele modulus (M_{T}) [6]
Slika 5: Faktor učinkovitosti (ε) v odvisnosti od modula Thiele (M_{T}) [6]

Restorative materials consist of all synthetic components that can be used to repair or replace tooth structure, including primers, bonding agents, liners, cement bases, amalgams, resin-based composites, hybrid ionomers, cast metals, metal-ceramics, ceramics, and denture polymers.[16,21] These materials can also be designed as controlled-delivery devices for the release of therapeutic or diagnostic agents. Restorative materials may be used for temporary, short term purposes (temporary cements, and temporary crown and bridge resins) or for longer-term application (dentin bonding, agents, inlays, onlays, crown, removable dentures, fixed dentures, and orthodontic appliances). These materials may further be classified as direct restorative materials or indirect restorative materials, depending on whether they are used –intraorally to fabricate restorations or prosthetic devices directly on the teeth or tissues or extraorally, in which materials are formed indirectly on casts or other replicas of the teeth and other tissues. An ideal restorative material would be biocompatible, bond with other visible tissues, exhibit properties similar to those of tooth enamel, dentin and other tissues, etc.

Auxiliary dental materials are substances which are used in the process of fabricating dental prostheses and appliances, but which do not become part of these devices. These include acid-etching solutions, impression materials, casting investments, gypsum cast and model materials, dental waxes, acrylic resin for impression and bleaching trays, acrylic resins for mouth guards and occlusion aids, and finishing and polishing abrasives.

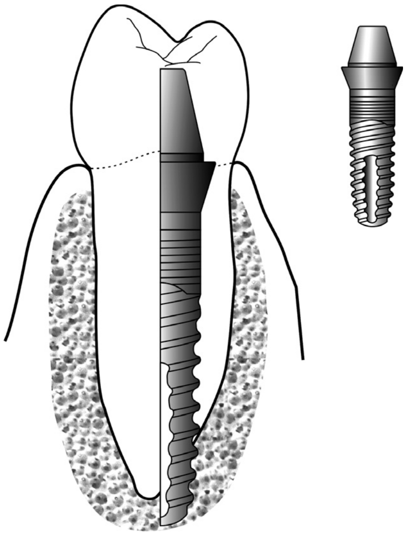

Figure 6: Schematic illustration of a cross-sectional view of a natural anterior tooth and supporting tissues (left) in combination with restorative dental materials (right)
Slika 6: Shematičen prikaz prereza naravnega zoba in nosilnega tkiva (levo) v kombinaciji s restavrativnim dentalnim materialom (desno)

Figure 6 is a schematic cross-section of a natural tooth and supporting bone and soft tissue (left) in combination with restorative dental materials (right). Under healthy conditions, the part of the tooth that extends out of adjacent gingival tissue is called a clinical crown, and that below the gingival tissue is called the tooth root. The crown of a tooth is covered with enamel and the root is covered with cementum, and it consists of dentin and tissue within one or more root canals.

The surface of implantable biomaterials is in direct contact with the host bone and soft tissue and it plays a critical role in determining its biocompatibility, functional compatibility, osteoinduction of bone and osseointegration of implants. The goal of regenerative therapy around orthopaedic and dental implant devices is to create a suitable environment in which the natural biological potential for functional regeneration of the bone and of the periodontal ligament can be stimulated and maximised. In implantology, wide arrays of biomaterials have been used so far with variable success rates.[17–20]

Metals are probably the oldest form of materials used for dental implants and the most common type of materials used so far. Superior fracture and fatigue resistance caused them to become the materials of choice in traditional load-bearing applications. A large spectrum of metals and alloys were used as endosseous implants, in orthopaedics, cranio-maxillofacial surgery and dentistry (**Table 3**). Gold-based alloys were among the first alloys to be used for implants, probably because these alloys were available in dentistry, but also because they promoted the fibrous interface with a bone, i.e. a distant osteogenesis with a short lifespan. Cobalt-chromium alloys were also developed and used as endosseous implants. However, the fundamental problem with these metals and alloys was the fibrous response which they promoted with the bone. By today's standards, none of these materials achieve osseointegration, probably because of their corrosion effected by the living tissue and the release of elements into the tissue. Today, these metals have largely been replaced by titanium and titanium alloys.

Bioceramics are a group of ceramics which are biologically active materials rich in calcium and phosphate. Hydroxyapatite and tricalcium phosphate are similar in composition to bone and teeth and can be used for the augmentation of alveolar ridges and filling bony defects. The various forms of bioceramics are Single crystals (Sapphire), Polycrystalline (Hydroxyapatite) Glass (Bioactive glass) Glass ceramics (Ceravital) Composites (Stainless steel reinforced Bioglass). There are about four types of bioceramics:

INERT: Attached by compact morphological fixation, e.g. Alumina, Carbon

POROUS: Attached by vascularization through pores, e.g. Porous Alumina.

SURFACE ACTIVE: Directly attach by chemical bonding with bone, e.g. Bioglass, Hydroxyapatite

RESORBABLE Designed to be slowly replaced by bone, e.g. Tricalcium Phosphate (TCP).

Ceramic coatings on dental implants, such as Calcium phosphates (hydroxyapatite- HA) appear to have better biological response than cpTi or Ti alloy alone, even if their clinical predictability remains controversial. Coatings seem to promote faster bone adaptation, higher bone implant strength, better osteoblast precursor activity, bone growth around dental implants and thus, bonding of the bone to the implants, i.e. osseointegration. HA coatings were considered highly because they enhance osseointegration, and they lead to the formation of more mineralised extracellular matrix (ECM) and to faster bone formation with respect to Ti substrates alone. The philosophy was that HA has an

Table 3: Example of dental and medical materials and their applications
Tabela 3: Primeri dentalnih in medicinskih materialov in njihove uporabe

MATERIALS	PRINCIPAL APLICATIONS
Metals and Alloys	
316 Stainless Steel-CP-Ti, Ti-Al-V, Ti-Al-Nb, Ti-13Nb-13Zr, Ti-Mo-Zr-Fe	Fracture fixation, stents, surgical instruments, bone and joint replacement, fracture fixation, dental implants, pacemaker, encapsulation
Co-Cr-Mo, Cr-Ni-Cr-Mo	Bone and joint replacement, dental implants, dental
Ni-Ti	Bone plates, stents, orthodontic wires
Gold Alloys	Dental restoration
Silver products	Antibacterial agents
Platinum and Pt-Ir	Electrodes
Hg-Ag-Sn amalgam	Dental restorations
Ceramics and Glasses	
Alumina	Joint replacement, dental implants, dental
Zirconia	Various parts of dental replacement
Calcium Phosphates	Bone repair and augmentation, surface coatings on metals
Bioactive glasses	Bone replacement
Porcelain	Dental restorations
Carbons	Heart valves, percutaneous devices, dental implants

advantage over smooth Ti surfaces having: (i) a bioactive surface versus an inert Ti surface; (ii) higher bond strength of the bone to the implant; and (iii) increased bone-to-implant contact. In spite of reports about overstressing, rapid bone-resorption adjacent to HA-coated implants, short-term survival rates (from 6 months to 6 years), or other causes of failures, there is still evidence of positive effects of HA coatings on osseointegration. Recently, other ceramic coatings, such as titanium nitride (TiN) and titanium carbide (TiC), have been proposed for implantology.

Most dental solders are either gold-based or silver-based alloys (**Table 4**). These alloys contain special elements such as tin to encourage a lower melting range and better flow. Gold-based solders are used primarily to solder cast alloys, whereas silver solders are used more in orthodontic applications. A variety of gold-based solders are available with various melting ranges to meet specific applications. The manufacturer of the cast alloys generally specifies the compatibility of solders with their alloys, and it is common for a manufacturer to offer both a series of dental casting alloys and compatible solders together. The strength, hardness, and corrosion of dental solders also depend on the composition. In general, solders with a higher melting range are stronger and harder than lower fusing solders.

5 JEWELLERY MANUFACTURING

The joining of many different materials is necessary in jewellery manufacture (the metal frames of rings, earrings, necklaces, etc. with different kinds of stone – precious, semi-precious, synthetic stones, coral, and pearls).

One of the phases in jewellery manufacturing is placing the precious stone into the metal frame. The stones are initially cut into the desired sizes and shapes, and then polished. The metal frame cast is ground and polished and the stones are joined to it by adhesives, soldering, or by mechanical clamping.[22] The attachment between stone and metal becomes weaker over time, because of elastic deformation. If the stone is soldered to the metal frame the joint between stone and metal is stronger. Different stones have different mechanical and physical properties and it is necessary to find an appropriate combination of solder components for each stone. For example, sapphire is an AlB_2BOB_3B mineral. Sapphire can be soldered after bonding or brazed without bonding. If the sapphire is brazed to titan without bonding, an alloy with 72 % Ag could be used. Diamond could be brazed to steel with L-Ag40Cd, L-Ag30Cr, or L-Ag20Si.

There are two groups of precious stones according to their price: first-order stones (diamond, ruby, sapphire and emerald) and second-order stones (aquamarine, topaz, zircon, onyx, quartz topaz, etc.). Many of them have similar chemical compositions, but their colours are different. The chemical composition of diamond is 99.95 % carbon. Emerald is a green mineral made of aluminium, and its colour comes from chrome or vanadium. Sapphire and ruby are minerals of AlB_2BOB_3B. Sapphire could have a blue colour from titan and iron, and violet from vanadium. Ruby could have a red colour from chrome or a chestnut colour from chrome and iron. The chemical compositions of stones could be very important when joining different kinds of stones. Many stones in the second group are very sensitive to heat. The result of heating the stone above its critical temperature could be

Table 4: Examples of solders used in dental practice
Tabela 4: Primeri lotov, ki se uporabljajo v dentalni praksi

Name of the solder, (Chemical composition, %)	Melting interval	Form of solder	Operation temperature	Colour	Application
Auroker L 1040 PF (79.0 % Au, 17.0 % Ag, 3.0 % Pt, 1.0 % Zn)	980 – 1040 °C	Strip (0.25× 1) mm	1040 °C	yellow	soldering metal-ceramics gold alloys
7 Aurodur HL 750 (73.0 % Au, 11.0 % Ag, 2.0 % Pt, 11.0 % Zn, 3.0 % Cu)	710 – 750 °C	Strip (0.25× 1) mm	750 °C	yellow	soldering dental alloys and alloys for metal-ceramics application
Auroker L 1060 (72.0 % Au, 5.0 % Ag, 12.0 % Pd, 2.0 % Zn, 8.0 % Cu, 1.0 % In)	1010 – 1070 °C	Strip (0.25× 1) mm	1060 °C	white	before firing ceramics
Midor L (58.0 % Au, 21.0 % Ag, 18.0 % Cu, 2.0 % Zn, 1.0 % Sn)	790 – 820 °C	Plate 0.33 mm Strip (0.25× 1) mm	820 °C	Light yellow	joining gold alloys for casting
Silopal L 890 (26.0 % Au, 16.0 % Ag, 30.0 % Cu, 15.0 % Pd, 13.0 % Zn)	850 – 890 °C	Strip (0.25× 1) mm	890 °C	white	soldering alloys based on the silver-palladium, before firing (baking) and the midfielder element for non-precious and precious metals
Witex lot (39.0 % Co, 22.0 % Cr, 19.0 % Ni, 10.0 % Fe, 5.0 % Si, 3.0 % Mo, 1.0 % B, 1.0 % V)		Wire Ø 1 mm	1180 °C	white	joining of materials for mobile prosthetic, CoCr alloys

a change in colour. Turquoise has a critical temperature at 250 °C, when its colour then changes from sky blue to green. At the critical temperature interval of tanzanite (from 400 °C to 500 °C), the nuances of yellow gradually disappear and the blue colour is intensified. Other precious stones can also express changes in their colours (quartz, topaz, amethyst, aquamarine, etc.). Therefore, it is very important during the joining of stones to the metal frame, that the stones are not heated above their critical temperatures.

The composition of brazing alloys used for jewellery applications is Au-Ag-Cu, with the addition of metals such as zinc and cadmium. Cadmium is very toxic, especially its vapour, during the melting process, and is replaced with non-toxic elements. Cadmium could be substituted with the following metals: tin (Sn), indium (In), gallium (Ga), and zinc (Zn). Also, some solders without cadmium have very high concentration of Ni (5 % to 9 %). According to EU Directive 76/769 EES (January 2000), the concentration of nickel in jewellery cannot exceed the maximum of 0.05 %. This EU Directive is a prerequisite for the prevention of allergic reactions caused by nickel. Nano-foil, with properly selected solder or braze components (without Ni), placed between metal parts could prevent allergic reactions to nickel and could enable a high quality of metal-metal joints.

6 CONCLUSIONS

Attempts to investigate the phenomena occurring on liquid metal/ceramics interfaces during metal ceramic joining in dental practice and jewellery manufacturing are still in their early stages. In this paper we carefully explain only the basic concepts and approaches necessary to treat wetting with diffusion phenomena accompanied by chemical reactions. The attention is confined to the typical examples taken from the actual practice and literature.

Nowadays, in dentistry, attention is increasingly focusing on the extensive range of alternative materials. These new materials include titanium and cobalt/nickel base alloys and all ceramic crowns. The latter have excellent aesthetic properties, but do not have the long-term clinical approval that gold has. For example, zirconia has only passed clinical tests during the last 8 years. In addition, the CAD/CAM techniques associated with the use of these materials are, in many cases, prohibitively expensive. Moreover, the problems of poor aesthetics often associated with porcelain-fused-to-metal techniques might be addressed through the use of extremely high gold content alloys, which have recently been patented. It is considered that, as CAD/CAM technology progresses, special high gold alloys should be developed which are well suited to milling and grinding operations and sufficiently high strength for long span bridges and small cross sections. Besides long term clinical approval and longevity, the most important advantages of gold alloys are easy workability, biocompatibility, aesthetics and maximum range of indications.

ACKNOWLEDGEMENT

This paper is part of Eureka project E!4213 NANO-FOIL. The authors gratefully acknowledge the Ministry of Higher Education, Science and Technology of the Republic of Slovenia and the Ministry of Science and Technological Development of the Republic of Serbia.

7 REFERENCES

[1] Z. Samardžija, R. B. Marinenko, S. Bernik, M. Kosec, M. Čeh, Mater. Technol., 37 (**2003**), 1–2

[2] T. Kopar, V. Ducman, Mater. Technol., 37 (**2003**), 1–2

[3] S. Bernik, M. Podlogar, N. Daneu, A. Rečnik, Mater. Technol., 42 (**2008**), 2

[4] G. Elssner, G. Petzow, ISIJ Int., 30 (**1990**), 1011

[5] A. Meier, D.A. Javernick, G. R. Edvards, JOM, February (**1999**), 44

[6] O. Levenspiel, Chemical reaction engineering 1999, (John Wiley & Sons, Inc.)

[7] K. T. Raic, Unsteady or starting phenomena at liquid metal/ceramic interfaces, Advances in Science and Technology, 32 (**2003**), 725–733

[8] K. T. Raic, An estimate of Si3N4 diffusion into Cu based filler metal, Ceramics International, 26 (**2000**), 19

[9] M. Mihailovic, T. Volkov Husovic, K. T. Raic, Micro- and nano-scale wetting of reactive metal at metal-ceramic interface, Advances in Science and Technology, 45 (**2006**), 1526–1531

[10] E. Saiz, R. M. Cannon, A. P. Tomsia, Acta Mater., 47 (**1999**), 4209

[11] M. D. Baldwin, P. R. Chidambaram, G. R. Edwards, Metallurgical and Materials Transactions A, 25A (**1994**), 2497

[12] Y. Nakao, K. Nishimoto, K. Saida, ISIJ Int., 30 (**1990**), 1142

[13] A. B. D. Cassie, S. Baxter, Trans. Faraday Soc., 40 (**1944**), 546

[14] W. Mader, M. Ruhle, Acta Metall., 37 (**1989**), 953

[15] A. Meier, P. R. Chidambaram, G. R. Edwards, *J. Mat.Sci.*, 30 (**1995**), 3791–3798

[16] R. G. Craig, J. M. Powers, Restorative Dental Materials, 11th ed., Ed., Mosby, Inc., 2002

[17] Gross U, H. J. Schmitz, V. Strunz, Surface activities of bioactive glass, aluminium oxid and titanium in a living environment. Ann NY Acad Sci, 523 (**1988**) 211–26

[18] W. Q. Yan, T. Nakamura, M. Kobayashi, H. M. Kim, F. Miyaji, T. Kokubo, Bonding of chemical treated titanium implants to bone. J Biomed Mater Res., 37 (**1997**) 2, 267–75

[19] M. Weinlaender, Bone growth around dental implants. Dental Clin North Am 35 (**1991**), 3, 585–601

[20] Hench LL, Wilson J. Surface-active biomaterials. Science, 226 (4675) (**1984**), 630–6

[21] D. Stamenković et al. Stomatološki gradivni materijali, 2003, ZUNS, Beograd

[22] K. T. Raic et al., Nanofoils for Soldering and Brazing in Dental Joining Practice and Jewellery Manufacturing, 1st International Conference on Materials and Technology sponsored by FEMS and IUVSTA,13-15 October (**2008**), Portorož, Slovenia, published in Mater. Technol., 43 (**2009**)1, 3

UDK 669.14.018.8:620.193
Original scientific article/Izvirni znanstveni članek

ISSN 1580-2949
MTAEC9, 44(2)67(2010)

INFLUENCE OF MnS INCLUSIONS ON THE CORROSION OF AUSTENITIC STAINLESS STEELS

VPLIV VKLJUČKOV MnS NA KOROZIJSKO ODPORNOST AVSTENITNIH NERJAVNIH JEKEL

Črtomir Donik, Irena Paulin, Monika Jenko
Institute of Metals and Technology, Lepi pot 11, SI-1000 Ljubljana, Slovenia
crtomir.donik@imt.si

Prejem rokopisa – received: 2009-09-19; sprejem za objavo – accepted for publication: 2009-12-21

The influence of alloy sulfur on the crevice solution chemistry and the nature of the surface in the crevice during initiation were investigated. Two austenitic steels with different amounts of sulfur in the alloy, AISI 316L and SS 2343, were compared using electrochemical measurements with an additional standard test – ASTM G48. The electrochemical measurements, i.e., a potentiodynamic measurement, a linear polarization and a Tafel polarization, were performed in a typical corrosion solution of 3.5 % NaCl and 0.1 % NaCl. The results show the difference for the steels in a low concentration of Cl^- ions, while in the higher concentration of the Cl^- ions the steels act very similarly. The MnS inclusions were analyzed and characterized using high-resolution SEM with EDX elemental analyses. The SE images show large differences for these materials in terms of the amount of inclusions. From the EDX measurements it was confirmed that the inclusions consist of Mn and S, and very few other types of inclusions were found.

Keywords: corrosion, stainless steel, MnS inclusion, electrochemical corrosion tests, ASTM G48

Raziskovali smo vpliv vsebnosti žvepla na korozijske lastnosti dveh avstenitnih nerjavnih jekel. Z elektrokemijskimi meritvami in s standardnimi preizkusi jamičaste korozije ASTM G48 smo poskušali ugotoviti razlike med dvema preiskovanima materialoma. Preiskovali smo dve po sestavi podobni nerjavni jekli tipa AISI 316L in SS 2343 z različnima vsebnostma žvepla. Elektrokemijske meritve: potenciodinamske meritve, linearne polarizacije in Tafelove polarizacije, smo naredili v tipični raztopini za korozijske preizkuse 3,5 % in 0,1 % NaCl. Pri nizkih koncentracijah kloridnih ionov v raztopini lahko opazimo odmike med lastnostmi materialov, medtem ko prihaja pri visokih koncentracijah kloridnih ionov do tega, da imata materiala zelo podobne korozijske lastnosti. S pregledom pod vrstičnim elektronskim mikroskopom visoke ločljivosti z EDX analizatorjem smo določili obliko in vrsto vključkov ter njihovo sestavo. Pri SEM-posnetkih lahko opazimo razlike med materialoma po količini vključkov in potrdimo z EDX-analizo, da vključki vsebujejo elementa Mn in S ter da skoraj ni prisotnih drugih vključkov.

Ključne besede: korozija, nerjavna jekla, MnS-vključki, elektrokemijski korozijski preizkusi, ASTM G48

1 INTRODUCTION

The effect of sulfur on the corrosion behavior of austenitic stainless steel is manifested through the behavior of the sulfide inclusions due to the low solubility of sulfur in ferrous metals.[1–5] Sulfide inclusions have been recognized as preferential sites for localized corrosion for almost 100 years, for steels, and for almost 60 years for stainless steels.[1,6–13] The effect of an alloying element can be manifested through effects on the passive film, the local solution chemistry, or the interfacial electrochemical kinetics.[10,14–23] The effects of alloyed sulfur on the localized corrosion in steels have been ascribed by various workers to each of these mechanisms. In our stainless steel, SS 2343, the sulfur is added to enhance lubrication through inclusions in the oil-free processes.[2,22–24]

Many theories have proposed that changes in the occluded chemistry are the key due to the effects of the dissolution products of the MnS inclusions.[2,23] Because most dissolved sulfur species have been observed to enhance metal dissolution, many sulfur species (i.e., sulfate, thiosulfate, elemental sulfur, and aqueous sulfide) have been predicted to result from MnS inclusion dissolution in the occluded region. Two categories of sulfur species may be considered, depending on the origin of the species: (a) sulfur species in the environment (H_2S, HS^-, S_2O_3, SO_2, HSO_4^-, SO_4^{2-}) and (b) sulfur in the material (sulfur in solid solution, sulfur segregated at the surface or in the grain boundaries, and sulfur in the sulfide inclusions).[4,25] In the case of the MnS sulfate inclusions, although their determination effect on the corrosion of steel and stainless steel has been extensively studied, the exact mechanism is not known. Sulfate (SO_4^{2-}) was predicted by Eklund to be the dominant dissolved sulfur species originating from sulfide inclusions via the electrochemical oxidation of the metal sulfide in the inclusions to sulfate, with the simultaneous formation of acid.[26]

The alteration of the chemistry of the stainless-steel surface in the vicinity of the sulfide inclusions, and the subsequent effects on the interfacial kinetics, has also been proposed as playing an important role in localized corrosion initiation. It was also observed that the corrosion initiated primarily at the inclusion edges, and concluded that the bare metal initially exposed upon inclusion dissolution became passivated and did not corrode until the precipitation of a $MnCl_2$ salt film (found using AES) occurred to restrict the mass transport. Smialowska[27] proposed that localized corrosion initiated by the formation of a thick salt layer at weak spots in the passive film (such as might be expected at inclusions), followed by hydrolysis of the salt leading to local acidification, inclusion dissolution and exposure of the bare, unprotected metal. Marcus et al.[27] proposed that regardless of its origin (i.e., from the alloy or from the solution), sulfur enhances metal dissolution via the formation of an adsorbed sulfur layer, which leads to weakening of the metal-metal bonds on the surface, thereby reducing the activation energy barrier for metal dissolution.

The important aspect of the corrosion is the formation of the passive film on the top of stainless steels. After the formation of this passive film on the bare metal surface, a slow dissolution of the metal cations continues, involving dissolution at the passive film surface and transport of the ions through the oxide. The question then arises as to where the bulk impurities (e.g., sulfur) go during the process. Above the critical concentration of sulfur at the interface (metal/oxide) the breakdown of the passive film was observed.[4]

There is much evidence for the damaging effect of the sulfur species over a wide range of corrosion-related service failures. The relation between the sulfur-induced corrosion mechanism presented in areas of practical importance can be rationalized on the basis of (a) the source of the sulfur, (b) the transport process to the metal surface, and (c) the condition of the reduction of the sulfur species into the harmful chemical state of sulfur.

Although it is clear that sulfide inclusions act as preferential sites for localized corrosion, the mechanism by which this occurs has remained unclear.

In the present work two stainless steels with different amounts of sulfur in the alloy were studied. The study was conducted using different electrochemical techniques: potentiodynamic measurements, linear polarization and Tafel polarization. MnS inclusions were investigated using SEM with EDX measurements.[28.29]

2 EXPERIMENTAL

Two types of stainless steel were investigated. Their compositions were confirmed using an Optical Emission Spectrometer (OES) as follows (weight percent): 17.0 % Cr, 10.0 % Ni, 1.5 % Mn, 0.40 % Si, 0.035 % P, 0.002 % S, 0.015 % C and the remainder Fe, denoted as AISI 316L; and 16.5 % Cr, 10.5 % Ni, 1.5 % Mn, 0.38 % Si, 0.041 % P, 0.025 % S, 0.020 % C and the remainder Fe, denoted as SS 2343.

The experiments for the electrochemical measurements were carried out in 3.5 % sodium chloride solution with and without 0.5-M Na_2S, and in 0.1 % sodium chloride solution. The standard test ASTM G48 was performed in a 6 % $FeCl_3$ solution at room temperature. All the chemicals were from Merck, Darmstadt, Germany.

The test specimens were cut into discs of 15 mm diameter. The specimens were abraded with SiC emery paper down to a 1000-grit prior to the electrochemical measurements. The specimens were then embedded in a Teflon PAR holder and employed as a working electrode. The reference electrode was a saturated calomel electrode (SCE, 0.242 V vs. SHE) and the counter electrode was a high-purity graphite rod.

Tafel polarization, potentiodynamic and linear polarization measurements were recorded using an EG&G PAR PC-controlled potentiostat/galvanostat Model 263 with SoftCorr computer programs. In the case of the potentiodynamic measurements and the linear polarization the specimens were immersed in the solution 1 h prior to the measurement in order to stabilize the surface at the open-circuit potential. Potentiodynamic curves were recorded starting at 250 mV more negative than the open-circuit potential. The potential was then increased, using a scan rate of 1 $mV\,s^{-1}$, until the transpassive region was reached. Linear polarization curves were recorded at ±10 mV around the open-circuit potential using a scan rate of 0.1 $mV\,s^{-1}$. The Tafel polarization curves were recorded at ±250 mV around the open-circuit potential using a scan rate of 0.5 $mV\ s^{-1}$. Some of the samples were passivated in 3M HNO_3 for 30 min to prevent localized corrosion on the boldly exposed surfaces.

The surface analytical experiments were performed using a high-resolution Scanning Electron Microscope JEOL JSM-6500F.

The standard test method ASTM G 48 for the pitting corrosion resistance of stainless steels and related alloys uses ferritic chloride solution. The method is used to compare the resistance of the stainless steels and related alloys in order to increase the resistance to pitting and crevice-corrosion initiation under the specific conditions. In our experiments *Method A* of standard ASTM G48 – ferric chloride pitting test was used: 6.0 % $FeCl_{3(aq)}$ with test specimens of 25 mm × 50 mm without sharp edges. All the specimens in the test had the same dimensions and were grinded with silicon grinding paper 600. The samples were weighed before and after exposure, and exposed to the solution for 72 h.

3 RESULTS AND DISCUSSION

3.1 Polarization measurements

In order to study the influence of the sulfur inclusions in stainless steels, different test solutions were used. The linear polarization curves were recorded for both materials on samples around the corrosion potential (**Figure 1**).

The calculations were performed from linear polarization measurements using the equation:

$$R_p = \beta_a \beta_c / (2.3\ I_{corr}\,(\beta_a + \beta_c)).$$

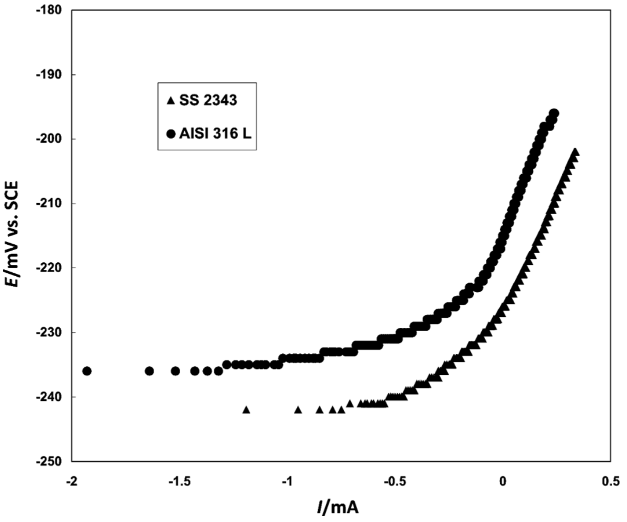

Figure 1: Linear polarization curves of the stainless steels AISI 316 L and SS 2343 in a 0.1 % NaCl solution

Slika 1: Graf linearne polarizacije nerjavnih jekel AISI 316 L in SS 2343 v 0,1 % raztopini NaCl

The polarization resistance, R_p, is evaluated from the linear polarization curves by applying a linear least-squares fit of the data around ±10 mV E_{corr}. The corrosion current, $I_{corr.}$, is calculated from R_p, the least-squares slope, and the Tafel constants, β_a and β_c, of 100 mV decade^{-1}. The value of $E(I = 0)$ is calculated from the least-squares intercept.

The corrosion rate was calculated by using the following conversion formula: $v_{corr.} = C(EW/d)(I_{corr.}/A)$, where EW is the equivalent weight of the sample in g, A is the sample area in cm^2, d is its density in g/mL, and C is a conversion constant that is dependent upon the units desired. The slopes of both materials were similar, so the corrosion rates of these materials did not differ significantly from each other. The corrosion potential for the stainless-steel AISI 316 L was –220 mV and for SS 2343 it was –230 mV.

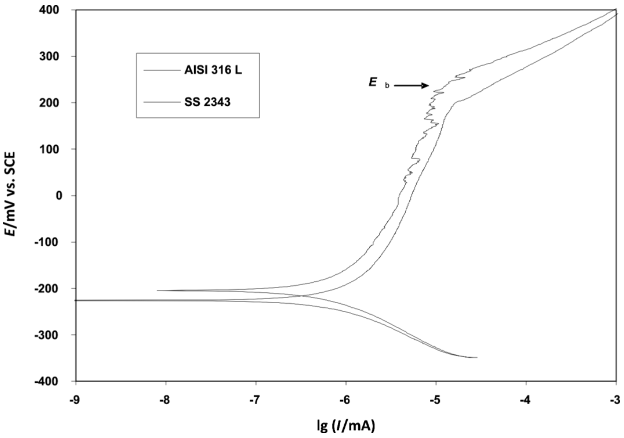

Figure 3: Potentiodynamic curves of the stainless steels AISI 316 L and SS 2343 in a 3.5 % NaCl solution

Slika 3: Potenciodinamski krivulji vzorcev nerjavnih jekel AISI 316 L in SS 2343 v 3,5-odstotni raztopini NaCl

The potentiodynamic curves were measured in two different solutions: 0.1% and 3.5 % NaCl, with and without the addition of $Na_2S \cdot 9H_2O$. **Figure 2** shows the potentiodynamic curves of the stainless steels AISI 316 L and SS 2343 in 0.1 % NaCl without any pre-passivation of the materials. After 1 h of stabilization at the open-circuit potential, the corrosion potentials (E_{corr}) for both materials were around –350 mV. Following the Tafel region both alloys exhibited passive behavior. The passive region is limited by the breakdown potential (E_b), which corresponds to the oxidation of water and the transpassive oxidation of the metal species. The breakdown potential for SS 2343 was approximately 380 mV and for AISI 316L it was 600 mV.

Figure 3 shows the potentiodynamic curves of the stainless steels AISI 316L and SS 2343 in 3.5 % NaCl. After 1 h of stabilization at the open circuit, the potential values of E_{corr} for both alloys were around –200 mV, although it was slightly higher for AISI 316L. The values of E_b are similar for both steels and are around 200 mV and 250 mV for SS 2343 and AISI 316L,

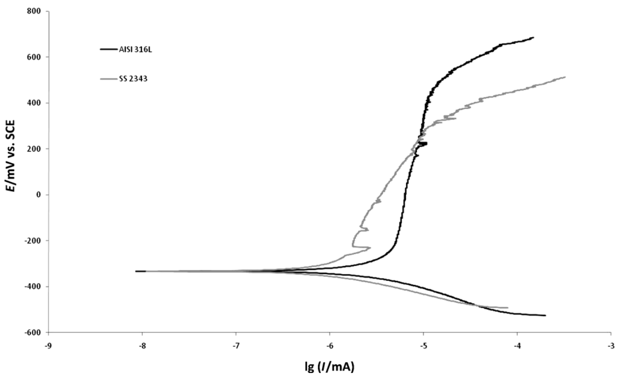

Figure 2: Potentiodynamic curves of the stainless steels AISI 316 L and SS 2343 passivated samples in a 0.1 % NaCl solution

Slika 2: Potenciodinamski krivulji pasiviranih vzorcev nerjavnih jekel AISI 316 L in SS 2343 v 0,1-odstotni raztopini NaCl

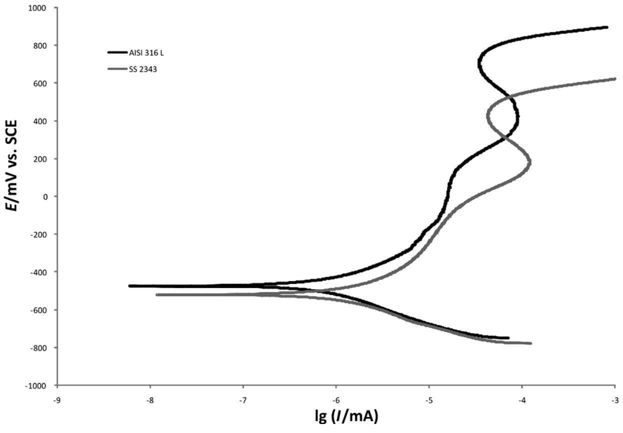

Figure 4: Potentiodynamic curves of the stainless steels AISI 316 L and SS 2343 in 0.1 % NaCl and 0.5-M Na_2S solution

Slika 4: Potenciodinamski krivulji nepasiviranih vzorcev nerjavnih jekel AISI 316 L in SS 2343 v 0,1-odstotni raztopini NaCl v 0,5 M Na_2S

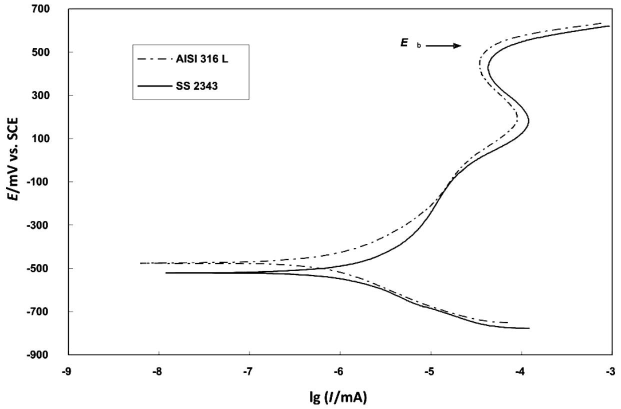

Figure 5: Potentiodynamic curves of the stainless steels AISI 316 L and SS 2343 in 3.5 % NaCl and 0.5-M Na_2S solution

Slika 5: Potenciodinamski krivulji nepasiviranih vzorcev nerjavnih jekel AISI 316 L in SS 2343 v 3,5-odstotni raztopini NaCl v 0,5 M Na_2S

respectively. The breakdown potentials for these alloys are relatively low due to a narrowing of the passive region in the presence of a high concentration of the Cl^- ions. As a result, the corrosion current values are relatively high, and therefore the corrosion rates are around mm per year (**Table 1**).

Table 1: Corrosion rates calculated from R_p for the stainless steels AISI 316 L and SS 2343 in (10^{-3} mm per year)

Tabela 1: Korozijske hitrosti, izračunane iz $R_{p,}$ za nerjavni jekli AISI 316 L in SS 2343 v (10^{-3} mm na leto)

Material	$v_{corr.}$ (10^{-3} mm/y)	
	NaCl	NaCl+Na_2S
AISI 316 L	140.6	46.75
SS 2343	158.9	53.93

The results mentioned above suggest that the distinction between the selected materials should be investigated in a low concentration of Cl^- ions. Therefore, the corrosive activator 0.5M Na_2S was added to the solution and the corrosion characteristics were measured. The pH of the test solution evidently increased; therefore, the corrosion potential was moved to more negative values to approximately –500 mV (**Figures 4 and 5**), whereas the corrosion current and the corrosion rate do not increase significantly (Table 1). In the presence of S^{2-} ions both steels exhibited better corrosion characteristics. However, we have to take into account that the pH is evidently higher than in the case of the test solution without the addition of the sulfide and that at approximately pH 12 the stainless steels are in a highly passivated area. In the 0.1 % solution of NaCl, both steels differed significantly, the passive region was evidently wider for the AISI 316 L compared to the SS 2343 (**Figure 2**). With the addition of 0.5-M Na_2S the values of E_{corr} were shifted from approximately –350 mV to –500 mV and –550 mV for the AISI 316L and SS 2343, respectively (**Figure 4**). The extension of the passive region increased with the addition of the sulfide. The E_b values were shifted to 450 mV and 750 mV for the AISI 316L and SS 2343, respectively (**Figure 4**).

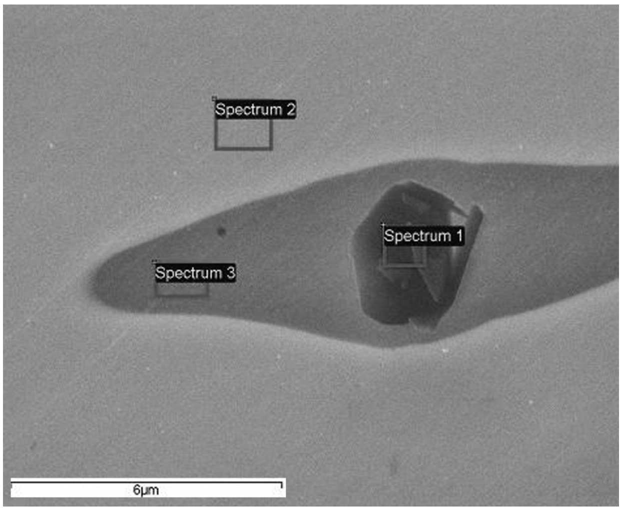

Figure 6: SE image of an inclusion in the sample SS 2343 with the areas of the EDX measurements

Slika 6: SE-posnetek površine vzorca s področij EDX-analize

3.2 Scanning Electron Microscopy

Figure 6 shows a SE image of an inclusion on the surface of the SS 2343; the EDX analysis was also performed on the marked areas. The results are shown in **Table 2**. The EDX measurements inside the inclusion showed the increased amount of Mn and S, with an atomic ratio 1 : 1, which indicates the presence of MnS in the inclusion (Spectrum 1 and 3). Spectrum 2 was performed on the bulk material and its composition confirmed the chemical composition of the standard composition of this type of stainless steel.

3.3 Standard corrosion test

Standard corrosion test for the pitting corrosion resistance of stainless steels and related alloys in the ferritic chloride solution, ASTM G 48, was performed for both alloys. The results are shown in **Table 3**, where the weight loss is shown in absolute mass and also in

Table 2: EDX measurements of the inclusion in SS 2343 in weight percent

Tabela 2: EDX-meritve vključka na površini jekla SS 2343 v masnih deležih (%)

	C	O	Mg	Al	S	Ti	Cr	Mn	Fe	Ni
Spectrum 1		27.31	1.08	24.34	14.40	0.82	4.66	21.59	3.82	1.98
Spectrum 2	2.25	0.67					16.67	1.77	64.37	10.82
Spectrum 3					29.60		5.68	50.09	4.15	1.30

mass percentage. The results show a slight difference in the weight loss, which could be the result of an increased amount of sulfur manganese inclusions. This small increase in the weight loss for the sample with the higher amount of sulfur inclusions is in the range of the measurement uncertainty and it could also be correlated to either a lower corrosion characteristic of the metal or a difference in the preparation of the samples.

Table 3: Results for ASTM G 48 test
Tabela 3: Rezultati preizkusa ASTM G 48

	m_1/g	m_2/g	Δm/g	Δm/%
AISI 316 L	3.0098	2.9195	0.0903	3.0
SS 2343	3.1527	2.9959	0.1568	4.9

4 CONCLUSION

The materials AISI 316 L and SS 2343 are chemically almost identical; the only difference is in the amount of sulfur, which is up to 10 times higher in the SS 2343. The results from the electrochemical measurements show a slight difference in the corrosion characteristics in favor of the AISI 316 L. However, the distinction between the selected materials is possible only in the solution containing low $Cl^–$ concentrations. In contrast, in the presence of high $Cl^–$ concentrations, the test solution is so aggressive that the difference in the chemical composition of both materials is diminished. The Na_2S addition in the corrosion solutions increased the pH to around pH 12, and therefore pushed the stainless steel into the passive region so the $S^{2–}$ ions did not play an important role in the differentiation of these to stainless steels. The difference between both materials is expressed by a standard corrosion test, ASTM G 48, where the AISI 316L showed a slightly better corrosion characteristic than the SS 2343 stainless steel.

5 REFERENCES

[1] Brossia, C. S.; Kelly, R. G., Occluded solution chemistry control and the role of alloy sulfur on the initiation of crevice corrosion in type 304ss. Corrosion Science 40 (**1998**) 11, 1851–1871

[2] Krawiec, H.; Vignal, V.; Heintz, O.; Oltra, R.; Chauveau, E., Dissolution of chromium-enriched inclusions and pitting corrosion of resulfurized stainless steels. Metallurgical and Materials Transactions a-Physical Metallurgy and Materials Science 37A (**2006**) 5, 1541–1549

[3] Krawiec, H.; Vignal, V.; Heintz, O.; Oltra, R., Influence of the dissolution of MnS inclusions under free corrosion and potentiostatic conditions on the composition of passive films and the electrochemical behaviour of stainless steels. Electrochimica Acta 51 (**2006**) 16, 3235–3243

[4] Sulfur-Assisted Corrosion Mechanisms and the Role of Alloyed Elements. In Corrosion Mechanisms in Theory and Practice, Marcus, P., Ed. CRC Press: 2002

[5] Schmuki, P.; Hildebrand, H.; Friedrich, A.; Virtanen, S., The composition of the boundary region of MnS inclusions in stainless steel and its relevance in triggering pitting corrosion. Corrosion Science 47 (**2005**) 5, 1239–1250

[6] Brossia, C. S.; Kelly, R. G., Influence of alloy sulfur content and bulk electrolyte composition on crevice corrosion initiation of austenitic stainless steel. Corrosion 54 (**1998**) 2, 145–154

[7] Donik, C.; Kocijan, A.; Mandrino, D.; Paulin, I.; Jenko, M.; Pihlar, B., Initial oxidation of duplex stainless steel. Applied Surface Science 255 (**2009**) 15, 7056–7061

[8] Kocijan, A.; Milosev, I.; Pihlar, B., The influence of complexing agent and proteins on the corrosion of stainless steels and their metal components. Journal of Materials Science-Materials in Medicine 14 (**2003**) 1, 69–77

[9] Kocijan, A.; Milosev, I.; Merl, D. K.; Pihlar, B., Electrochemical study of Co-based alloys in simulated physiological solution. Journal of Applied Electrochemistry 34 (**2004**) 5, 517–524

[10] Kocijan, A.; Donik, C.; Jenko, M., Electrochemical and XPS studies of the passive film formed on stainless steels in borate buffer and chloride solutions. Corrosion Science 49 (**2007**) 5, 2083–2098

[11] Jenko, M.; Mandrino, D., Application of surface analytical technique HRAES to metallurgy. Strojarstvo 41 (**1999**) 3–4, 107–110

[12] Mandrino, D.; Vrbanic, D.; Jenko, M.; Mihailovic, D.; Pejovnik, S., AES and XPS investigations of molybdenum-sulfur-iodine-based nanowire-type material. Surface and Interface Analysis 40 (**2008**) 9, 1289–1293

[13] Donik, C.; Kocijan, A.; Paulin, I.; Jenko, M., Oxidation of duplex stainless steel at moderately elevated temperature. Materiali in tehnologije / Materials and technology 2009, In Press, Corrected Proof

[14] Abreu, C. M.; Cristóbal, M. J.; Losada, R.; Nóvoa, X. R.; Pena, G.; Pérez, M. C., Comparative study of passive films of different stainless steels developed on alkaline medium. Electrochimica Acta 49 (**2004**) 17–18, 3049–3056

[15] Gojic, M.; Marijan, D.; Kosec, L., Electrochemical behavior of duplex stainless steel in borate buffer solution. Corrosion 56 (**2000**) 8, 839–848

[16] Kocijan, A.; Milosev, I.; Pihlar, B., Cobalt-based alloys for orthopaedic applications studied by electrochemical and XPS analysis. Journal of Materials Science-Materials in Medicine 15 (**2004**) 6, 643–650

[17] Kocijan, A.; Donik, C.; Jenko, M., The corrosion behaviour of duplex stainless steel in chloride solutions studied by XPS. Materiali in Tehnologije 43 (**2009**) 4, 195–199

[18] Kocijan, A.; Donik, C.; Jenko, M., The electrochemical study of duplex stainless steel in chloride solutions. Materiali in Tehnologije 43 (**2009**) 1, 39–42

[19] Olefjord, I.; Clayton, C. R., Surface-composition of stainless-steel during active dissolution and passivation. Isij International 31 (**1991**) 2, 134–141

[20] Olsson, C. O. A.; Landolt, D., Passive films on stainless steels - chemistry, structure and growth. Electrochimica Acta 48 (**2003**) 9, 1093–1104

[21] Stypula, B.; Stoch, J., The characterization of passive films on chromium electrodes by XPS. Corrosion Science 36 (**1994**) 12, 2159–2167

[22] Bastos, I. N.; Tavares, S. S. M.; Dalard, F.; Nogueira, R. P., Effect of microstructure on corrosion behavior of superduplex stainless steel at critical environment conditions. Scripta Materialia 57 (**2007**) 10, 913–916

[23] Wranglen, G., Pitting and sulfide inclusions in steel. Corrosion Science 14 (**1974**) 5, 331–349

[24] Yin, Z. F.; Zhao, W. Z.; Tian, W.; Feng, Y. R.; Yin, C. X., Pitting behavior on super 13Cr stainless steel in 3.5% NaCl solution in the presence of acetic acid. Journal of Solid State Electrochemistry 13 (**2009**) 8, 1291–1296

[25] Marcus, P.; Talah, H., The sulfur-induced breakdown of the passive film and pitting studied on nickel and nickel-alloys. Corrosion Science 29 (**1989**) 4, 455–463

[26] Eklund, G. S., Initiation of pitting at sulfide inclusions in stainless-steel. Journal of the Electrochemical Society 121 (**1974**) 4, 467–473

[27] Lukac, C.; Lumsden, J. B.; Smialowska, S.; Staehle, R. W., Effects of temperature on kinetics of passive film growth on iron. Journal of the Electrochemical Society 122 (**1975**) 12, 1571–1579

[28] Mandrino, D.; Godec, M.; Torkar, M.; Jenko, M., Study of oxide protective layers on stainless steel by AES, EDS and XPS. Surface and Interface Analysis 40 (**2008**) 3–4, 285–289

[29] Paulin, I.; Donik, C.; Jenko, M., Mechanisms of HF bonding in dry scrubber in aluminium electrolysis. Materiali in Tehnologije 43 (**2009**) 4, 189–193

[30] International, A., ASTM G48-03(2009) Standard Test Methods for Pitting and Crevice Corrosion Resistance of Stainless Steels and Related Alloys by Use of Ferric Chloride Solution.

UDK 543.428.3:620.1/.2
Original scientific article/Izvirni znanstveni članek

ISSN 1580-2949
MTAEC9, 44(2)73(2010)

AES AND XPS CHARACTERIZATION OF TITANIUM HYDRIDE POWDER

PREISKAVE PRAŠKA TITANOVEGA HIDRIDA S SPEKTROSKOPIJO AUGERJEVIH ELEKTRONOV IN RENTGENSKO FOTOELEKTRONSKO SPEKTROSKOPIJO

Irena Paulin, Djordje Mandrino, Črtomir Donik, Monika Jenko
Institute of Metals and Technology, Lepi pot 11, 1000 Ljubljana, Slovenia
irena.paulin@imt.si

Prejem rokopisa – received: 2009-12-01; sprejem za objavo – accepted for publication: 2009-12-24

Titanium hydride powder, manufactured by ball milling titanium in a hydrogen atmosphere down to micron-sized particles, was analyzed by X-ray Photoelectron Spectroscopy (XPS). A strong titanium oxide signal was also measured, which decreased somewhat after intense sputtering of the sample, but was impossible to get rid of completely. This was probably due to the high surface/volume ratio of each TiH_x particle, which contributes to a substantial titanium oxide/TiH_x ratio, and due to the surface morphology of the powder sample, which leaves a considerable part of the oxide layer shaded during the sputtering. Auger Electron Spectroscopy (AES) was then employed and some characteristic differences in the shape of the Ti LMM spectra between the TiH_x and Ti were observed; however, they can be ascribed to the TiH_x only after a comparison with the same types of spectra measured on titanium oxide. An additional XPS measurement was performed with TiH_x powder and powdered Ti. The peaks were fitted with Ti oxide and metallic Ti components and the shifts of the metallic component between the Ti and TiH_x (a shift of 0.4 eV was expected) were checked for.

Keywords: titanium hydride, ball milling, AES, XPS

Prašek titanovega hidrida, sintetiziran z mletjem titana v krogličnem mlinčku v vodikovi atmosferi do mikrometrske velikosti delcev, smo analizirali z rentgensko fotoelektronsko spektroskopijo (XPS). Pri tem smo izmerili močan signal titanovega oksida, ki je sicer upadel po intenzivnem ionskem jedkanju površine vzorca, ni pa izginil. Verjeten razlog je visoko razmerje površina/volumen posameznih delcev TiH_x, ki prispeva k znatnemu razmerju titanov oksid/TiH_x, kakor tudi morfologija površine praškastega vzorca, zaradi katere je del oksida zasenčen med ionskim jedkanjem. S spektroskopijo Augerjevih elektronov (AES) smo opazili nekatere karakteristične razlike v obliki Ti LMM-spektrov med TiH_x in Ti, vendar jih je bilo mogoče pripisati TiH_x šele po primerjavi z enakim tipom spektrov, izmerjenih pri titanovem oksidu. Nadaljnjo meritev XPS smo opravili pri prašku TiH_x in prašku Ti. Določili smo oksidne in kovinske komponente vrhov in preverjali premike kovinskih komponent pri TiH_x glede na Ti (premik naj bi bil 0,4 eV).

Ključne besede: titanov hidrid, kroglični mlinček, AES, XPS

1 INTRODUCTION

Titanium hydride can be used as a catalyst in the reversible dehydrogenation of other hydrides and carbon nanotubes.[1,2,3] It is also used as a catalyst in the preparation of titanium compounds,[1,4,5] as a source of pure hydrogen,[1] in the manufacturing of ceramic and glass seals from a mixture of active metal titanium or titanium hydride in powder form [1,6] and titanium coatings.[1] It is also well known as a blowing agent in the production of aluminum foams and some other foam-like structures produced by powder metallurgy.[7,8] For these purposes extensive studies of titanium hydride as well as of dehydrogenation and their effect on the formation of alloy foams have been performed.[9,10] In this study an attempt was made to apply surface-analysis techniques (AES and XPS) to titanium hydride powder, manufactured by ball milling titanium in a hydrogen atmosphere, that is used for the commercial production of aluminum foam. It was shown previously that the characteristic signatures from ultra-high-vacuum (UHV) deposited thin-film titanium hydride can be obtained using these techniques.[11,12] In our case the titanium hydride was in the shape of micron-sized powder particles. Therefore, in the XPS a strong titanium oxide signal was also measured, which decreased somewhat after the intense sputtering of the sample, but was impossible to remove completely due to the high surface/volume ratio of each TiH_x particle, which contributes to the substantial titanium oxide/TiH_x ratio, and due to the surface morphology of the powder sample, which leaves a considerable part of the oxide layer shaded during the sputtering. This oxide component also influences the shape of the Ti LMM peaks. Thus, while relying on the same type of titanium hydride, the characteristic features in AES and XPS spectra, as observed by Lisowski et al.,[11] had to be resolved from rather complex data (due to the complexity of the system in this study compared to the system as described by Lisowski et al. [11]).

2 EXPERIMENTAL

Titanium hydride powder, milled titanium, polished titanium plate and titanium oxide powder samples were fixed onto sample holders for the SEM/AES/XPS investigations by means of UHV-compatible double-sided sticky tape. Th esputter cleaning of the samples was performed under UHV conditions inside the main vacuum chamber of the SEM/AES/XPS apparatus, where the samples were introduced via a fast-entry air-lock.

The SEM imaging as well as the AES and XPS depth profiling of the samples were performed using a VG-Scientific Microlab 310F SEM/AES/XPS. For all the XPS measurements, Mg K_{α} radiation at 1253.6 eV with an anode voltage × emission current = 12.5 kV × 16 mA = 200 W was used. For the XPS profiling measurements an Ar^{+} energy of 3 keV at 1 µA ion current over a 6 × 6 mm^2 area was used. Similar ion-beam parameters with a 4 × 4 mm^2 area were used for the AES profiling. A rough estimate for the sputtering rate during the XPS profiling parameters is of the order of 1 nm/min, and 2 nm/min for the AES.

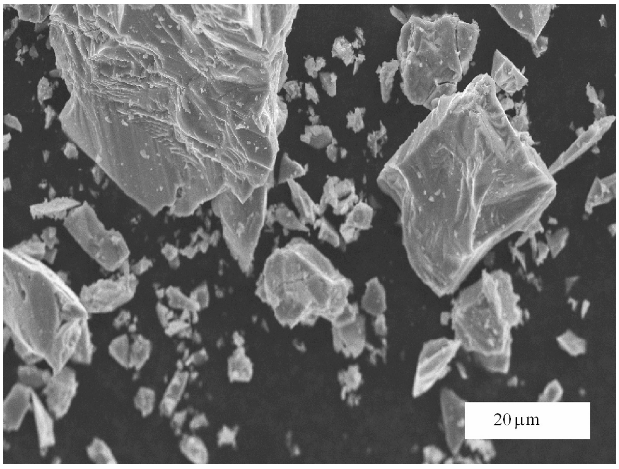

Figure 1: SEM image of the Ti hydride powder
Slika 1: SEM slika praška Ti hidrida

The AES and XPS spectra were acquired using the Avantage 3.41v data-acquisition & data-processing software supplied by the SEM/AES/XPS equipment manufacturer. Casa XPS software [13] was also used for detailed data processing.

3 RESULTS AND DISCUSSION

A SEM image of the particles of as-received Ti hydride powder manufactured by the ball milling of titanium in a hydrogen atmosphere is shown in **Figure 1**. It can be seen that powder grains are of irregular shape, ranging over more than two orders of magnitude in size: from below 0.5 µm to well over 50 µm.

In **Figure 2,** high-resolution XPS spectra of the Ti 2p from pure Ti (**Figure 2a, line 1**) and Ti hydride (**Figure 2a, line2**), as measured by Lisowski et al. [11] on UHV-deposited thin films, are shown. The Ti 2p of Ti hydride at 1200 s (top), 8400 s and 36000 s sputtering times are shown in **Figure 2b**. The Ti 2p of the milled Ti at 1200 s (top), 4800 s and 8400 s sputtering times are shown in **Figure 2c**. While in the spectra of Lisowski et al. [11] the metallic-type Ti seems to be predominant, with an approximately 0.4 eV shift towards higher binding energies for Ti $2p_{3/2}$, in the case of the Ti hydride, the spectra measured on the ball-milled Ti and the Ti hydride are much more complex. Ti 2p peaks obtained were fitted with the Ti $2p_{3/2}$ and Ti $2p_{1/2}$ components of metallic Ti, TiO_2 and TiO_x.[14,15] The metallic Ti $2p_{3/2}$ is the right-most component. The Ti hydride powder appears to be covered by a TiO_2 layer, which is partially removed or/and reduced only after prolonged sputtering (**Figure**

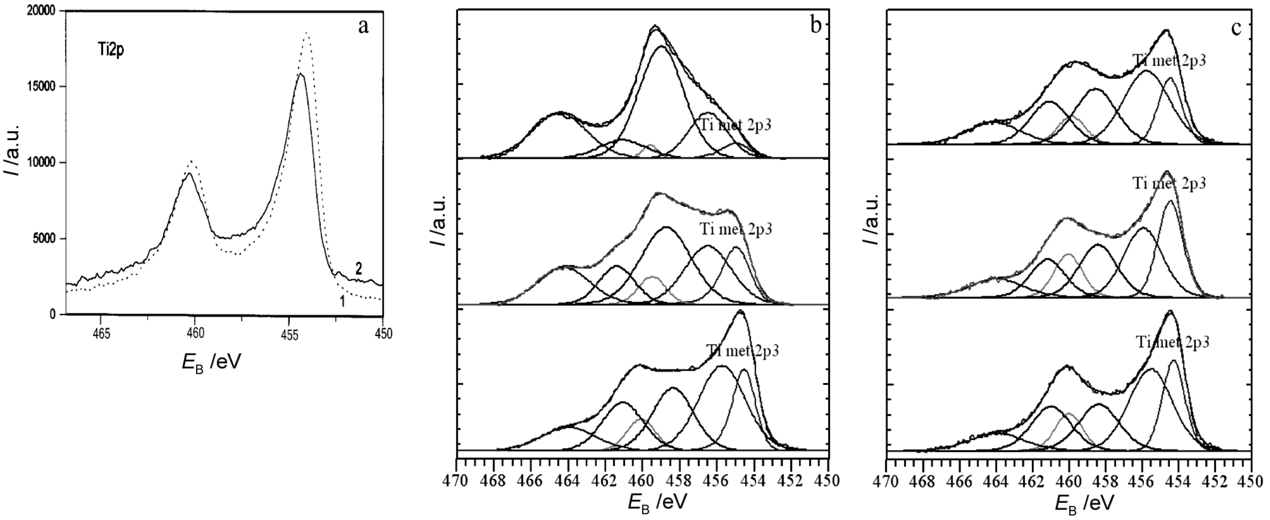

Figure 2: High-resolution XPS spectra of Ti 2p from pure Ti (dotted line 1) and Ti hydride (line 2) as measured by Lisowski et al. [11] on UHV-deposited thin films; Ti 2p of Ti hydride at 1200 s (top), 8400 s and 36000 s sputtering times (b); Ti 2p of milled Ti at 1200 s (top), 4800 s and 8400 s sputtering times (c).

Slika 2: Visokoločljivi spektri XPS-prehodov Ti 2p s čistega Ti (črtkana črta 1) in Ti- hidrida (črta 2), kot so jih izmerili Lisowski in sodelavci [11] na tankih plasteh, nanesenih v UHV; Ti 2p s Ti-hidrida po 1200 s (zgoraj), 8400 s in 36 000 s ionskega jedkanja (b); Ti 2p z mletega Ti po 1200 s (zgoraj), 4800 s in 8400 s ionskega jedkanja (c).

2b). The changes to the milled Ti with sputtering are much less pronounced, with TiO_x [16] and metallic Ti gaining slightly versus TiO_2 (**Figure 2c**). The average binding-energy value for the metallic Ti $2p_{3/2}$ component for the milled Ti can be determined from the XPS measurements after all sputtering cycles as (454.4 ± 0.1) eV.

In **Figure 3** the deviations, δE_B, of the metallic Ti $2p_{3/2}$ binding energy with sputtering time for Ti hydride from the average value of 454.4 eV determined for the milled Ti are shown. Also shown are the linear deviation trend and the average deviation, which is close to 0.4 eV. This can be interpreted as the Ti hydride characteristic shift in the metallic Ti $2p_{3/2}$ binding energy observed in Ti hydride thin films.[11] The highly scattered data are probably an artifact of the measurement as well as the fitting procedure. It is, nevertheless, possible to observe a declining deviation trend or even hypothesize about a possible switch from a high valued deviation (0.5–0.6 eV) to a low valued one (0.1–0.2 eV) in the 20 000–30 000 s sputtering time range. Whatever the precise form of this decline, it suggests that the Ti hydride powder

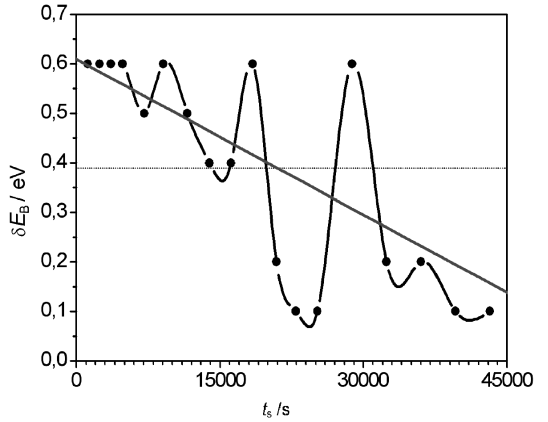

Figure 3: Deviation of the metallic Ti $2p_{3/2}$ binding energy with sputtering time for Ti hydride from the average value of 454.4 eV obtained for the milled Ti. The linear deviation trend (the thick solid line) and the average deviation (the thin horizontal line), which is close to 0.4 eV, are also shown.

Slika 3: Odvisnost razlike med vezavno energijo za kovinski Ti $2p_{3/2}$ Ti-hidrida in povprečno vrednostjo 454,4 eV, izmerjeno pri mletem Ti, od jedkalnega časa. Prikazana sta tudi linearen trend razlike (debela neprekinjena črta) in povprečna vrednost razlike (tanka vodoravna črta), ki je blizu 0,4 eV.

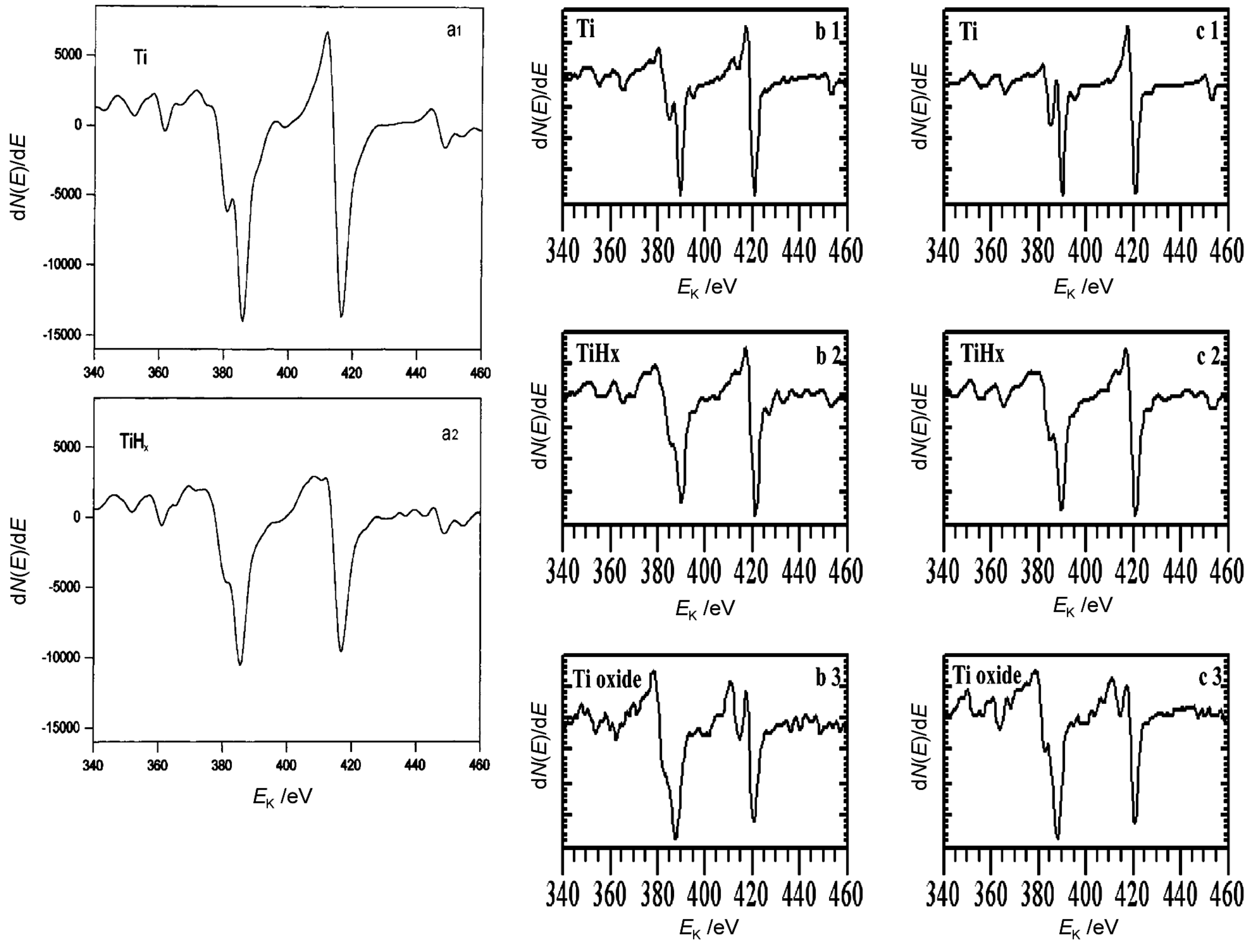

Fig 4: Ti LMM Auger transitions from pure Ti (a1) and Ti hydride (a2) as measured by Lisowski et al. [11] on UHV-deposited thin films; Ti LMM Auger transitions from pure Ti (b1, c1), Ti hydride (b2, c2) and Ti oxide (b3, c3) after 1200 s (b1, b2, b3) and 8400 s (c1, c2, c3) of sputtering.

Slika 4: Augerjevi prehodi Ti LMM s čistega Ti (a1) in Ti-hidrida (a2), kot so jih izmerili Lisowski in sodelavci[11] na tankih plasteh, nanesenih v UHV; Augerjevi prehodi Ti LMM s čistega Ti (b1, c1), Ti-hidrida (b2, c2) in Ti-oksida (b3, c3) po 1200 s (b1, b2, b3) in 8400 s (c1, c2, c3) ionskega jedkanja.

grains may not be of homogeneous consistency, with (more) hydrogen being closer to the grain surface.

In **Figure 4a** are the Ti LMM Auger transitions from pure Ti (**Figure 4a1**) and Ti hydride (**Figure 4a2**) as measured by Lisowski et al. [11] on UHV-deposited thin films. The Ti LMM Auger transitions from the polished Ti plate (**Figure 4b1**, **4c1**), the Ti hydride powder (**Figure 4b2**, **4c2**) and the TiO_2 powder (**Figure 4b3**, **4c3**) after 1200 s (**Figure 4b1**, **4b2**, **4b3**) and 8400 s (**Figure 4c1**, **Figure 4c2**, **Figure 4c3**) of sputtering are also shown. The differences in the peak shapes between all three samples can be observed and they become more pronounced with sputtering. The differences between the Ti hydride and the Ti do not completely agree with the differences found by Lisovski et al. [11]; however, it can be seen from **Figure 4** that they are not of the same nature as the differences between the Ti oxide and the Ti.

The most useful features are the less pointed shape of the maximum at approximately 375 eV [11], nearly dissappeared forking of TiH minimum between 385–390 eV and the small hydrogen-induced peak around 443 eV [11] in the spectra measured on the Ti hydride. Some other features also characteristic of Ti hydride may appear in these samples due to the Ti oxide.

4 CONCLUSIONS

XPS and AES characterizations of ball-milled Ti hydride powder were attempted using the same characteristic signatures in both methods as for Ti hydride thin films manufactured in UHV. Due to the manufacturing process the Ti hydride in this study was found to be covered with a layer of oxide that could not be completely removed, so the characteristic signal of Ti hydride could barely be extracted by peak fitting in the case of the XPS and had to be verified by comparison with metallic Ti and Ti oxide spectra in the case of AES. An additional benefit from the fitting of the Ti 2p is the suggestion that the titanium hydride grain may not have a homogeneous composition. To verify this, a cross-sectional AES study of individual grains by immersing titanium hydride powder in a low-melting-point alloy, and polishing the cross-section, a technique already used for study of soft-magnetic powders [17], is planned.

5 REFERENCES

[1] R. S. Venilla, A. Durygin, M. Merlini, Z. Wang, International Journal of Hydrogen Energy, 33 (**2008**), 6667–6671

[2] R. S Kumar, A. L. Cornelius, M. G. Pravica, M. F. Nicol, M. Y. Hu, P. C. Chow, Diam. & Relat. & Mater., 16 (**2007**), 1136–1139

[3] I. O. Bashkin, A. I. Koleshnikov, M. A. Adams, M. F. Nicol, M. Y. Hu, P.C. Chow, J. Phys. Condens. Matter., 12 (**2000**) 4757–4765

[4] M. N. Ozyagcilar, M.W. Davis; Catalysts for synthesis of ammonia, United States Patent 4623532, 1986

[5] V. E. Antonov, I. O. Bashkin, V. K. Fedotov, S. S. Khasanov, T. Hansen, A. S. Ivanov, Phys Rev B, 73 (**2006**)5, 054107–054112

[6] I. Paulin, C. Donik, M. Jenko, Mechanisms of HF Bonding in Dry Scrubber in Aluminium Electrolysis, Materiali in Tehnologije, 43 (**2009**) 4, 189

[7] PM Proa-Flores, RAL Drew, Advanced Engineering Materials, 10 (**2008**)9, 830–834

[8] A. Ibrahim, C. Koerner, R. F. Singer, Advanced Engineering Materials, 10 (**2008**), 845–848

[9] Y. W. Gu, M. S. Yong, B. Y. Tay, C. S. Lim, Materials Science & Engineering C, 29 (**2009**), 1515–1520

[10] M. Vijay, V. Selvarajan, K. P. Sreekumar, J. Yu, S. Liu, P.V. Ananthapadmanabhan, Solar Energy Materials & Solar Cells, 93 (**2009**), 1540–1549

[11] W. Lisowski, A. H. J. van den Berg, D. Leonard, H. J. Mathieu, Surface and Interface Analysis, 29 (**2000**), 292–297

[12] A. Kocijan, C. Donik, M. Jenko, The Corrosion Behaviour of duplex stainless steel in chloride solutions studied by XPS, Materiali in Tehnologije, 43 (**2009**) 4, 195

[13] Fairley N, CasaXPS VAMAS Processing Software. Available from World Wide Web: http://www.casaxps.com/

[14] Chastain J. (ed.), Handbook of X-ray Photoelectron Spectroscopy, Physical Electronics, Eden Prairie 1995

[15] C. D. Wagner, A.V. Naumkin, A. Kraut-Vass, J. W. Allison, C. J. Powell, J. R. Rumble (eds.), NIST X-ray Photoelectron Spectroscopy Database. Available from World Wide Web: http://srdata.nist.gov/xps

[16] C. Donik, A. Kocijan, I. Paulin, M. Jenko, The Oxidation of Duplex Stainless Steel at Moderately Elevated Temperatures, Materiali in Tehnologije, 43 (**2009**) 3, 137

[17] M. Godec, Dj. Mandrino, B. Šuštaršič, M. Jenko, Surface and Interface Analysis, 34 (**2002**), 346–351

UDK 669.14.018.252:539.42
Original scientific article/Izvirni znanstveni članek

ISSN 1580-2949
MTAEC9, 44(2)77(2010)

FRACTURE CHARACTERISTICS OF THE Cr-V LEDEBURITIC STEEL VANADIS 6

PRELOMNE ZNAČILNOSTI LEDEBURITNEGA Cr-V-JEKLA VANADIS 6

Peter Jurči[1], Borivoj Šuštaršič[2], Vojteh Leskovšek[2]

[1] Czech Technical University in Prague, Faculty of Mechanical Engineering, Karlovo nám. 13, 121 35 Prague 2, Czech Republic
[2]Institute of Metals and Technology, Lepi pot 11, 1000 Ljubljana, Slovenia
p.jurci@seznam.cz

Prejem rokopisa – received: 2009-11-16; sprejem za objavo – accepted for publication: 2009-12-08

The P/M Vanadis 6 is a very popular tool steel used for different cold work applications. The specimens for the three point bending tests and fracture toughness test were austenitized at two different temperatures, quenched with or without the sub-zero treatment and then double tempered. The bending strength was lower by higher austenitizing temperature and also with the use of sub-zero treatment. The average fracture toughness was lower by higher austenitizing temperature also and increased slightly with the sub-zero treatment. The lowering of bending strength can be considered as logical result because of the austenitic grain growth, as well as increased internal stresses in the case of sub-zero processed samples. For fracture toughness, the situation seems to be more complex. On one side, the effect of austenitizing temperature on fracture toughness is similar as for bending strength, on the other side, the sub-zero treatment induces a rather slight increase of fracture toughness. The paper presents some details on the experiments performed including possible explanation of the material's behaviour considering microstructure investigations.

Key words: ledeburitic Cr-V PM steel, heat treatment, sub-zeto treatment, bending strength, fracture toughness, fracture surface

PM-jeklo Vanadis 6 je zelo popularno orodno jeklo za različno uporabo v hladnem. Preizkušance za tri točkovni upogib in žilavost loma smo avstenitizirali pri dveh različnih temperaturah, kalili z obdelavo in brez nje pod temperaturno ničlo in dvakrat popustili. Ugotovili smo, da je upogibna trdnost nižja po kaljenju z višje temperature in po obdelavi pod ničlo. Žilavost loma je bila nižja po kaljenju z višje temperature in je bila nekoliko večja po obdelavi pod ničlo. Zmanjšana upogibna trdnost je logičen rezultat povečanja velikosti avstenitnih zrn in povečanja notranjih napetosti po obdelavi pod ničlo. Primer žilavosti loma je bolj kompleksen, kajti na eni strani temperatura avstenitizacije vpliva podobno na upogibno trdnost in žilavost loma, po drugi pa obdelava pod ničlo poveča žilavost loma.V članku so predstavljeni detajli o opravljenih preizkusih in predstavljena je razlaga vedenja materiala z upoštevanjem mikrostrukture.

Ključne besede: ledeburitno PM CrV-jeklo, toplotna obdelava, obdelava pod ničlo, upogibna trdnost, žilavost loma, površina preloma

1 GENERAL REMARKS

Ledeburitic steels have a high wear resistance and hardness and are used in many industrial operations like: metal cutting, wood cutting, fine blanking, bending etc. In these operations, the material must meet various requirements. It has to withstand compressive stresses, abrasive and/or adhesive wear, but also chipping and total tool collapse.

To meet these demands, the ledeburitic steels must have an optimal chemistry, as well as phase constitution. Moreover, a proper heat treatment must be performed before the use. The ledeburitic steels contain a high content of carbon and alloying elements that form carbides responsible not only for high hardness and wear resistance but also for the capability of the material to achieve a high strength and acceptable fracture toughness after heat treatment. For the resistance to chipping and total collapse, two basic characteristics are important: three-point bending strength as a measure for the resistance against the crack initiation and the fracture toughness that characterises the resistance of the material against crack propagation.

The three-point bending strength is sensitive to various factors. First of all it is important how the material was made. It is known that the large carbide networks, clusters or bands are responsible for a significant lowering of three-point bending strength and its anisotropy [1,2]. This is also the main reason why the steels made via the powder metallurgy (P/M) of rapidly solidified particles have higher bending strength than the materials of the same chemistry made by conventional metallurgy. The three-point bending strength is also influenced by the material cleanless. It was reported that oxides, sulphides and other impurities can decrease the three-point bending strength significantly even at relatively low quantity [3]. The quality of the surface should also not be neglected. Some investigations have confirmed that the three-point bending strength decreases as the surface roughness increases [4]. The three point-bending strength decreases with the increase of the austenitizing temperature because of the coarsening of the austenitic grains during austenitization [5].

On the other hand, the fracture toughness depends mainly on the matrix hardness and its ductility. Generally, it also depends to its relation to the carbide network (cohesive strength at carbide-matrix boundary i.e. shape, size and size distribution of carbide particles, carbide clusters, distance among the particles etc). Ledeburitic steels have to be heat treated up to approximately *HRc* 60 (or more in some cases); and their fracture toughness is relatively low. For the conventionally manufactured chromium ledeburitic steels, as well as high speed steels, it decreases with the increasing austenitizing temperature and also with increasing tempering temperature, but only up to the maximum of secondary hardness [6]. The orientation of carbides and/or the state of the carbides (networks or bands) play only minor role [4,7,8]. On the other hand, the role of carbide distribution is highlighted in the soft state of the steels [7,8] the microstructure with carbide network had the lower fracture toughness, although the wrought material had better values. No data, except the early work of Olsson and Fischmeister [9], are known on the assessment of fracture toughness of P/M made ledeburitic steels. However, results published in the mentioned paper are negatively influenced by the state of manufacturing technique, porosity of the consolidated material, and therefore they did not have a sufficient value for today's manufactured and used materials.

The ideas about the sub-zero treatment on the mechanical properties of ledeburitic steels was developed over last few decades [10,11]. This technique has early gained scientific interest, but the attempts of its application did not produce doubtless results. Kulmburg et al. [11], for instance, reported for the M2-type steel a reduction of the amount of retained austenite after sub-zero treatment at –196 °C for 1 h and slight lowering of three point bending strength. Berns [10], on the other hand, reported a significant hardness increase for the sub-zero processed X290Cr12 ledeburitic steel. Last decade has brought new accurate investigations on the nature of possible improvement of material characteristics after the sub-zero processing. Stratton [12] pointed out, that especially for the D2 ledeburitic steel, the improvement of wear resistance due to the sub-zero processing could be increased to extremely high values. According to investigations of Collins and Meng [13–15], it is assumed that deep cooling leads to an arrangement of the structure responsible for the hindering of the dislocation movement. This induces a strengthening of the material. In addition, Meng assumed [14] that martensite originated at very low temperatures can differ from that transformed at higher temperatures in the lattice parameter. The martensitic transformation is probably superposed with the precipitation of nanosized carbides particles coherent with the matrix. However, up to now the principal explanation of the positive effect on essential properties (hardness, wear resistance) is not entirely clear. Moreover, also an optimal processing route of the cryogenic processing is not clearly determined and the opinions about it are different.

The main goal of our experimental effort was a reliable investigation on the influence of various factors (heat treatment, sub-zero treatment, tempering) on fracture toughness and three point bending strength of the PM ledeburitic steels. The Vanadis 6 P/M steel produced by Uddeholm was selected as example because of its relatively simple chemistry.

2 EXPERIMENTAL

The experimental material was the ledeburitic steel Vanadis 6 with nominally 2.1 % C, 1.0 % Si, 0.4 % Mn, 6.8 % Cr, 1.5% Mo, 5.4 % V and Fe as balance, manufactured with P/M (HIP of rapidly solidified particles) and soft annealed to the hardness of HV_{10} = 284.

Two types of specimens were prepared for the investigations. Samples for the three point bend testing (numbered 1 to 28) had a cross section of (10 × 10) mm and a length of 100 mm. They were ground to obtain a final surface roughness of 0.2–0.3 μm. The second type of specimens were the circumferentially notched and pre-cracked specimens (numbered 33 to 69) prepared according to the method described in [6,16] (see also **Figure 1**).

The specimens were then submitted to the heat treatment procedure that included vacuum austenitization up to temperature 1000 °C or 1050 °C, nitrogen gas quenching at 5 bar pressure and double tempering, each cycle at 550 °C for 1 h. In selected cases, the sub-zero treatment in liquid nitrogen was inserted between the quenching and tempering. The parameters of heat-treatment, the average K_{IC} and final hardness and are summarized in **Table 1**.

The fracture toughness was determinated according to the method published elsewhere [6,16]. At least eight samples were tested for a given parameter of the heat treatment. Three point bending tests have been carried out at following parameters: distance between supports of 88.9 mm, loading in the central region and loading rate of 5 mm/min up to fracture. The results of bend strength testing and hardness measurements are given in **Table 2**.

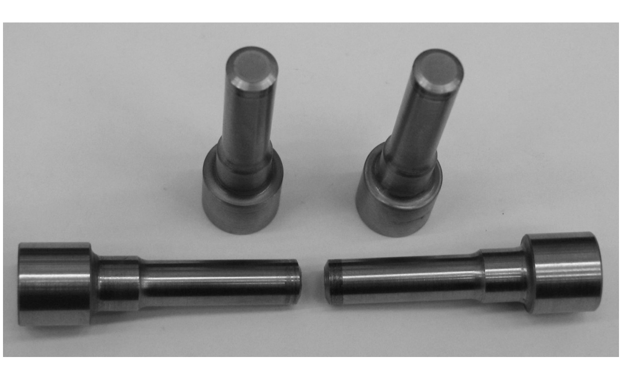

Figure 1: Precracked and fractured V notched cylindrical samples for K_{IC} determination

Slika 1: Prelomljeni valjasti preizkušanci z V zarezo za določitev K_{IC} z vnaprejšnjo razpoko

Table 1: K_{IC} for V notched cylindrical samples
Tabela 1: K_{IC} valjastih preizkušancev z V-zarezo

Specimens	Testing conditions			K_{IC}	Notch strength	Rockwell hardness
	Preheating and quenching	Subzero treatment in liqu. N_2	Tempering	Mpa √m	MPa	*HRc* *
33–40	650/850 °C → 1000 °C/30 → N_2 (5 bar)	–	2-times 550 °C/1 h	12.9 ± 0.9/1.3 (11.2 at $\boldsymbol{x}_0$)	283.3 ± 19.8/29.0	57.5 ± 0.3/0.7
41–50	650/850 °C → 1000 °C/30 → N_2 (5 bar)	−196 °C/24 h		13.2 ± 2.4/1.9 (9.5 at $\boldsymbol{x}_0$))	289.4 ± 51.6/42.0	56.4 ± 0.6/0.5
51–60	650/850 °C → 1050 °C/30 → N_2 (5 bar)	–		10.9 ± 1.5/1.2 (8.1 at $\boldsymbol{x}_0$))	238.0 ± 33.8/26.2	61.3 ± 0.4/0.8
61–69	650/850 °C → 1050 °C/30 → N_2 (5 bar)	−196 °C/24 h		12.5 ± 1.4/1.9 (9.1 at $\boldsymbol{x}_0$))	273.1 ± 31.2/40.9	58.8 ± 0.3/0.3

* One (1) Rockwell is added as a correction for rounded (cylindrical) samples

Table 2: Bend strength of samples with square section
Tabela 2: Upogibna trdnost preizkušancev s kvadratnim prerezom

Specimens	Testing conditions			Bend strength	Rockwell hardness
	Preheating and quenching	Subzero treatment in liqu. N_2	Tempering	MPa	*HRc*
1–7	650/850 °C → 1000 °C/30 → N_2 (5 bar)	–	2-times 550 °C/1 h	3626 ± 186/259	56.3 ± 0.7/1.2
8–14	650/850 °C → 1000 °C/30 → N_2 (5 bar)	−196 °C/24 h		3587 ± 143/169	55.3 ± 0.8/1.0
15–21	650/850 °C → 1050 °C/30 → N_2 5 bar	–		3474 ± 357/514	59.9 ± 0.8/1.1
22–28	650/850 °C → 1050 °C/30 → N_2 (5 bar)	−196 °C/24 h		3352 ± 385/307	58.1 ± 0.5/0.4

The microstructure of the material was investigated with light microscopy (LM) and scanning electron microscopy (SEM). The fractures surfaces were investigated with SEM. Hardness measurements were made using the Vickers method at a load of 98.1 N (HV_{10}) as well as using the Rockwell "C" method (*HRC*).

3 RESULTS AND DISCUSSION

The microstructure of the as-received material is shown in **Figure 2a** and **2b**. The LM micrograph (**Figure 2a**) gives us the overview. One can see that the material consists of the matrix and carbides particles that are very fine and uniformly distributed throughout the material. The SEM micrograph, (**Figure 2b**) shows that carbide particles of different size with the maximum size of particles is around 3 µm and the smallest have a size less than 0.5 µm.

The steel microstructure after heat processing is shown in **Figure 3a–d**. It consists of the martensitic matrix and of eutectic and part of secondary carbide particles. These particles are very fine and uniformly distributed in the matrix. The amount of carbides is slightly smaller for the specimens processed at higher austenitizing temperature. This is natural as higher temperature normally leads to the dissolution of large amount of secondary carbides.

Heat treatment leads to a substantial hardness increase. With increasing austenitizing temperature the hardness increases. It is natural because higher austenitizing temperature induces a better dissolution of secondary carbides and higher supersaturation level of martensite after the quenching. On the first sight, it is rather surprising that the sub-zero processing reduces the hardness only slightly. Several authors, for instance Berns [10], Kulmburg et al. [11], reported either slight or

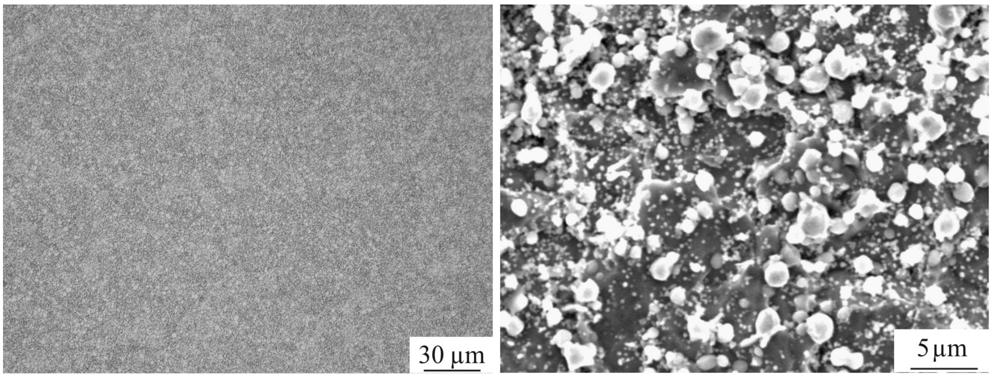

Figure 2: Microstructure of the investigated steel in as-received condition: a) LM micrograph and b) SEM micrograph
Slika 2: Mikrostruktura jekla v dobavljenem stanju; a) optični posnetek, b) SEM-posnetek

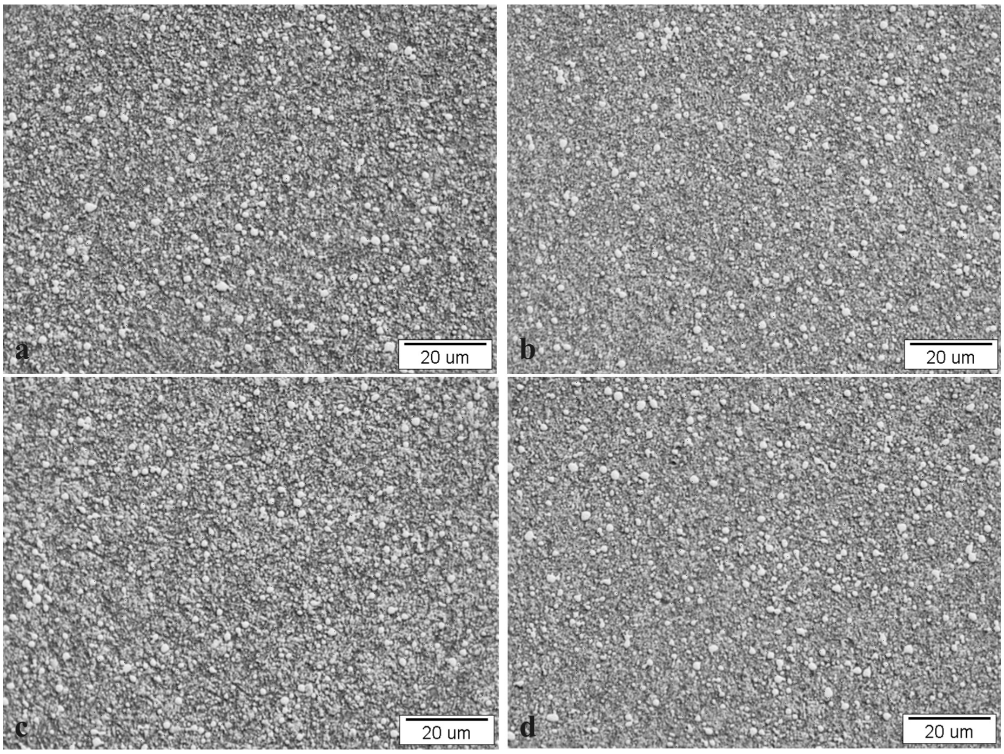

Figure 3: Microstructure of the Vanadis 6 steel after the heat treatment: a) austenitizing 1000 °C + quenching + 2x tempering, b) austenitizing 1000 °C + quenching + sub-zero + 2x tempering, c) austenitizing 1050 °C + quenching + 2x tempering, d) austenitizing 1050 °C + quenching + sub-zero + 2x tempering,
Slika 3: Mikrostruktura jekla po toplotni obdelavi: a) avstenitizacija pri 1000 °C + kaljenje + dvakratno popuščanje, b) avstenitizacija pri 1000 °C + kaljenje + obdelava pod ničlo + dvakratno popuščanje, c) avstenitizacija pri 1050 °C + kaljenje + dvakratno popuščanje, d) avstenitizacija pri 1050 °C + kaljenje + obdelava pod ničlo + dvakratno popuščanje.

more significant hardness increase of hardness after sub-zero treatment. However, in the mentioned papers, other ledeburitic steels were investigated, the sub-zero processing was carried out at different parameters and the tempering was shorter. It is assumed also, that two processes were happening during the deep freezing related to high stresses and strains; i.e. retained austenite to martensite transformation (hardness increase) and mechanical annealing (hardness decrease). Anyway, the reasons for the reduction in hardness requires more detailed TEM investigation.

The three point bending strength (**Table 2 and Figure 4a**), decreases with the increasing austenitizing temperature. This was expeced because at increased austenitizing temperature grains coarse structural constituents are changed and the bending strength is decreased. Also after the sub-zero processing, the three point bending strength is decreased. Similar results were published also by other authors [10,11,14] that did not suggest a reliable explanation. The bending strength is lower because of the increased internal stresses after quenching and deep freezing. These stresses are relieved by the

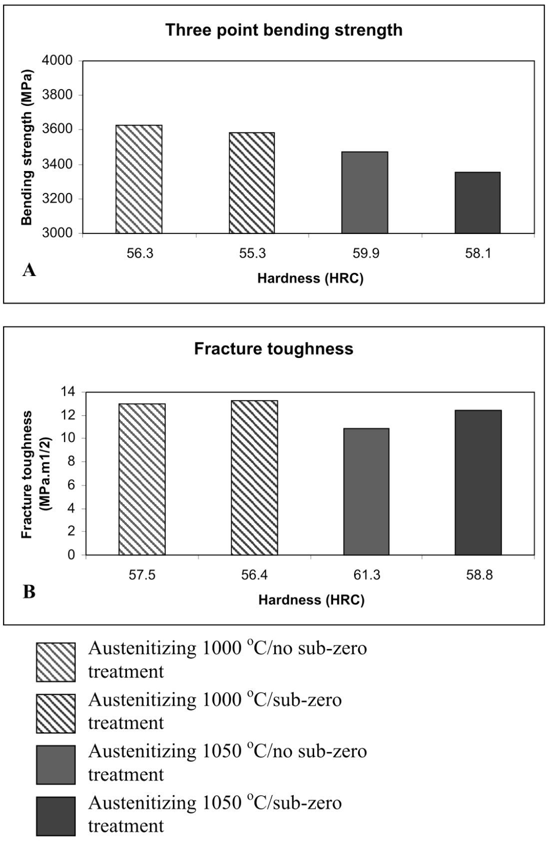

Figure 4: Graphical presentation of obtained experimental results for a) three-point bend strength and b) average fracture toughnes for different hardness
Slika 4: Eksperimentalni rezultati za a) tri točkovni preizkus upogibne trdnosti in b) žilavosti loma pri različni trdoti

tempering and this supports the conclusion that the sub-zero treatment decreases the material's resistivity to crack initiation. A possible explanations could be in the increased surface roughness because of martensite transformation (lattice reorientation and deformation) and mechanical annealing (dislocation glide and annihilation). Further investigations should prove this explanation.

On the other hand the results of fracture toughness (**Table 1** and **Figure 4b**) show slightly opposite tendency. Normally, it can be expected that higher austenitizing temperature would lead to a lower fracture toughness, since it is function of the matrix hardness. The principal explanation would the higher hardness of the matrix after higher austenitizing temperature. Nevertheless, the average fracture toughness after heat processing of Vanadis 6 steel was found to be slightly higher for sub-zero processed material. This is rather contradictory to the generally expected behaviour, as it is normally assumed that not only the resistance against initiation, but also the resistance against propagation of the crack should be lowered. However, it seems that the situation can be considered to be more complex, the more complete transformation of austenite into the martensite would be in favour of lower fracture toughness. On the other hand, the so-called effect of mechanical annealing (dislocation glide to the grain boundaries and a decrease of dislocation concentration inside the grains) can induce a resistance to the crack propagation resulting in the improvement of fracture toughness.

It is noticed that former investigations have shown a linear correlation between so called weak spot (x_0) and fracture toughness K_{IC}. In the case of tool and high speed steels this linear correlation shows a relatively large statistical reliability ($r^2 > 0.7$) and as the relevant material's K_{IC} value is used, the K_{IC} value at $x_0 = 0$ [18–20] are very conservative. In the case of materials with larger K_{IC} (for example hot work tool steels) this correlation is not so distinct and the mean value of all the determined K_{IC} values is usually used. In **Table 1** both approaches of K_{IC} results are given. For the $K_{IC} = f(x_0)$ approach a relatively good statistical reliability of results is obtained for three cases (r^2 = 0.7–0.9), except for the first set of experiments (specimens 33–40, **Table 1**). The obtained K_{IC} values at $x_0 = 0$ seems also to be relatively too conservative, therefore mean values (arithmetic average) of K_{IC} are used as relevant.

The fracture surface of not sub-zero processed sample after three point bending test is in **Figure 5a**. The fracture was initiated on the tensile strained side of the specimen (left margin of the micrograph) and propagated downwards the material. Some propagation lines are visible in the micrograph. In the direction from the tensile side to the core of the sample the fracture surface becomes a slightly more marked topography. As reported [5], such fracture surface (typical for hard steels) is known as low energetic ductile because some energy is also spent for the plastic deformation. However, the plastic energy is relatively low and corresponds to a relatively flat surface relief of the surface. More detailed micrograph, **Figure 5b**, shows that the fracture was propagated by two main mechanisms. The first is the cracking of coarser carbide particles (see **Figure 5c**) and the second is the de-cohesion at the carbide/matrix interfaces which can be attributed to different plasticity of these two microstructural constituents. In some places dimples are (tracks of extracted carbides) visible with in vicinity a plastically deformed matrix, **Figure 5d**.

The fracture surface of sub-zero processed material is shown in **Figure 6**. On the overview, **Figure 6a**, also propagation lines on the tensile strained side are visible. Detail micrograph, **Figure 6b**, confirms that the mechanism of fracture propagation is very similar to that of the sample processed without sub-zero period. Both, cracking of carbide particles and de-cohesion on the matrix/particle interfaces are clearly visible in the micrograph.

To explain the fracture propagation more precisely, the fracture surface of one specimen processed with a sub-zero period was examined to more in detail. **Figure 7a** shows a SEM micrograph at high magnification.

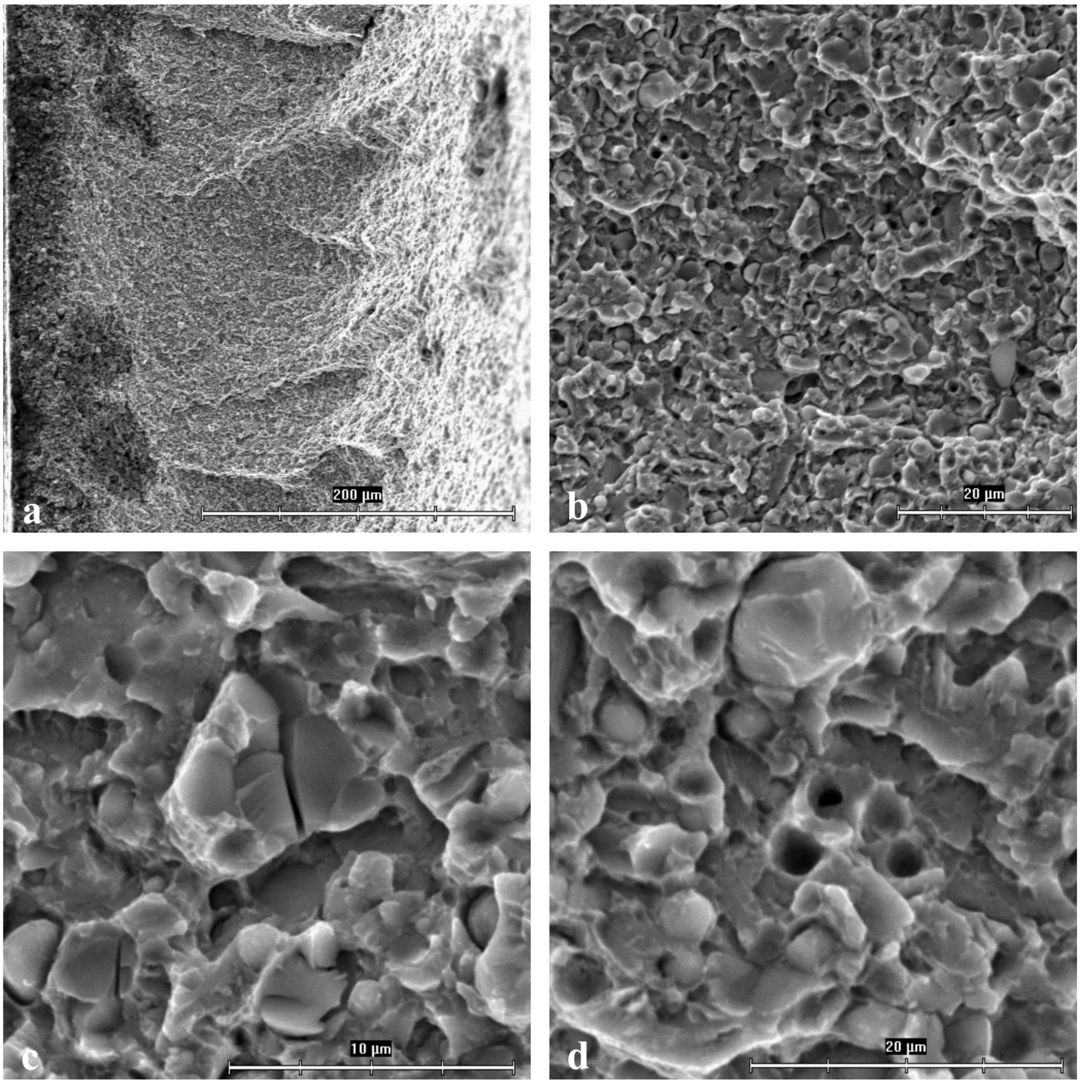

Figure 5: Fracture surface of the steel Vanadis 6 without a sub-zero treatment by different magnification
Slika 5: Površina preloma jekla brez obdelave pod ničlo; EM-posnetki pri različnih povečavah

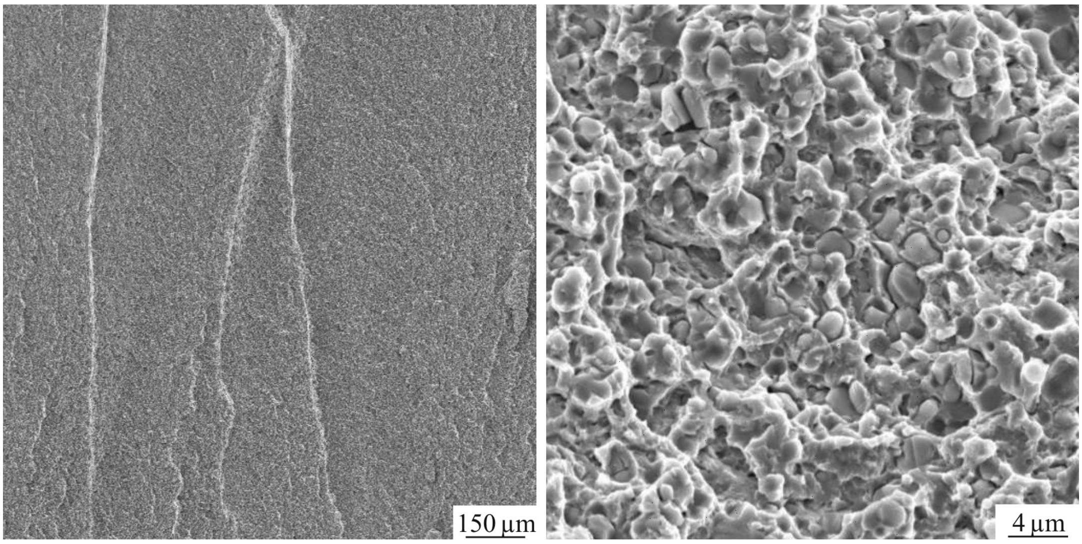

Figure 6: Fracture surface of the steel Vanadis 6 processed with a sub-zero period by different magnification
Slika 6: Površina preloma jekla po obdelavi pod ničlo; SEM-posnetka pri različni povečavi

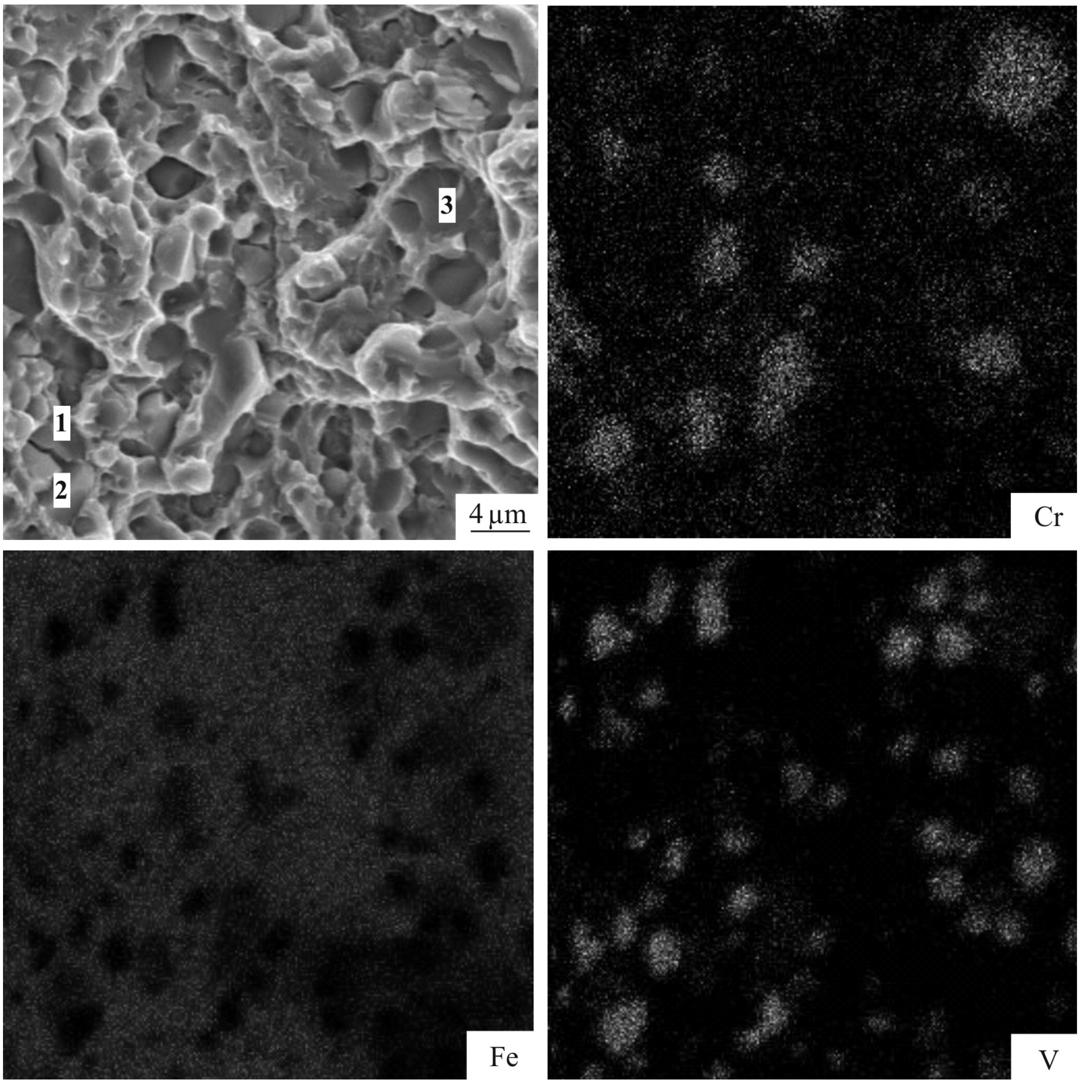

Figure 7: Fracture surface of the steel Vanadis 6 processed with a sub-zero period, fracture surface and EDS mapping for main alloying elements
Slika 7: Površina preloma jekla po obdelavi pod ničlo; prelomna površina in rasterski EDS-posnetek za osnovne legirne elemente

Three characteristic areas are marked. The first and second are carbide particles. The particle "1" was broken at fracture propagation. The particle "2" did not break and at the interface with the particle "1" decohesion is visible. The place "3" is a typical cleavage area in the matrix. EDX-mapping shows that the particle 1 is a chromium rich phase, probably of the M_7C_3-type. Its chemistry was estimated to 39 % Cr, 40 % Fe, 12 % V. The particle "2" contains more vanadium and less other elements – EDX fixed following chemistry: 13 % Fe, 61 % V, 9 % Cr. The cleavage region "3" can be referred as matrix with the chemical composition 89 % Fe, 6 % Cr, 1.7 % V.

4 CONCLUSIONS

The microstructure of the as-received material consisted of the matrix and carbide particles uniformly distributed in the material. The maximal size of particles is around 3 µm, but there are also particles with a size below of 0.5 µm (pearlitic carbides) are found.

After the heat-treatment the microstructure consists of the martensitic matrix, eutectic and part of secondary carbide particles. The amount of particles is smaller than in the as-received condition. For the heat processed material, the portion of carbide is slightly smaller for the specimens processed at higher austenitizing temperature.

The heat-treatment leads to a substantial hardness increase. With increasing austenitizing temperature the hardness increases, while, the sub-zero processing leads to slight decrease in hardness. This is rather surprising and inconsistent with earler observations. In this moment it is not clear why the sub-zero processing lowers the hardness of the steel Vanadis 6 steel and the explanation requires a more detailed investigation.

The three point bending strength decreases with the increasing austenitizing temperature. Also, with the application of sub-zero processing the three point bending strength is lowered.

The fracture toughness is lowered with increased austenitizing temperature. It is rather surprising that the sub-zero treatment increases the average fracture toughness slightly. Similarly to the hardness behaviour, this is not entirely clear and needs detailed TEM examination.

The fracture surfaces of the sub-zero- and the not sub-zero processed samples have similar basic characteristics. Both surfaces shown clearly dimple morphology. In some areas details of crack propagation like breaking of carbide particles and decohesion at the phase interfaces occur, also.

ACKNOWLEDGEMENTS

This work was done within the project ICDAM (INNOVATIVE CENTRE OF DIAGNOSTICS AND APPLICATION OF MATERIALS) and as a result of long-time scientific co-operation between IMT in Ljubljana and CTU in Prague.

5 REFERENCES

[1] Geller, J. A.: Instrumentaľnyje stali, 5. vyd., Metallurgija, Moskva, 1983

[2] Grgač, P.: Neue Hütte, 12 (**1989**), 459

[3] Fremunt, P., Krejčík, J., Podrábský, T.: Nástrojové oceli, Dum techniky Brno, 1994

[4] Spies, H.-J., Riese, A., Hoffmann, W.: Neue Hütte, 3 (**1990**) 3, 96

[5] Hnilica, F., Čmakal, J., Jurči, P.: Materiali in Tehnologije, 38 (**2004**) 5, 263

[6] Leskovšek, V., Ule, B.: J. Mater. Proc. Technol. 82 (**1998**), 89

[7] Berns, H., Fischer, A., Hönsch, W.: Härterei-Tech. Mitt., 45 (**1990**) 4, 217

[8] Berns, H., Bröckmann, C., Weichert, D.: Engineering Fracture Mechanics, 58 (**1997**), 311

[9] Olsson, L. R., Fischmeister, H. F. Powder Metalurgy, 1 (**1978**), 13

[10] Berns, H.: HTM, 29 (**1974**) 4, 236

[11] Kulmburg, A. et al.: HTM 47 (**1992**) 5, 318

[12] Stratton, P. F.: In.: Proc. of the 1st Int. Conf. on Heat Treatment and Surf. Eng. of Tools and Dies, Pula, Croatia, 8.–11. 6. 2005, 11–19

[13] Collins, D. N.: Heat Treatment of Metals 23 (**1996**), 2

[14] Meng, F. et al.: ISIJ International, 34 (**1994**) 2, 205–210

[15] Collins, D. N., Dormer, J.: Heat Treatment of Metals, 24 (**1997**) 3, 71–74.

[16] Šuštaršič, B., Leskovšek, V., Jutriša, G.: Materiali in Tehnologije, 37(**2003**), 369

[17] Z. W. Shan et al: Mechanical annealing and source-limited deformation in sub-micrometre-diameter Ni crystals, Nature Materials, 7 (**2008**), 115

[18] B. Ule, V. Leskovšek, B. Tuma: Estimation of plain strain fracture toughness of AISI M2 steel from precracked round-bar specimens, *Eng. fract. mech.*, 65(**2000**) 5, 559–572

[19] V. Leskovšek, B. Ule, B. Liščić: Relations between fracture toughness, hardness and microstructure of vacuum heat-treated high-speed steel, *J. mater. process. technol.*, 127 (**2002**), 298–308

[20] V. Leskovšek: Modelling of high-speed steels fracture toughness, *Mater. manuf. process.*, 24 (**2009**) 6, 603–609

UDK 669.14.018.298:539.4
Original scientific article/Izvirni znanstveni članek

ISSN 1580-2949
MTAEC9, 44(2)85(2010)

SURFACE MODIFICATIONS OF MARAGING STEELS USED IN THE MANUFACTURE OF MOULDS AND DIES

MODIFIKACIJA POVRŠINE JEKLA MARAGING IN UPORABA PRI IZDELAVI KOKIL IN UTOPOV

Franjo Cajner[1], Darko Landek[1], Vojteh Leskovšek[2]
[1]University of Zagreb, Faculty of Mechanical Engineering and Naval Architecture, Ivana Lučića 1, 10000 Zagreb, Croatia
[2]Institute of Metals and Technology, Lepi pot 11, 1000 Ljubljana, Slovenia
franjo.cajner@sb.hr

Prejem rokopisa – received: 2009-11-02; sprejem za objavo – accepted for publication: 2009-12-09

Low-carbon, high-alloy, precipitation hardening MARAGING steels have been developed in the early sixties of the last century as a high strength structural materials for application in aeronautical and missile engineering. Due to their excellent properties, such as: high hardenability, good toughness, and high resistance to thermal fatigue, and due to simple heat treatment (without protective atmosphere) with very small distortions, MARAGING steels are successfully used for the fabrication of moulds and dies. The main drawback of these steels is their relatively low wear resistance, particularly if the die is subjected to extensive wear during service. The paper presents an overview of existing MARAGING steels used in mould manufacturing and gives their general properties. Also, the results of the applied modification and coating processes are presented with a special focus on the increase in wear resistance.

Key words: MARAGING steels, thermo-chemical treatment, PVD coating, wear resistance

Malooglljična, visokolegirana in izločevalno utrjena jekla MARAGING so bila razvita v zgodnjih šestdesetih letih prejšnjega stoletja kot zlitine z visoko trdnostjo za uporabo v letalski in raketni tehniki. Zaradi izvrstnih lastnosti, kot so velika kaljivost, dobra žilavost, velika odpornost proti toplotni utrujenosti in enostavna toplotna obdelava (brez varovalne atmosfere) z majhnim krivljenjem, omogočajo učinkovito uporabo teh jekel tudi za izdelavo kokil in utopov. Njihova pomanjkljivost je majhna odpornost proti obrabi, še posebej, če je utopno orodje izpostavljeno veliki obrabi. V članku je pregled jekel vrst MARAGING, ki se uporabljajo pri izdelavi utopov, in njihovih lastnosti. Predstavljeni so tudi rezultati uporabljenih metod za obdelavo in prekritje površine s poudarkom na povečani odpornosti proti obrabi.

Ključne besede: jekla MARAGING, termo-kemična oddelava, PVD-prekritja, odpornost proti obrabi

1 INTRODUCTION

Low-carbon, high alloy MARAGING steels belong to the Fe-Ni-Co alloying system, using Mo, Ti, and Al as alloying elements. These steels were developed in the early sixties of the last century as high strength structural materials intended for application in aeronautical and aerospace engineering (e.g. for propeller drive shafts, pilot seat frames, liquid fuel tanks, armour plates, etc.). By modifying their composition with the addition of Cr (9–3 %), Fe-Ni-Cr or Fe-Ni-Co-Cr alloying systems were created, MARAGING steels belonging to these systems are suitable for the application in highly corrosive environments [2]. Later on, MARAGING steels started to be used for the manufacturing of tools, where are superior to other tool materials due to their superior properties [1–3]:

- High toughness and high fracture toughness combined with very high strength;
- High resistance to thermal fatigue;
- Protective atmosphere in heat treatment is not required, i.e. in solution annealing and precipitation hardening – aging, as there is no risk of decarburization and oxidation of the surface.
- Hardenability, even with the largest tool sizes, is achieved by slow cooling from the temperature of solution annealing; therefore, the risks of distortions and the occurrence of cracks caused by the difference in temperatures in the tool cross-section are significantly reduced.
- Good weldability;
- Good electro-erosion machinability;
- Good chip machinability and/or cold deformability after quenching enable the tool manufacturing to the end dimensions before the final heat treatment (aging) is completed.
- In solution annealing and in cooling, the expected shortening is approximately 0.1 %, and in the final heat treatment (aging), there are practically no deformations; therefore, these heat treatment processes can be considered as processes causing no distortion.
- Compared to the conventional heat treatment of tool steels, the heat treatment of MARAGING steels (solution annealing and aging) is much simpler.

The main disadvantage of MARAGING steels compared to high alloy tool steels is their relatively low hardness (*HRC* = 50–57 at the most), and consequently the insufficient resistance to wear. Due to their lower hardness, MARAGING steels are not suitable for the manufacture of cutting tools, but are suitable for the manufacture of moulds and dies (for die-casting and for polymer processing), of forming tools, etc. [1,2]. A relatively high price of MARAGING steels (they are several times more expensive than the high alloy tool steels produced by standard methods) cannot be taken as a major drawback in modern machine tool industry since tool steels produced by powder metal forming have a similar price.

In references [3–5], the application of nitriding and/or nitrocarburising is usually recommended to improve the wear resistance. The investigation of the application of other thermo-chemical treatments (carburizing, boriding) and of vapour deposition coating processes [6–10] seems to be a natural choice. Results found in literature and results of our research on the possibility of improving the wear resistance of MARAGING steels are presented in this work.

2 PROPERTIES OF MARAGING TOOL STEELS

Iron-nickel phase diagram and the influence of the content of nickel on the hardness in the solution-annealed steels (**Figure 1**) can contribute to the understanding of the hardening mechanism of MARAGING steels. **Figure 1 a**, shows that the alloy with approximately 18 % Ni will be in the single-phase austenite area above the temperature of 650 °C (generally the temperature of austenization-homogenization is approximately of 820 °C). With this content of nickel, the alloy exhibits the highest strength after cooling (**Figure 1b**). As the solution annealed MARAGING steel is cooled from the temperature of annealing to approximately 250 °C (slow cooling in the air is sufficient), the low-carbon nickel-martensite, which is actually an oversaturated solution of Co, Mo, Ti and Al in the alloy Fe-Ni-(Co), starts to form. The transformation of austenite into nickel-martensite is completed at a temperature of approximately 200 °C; and at this temperature, the microstructure should be without residual austenite. Nickel-martensite (with a hardness of approx. *HV* 300) can be easily machined by the chips removal and by deformation machining and can even be welded, if necessary.

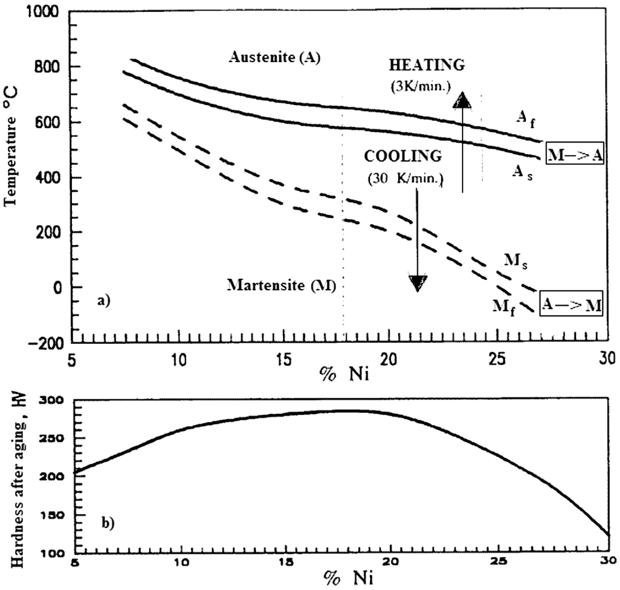

Figure 1: a) Real phase diagram Fe-Ni [11], b) Quenching hardness of Fe-Ni alloys in dependence of the percentage of nickel (with the addition of Co, Mo, Ti, and Al) [12]

Slika 1: a) Realni fazni diagram Fe-Ni [11], b) Kalilna trdota zlitin Fe-Ni v odvisnosti od vsebnosti niklja (z dodatkom Co, Mo, Ti in Al) [12]

The solution annealing of MARAGING steels is carried out in steel mills, and the manufacturer of a machine part or a tool carries out only the final heat treatment (aging) after the machining to the specified dimensions. The process of aging is performed in furnaces without protective atmosphere and at relatively low temperatures (approx. 500 °C). In the slow cooling process that follows, small distortions occur. In the age hardening process, a large number of finely dispersed precipitates of intermetallic phases occur (e.g. Ni_3Al, Ni_3Ti, Fe_2Mo, FeCr, and Fe_7Mo_6) in nickel martensite, which results in an increase in steel hardness from *HV* = 280–380 to *HV* = 500–650. Also, the tensile strength of the steel is increased to 4200 N/mm², and deformability and fracture toughness are rather good [1–4]. **Figure 2** gives a flow diagram of the heat treatment process of MARAGING steels.

Table 1 lists several grades of MARAGING tool steels divided into three groups according to their resistance to elevated temperatures and corrosion [2]:

a) steels suitable for hot working at temperatures of up to 425 °C: X 3 NiCoMo 18 8 5, X 3 NiCoMo 18 9 5, X 2 NiCoMoTi 18 12 4
b) steel suitable for hot working at temperatures of up to 600 °C: X 2 NiCoMo 12 8 8
c) steels with superior corrosion stability: X 1 CrNiCoMo 9 10 3, X 1 CrNiCoMo 13 8 5, X 2 CrNiCoMo 12 8 5

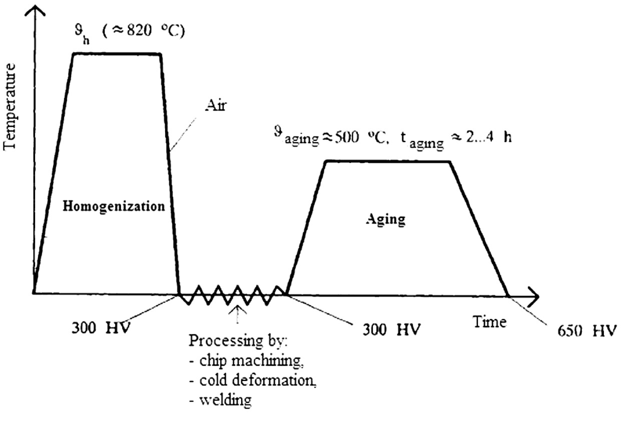

Figure 2: A flow diagram of the heat treatment process of MARAGING steels [2]

Slika 2: Diagram poteka procesa toplotne obdelave jekel MARAGING jekel [2]

Table 1: MARAGING tool steels [2]
Tabela 1: Jekla MARAGING [2]

Resistance to temperature / corrosion	Steel grade	Heat treatment		Mechanical properties									
				after solution annealing (homogenization)					after aging				
		Homogenization temperature, °C	Aging temperature, °C/ /Aging time, h	R_m/MPa	$R_{p0.2}$/MPa	max. *HV*	min. A_5/%	min. $KV_{20°C}$/J	R_m/MPa	$R_{p0.2}$/MPa	max. *HV*	min. A_5/%	min. $KV_{20°C}$
<425 °C	X3 NiCoMo 18 8 5	820	480 / 3	1130	830	350	15	60	1920	1720	500	8	20
	X3 NiCoMo 18 9 5	820	480 / 3	1130	830	350	15		1960	1910	570	7	30
	X2 NiCoMoTi 18 12 4	820	500 / 6	1130	830	350	15		2350	2260	590	6	10
<600 °C	X2 NiCoMoTi 12 8 8	900	550/ 2						1980	1800	560		
Corrosion resistance	X1 CrNiCoMo 9 10 3	835	480 / 6						1500	1400		12	60
	X1 CrNiCoMo 13 8 5	820	480 / 6						1700	1500		11	50
	X2 CrNiCoMo 12 8 5	880	480 / 6	1000	700				1870	1650		10	40

Table 2: Chemical composition of MARAGING steel 14 10 5
Tabela 2: Kemična sestava jekla MARAGING 14 10 5

w/%															
C	Si	Mn	P	S	Cr	Mo	Ni	V	Al	Cu	Ti	Nb	N	B	Co
0.01	0.88	0.087	0.003	0.002	0.11	4.81	13.60	0.024	0.14	0.08	0.17	0.10	0.013	0.002	9.50

MARAGING steels suitable for working at temperatures of up to 425 °C have a rather low resistance to high temperatures since austenite, which decreases the hardness and strength in operating conditions, is recreated already at the temperature of 500 °C [13]. Therefore, these steels are used for tools used in cold and lower temperature operating conditions, such as. [2]:

- moulds for polymer processing
- dies for the die casting of silumin or zinc alloys
- punches for the extrusion of lead cable sheaths
- tools for compression-extrusion of Al-alloys
- matrices and punches for the cold forging of bodies and heads of bolts.

The MARAGING steel suitable for hot working at temperatures of up to 600 °C (X 2 NiCoMo 12 8 8) has a lower content of Ni than the steels with 18 % Ni. Therefore, it has to be solution annealed at a temperatures of approximately 900 °C (**Figure 1**) and also precipitation hardened (aged) at temperatures of up to 625 °C. The increased content of Mo (from 5 % to 8 %) has also a beneficial influence on the increase in hardness during the aging process by additional precipitation of Ni_3Mo. Due to the improved resistance to thermal fatigue, this steel grade can be recommended for the manufacture of mould components for the die casting of aluminium alloys [2].

MARAGING steels with improved corrosion stability have a lower content of nickel (from 8 % to 10 %) and cobalt Co (from 3 % to 5%) and contain between 9 % to 13 % of chromium (as an active corrosion resistant ingredient, chrome contributes to the improved corrosion resistance). The addition of chromium decreases the hardness, as well as the strength (to approximately 1600 N/mm^2) and the yield stress (to approx. 1500 N/mm^2). It decreases also, the temperatures of the start (M_s) and the finish (M_f) of the formation of nickel-martensite. Therefore, with these steels, retained austenite may occur after quenching and a need for deep cooling may arise. MARAGING steels high-alloyed by chrome can be recommended for the manufacture of mould components for the processing of highly corrosive polymers.

3 IMPROVED WEAR RESISTANCE

In reference, results of research into the feasibility of the application of various surface treatment procedures (nitriding, carburizing, boriding, and PVD coating) in order to improve the wear resistance of MARAGING steels are found [3,6,7,9,10,11,12,13]. Our investigations [6,9] on the MARAGING steel 14 10 5 (**Table 2**) included the following surface treatment procedures: nitriding in Tenifer salt bath, nitriding in plasma gases, as well as carburizing and boriding according to the parameters listed in Table III. In addition, a possible application of the duplex treatment of plasma nitriding and of physical vapour deposition (PVD) procedure has been investigated also. In **Table 3** the performed researches are summarised and all heat treatment parameters applied are listed.

The effect of processes of modification and coating on the properties of MARAGING steel 14 10 5 has been estimated with microstructure, hardness distribution on

Table 3: Heat treatment of test samples made of MARAGING steel 14 10 5

Tabela 3: Toplotna obdelava preizkušancev iz jekla MARAGING 14 10 5

Heat treatment parameters	
Solution annealed at 820 °C/1h/air	Aged at 500 °C/4h
	Nitrocarburized by the TENIFER procedure at 580 °C/4h
	Ion-nitrided at 500 °C/72h
	Ion-nitrided at 500 °C/20h
	Ion-nitrided at 500 °C/20h + PVD coated at 450 °C/70 min
	Carburized in the Degussa KG 6 granulate at 900 °C/4h + aged at 500 °C/4h
	Borided in the EKABOR 2 (Degussa) powder at 900 °C/4h + aged at 500 °C/4h

the cross-section and tribological tests (abrasive, erosive and adhesive wear). **Figures 3 to 8** present the results of these tests. The testing of resistance to abrasive wear was carried out by the dry sand/rubber wheel tests (Ottawa 50/70 quartz sand) at a compressive force of 45 N (**Figure 4**). The same sand type was used in the tests of erosive wear with sand grains colliding with the test sample surface at an angle of incidence of 90° (**Figure 6**). Tests of abrasive wear were carried out by a friction ring made of hardened steel at the compressive force of 100 N. During testing, values of friction coefficient were determined (**Figure 8**). Details on the conducted tests are given in [9,10].

3.1 Carburization of MARAGING steels

The carburization of MARAGING steels was carried out at the temperatures of solution annealing. After the cooling process, high-carbon martensite with increased hardness (and a probable presence of residual/retained austenite) is obtained in the boundary layer. The total depth of carburized layer on the MARAGING steel 14 10 5 was approx. 0.8 mm. The subsequent aging improved the core hardness, and reduced the hardness of the carburized layer (**Figure 3**). The carburization of MARAGING steels improved their resistance to abrasive wear compared with the solution annealed and aged condition or with that of solution annealed and nitrided (**Figure 4**). The carburization of MARAGING steels also has some adverse effects. The formation of a hard martensite layer (with hardness of approx. *HV* 700) is accompanied with additional distortions and by a more difficult chip machining. Thus, one of major advantages of MARAGING steels, i.e. the heat treatment without distortions, is lost.

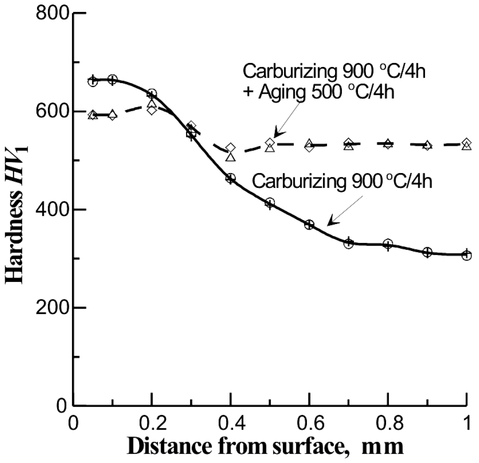

Figure 3: Hardness distribution in the edge layer of carburized test samples made of MARAGING steel 14-10-5

Slika 3: Porazdelitev trdote ob površini naoogljičene plasti pri preizkušancu iz jekla MARAGING 14 10 5

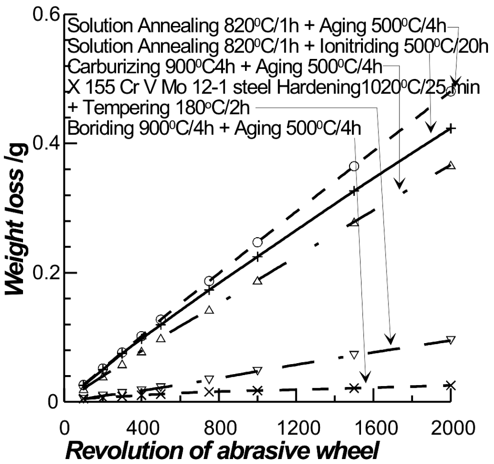

Figure 4: The abrasive wear mass loss of test samples made of MARAGING steels 14-10-5 with and without surface modifications compared with the wear of samples made of high alloy tool steel X155CrVMo12 1 [9,10]

Slika 4: Izguba mase zaradi abrazivne obrabe preizkušancev iz jekla MARAGING 14 10 5 z modifikacijo površine in brez nje v primerjavi s preizkušanci iz močno legiranega orodnega jekla X155CrVMo 12 1 [9,10]

3.2 Boriding of MARAGING steels

The boriding of MARAGING steel 14 10 5 by using the standard means and parameters results in a boride

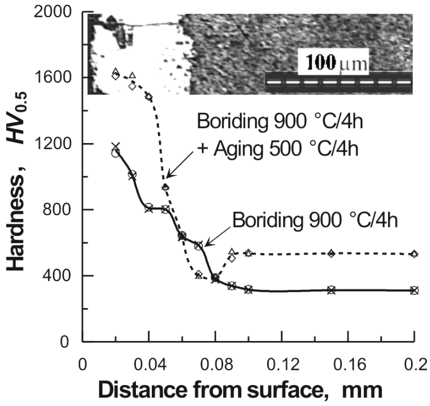

Figure 5: The microstructure and hardness distribution in the edge layer of borided test samples made of MARAGING steel 14-10-5 [10]

Slika 5: Mikrostruktura in porazdelitev trdote v robni plasti boriranih preizkušancev iz jekla MARAGING 14 10 5 [10]

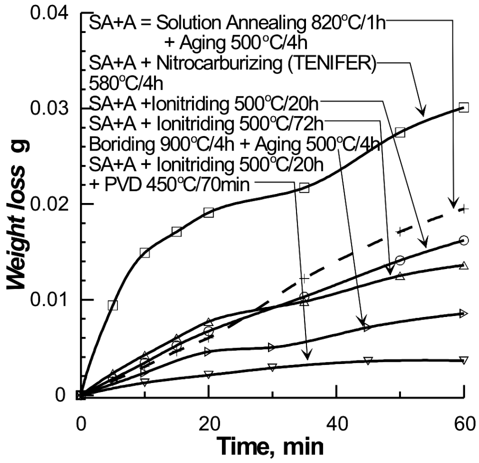

Figure 6: Mass loss in erosive wear tests carried out on test samples made of MARAGING steel 14-10-5 with and without surface modifications [10]

Slika 6: Izguba mase pri preizkusih erozivne obrabe preizkušancev iz jekla MARAGING 14 10 5 z modifikacijo površine in brez nje [10]

layer with a thickness of approx. 50 μm and with high hardness (above $HV_{0.5}$ 1000) (**Figure 5**). This layer showed a high resistance to erosive wear and an improved resistance to abrasive wear, even higher than that of highly wear resistant ledeburite steel for cold working (**Figure 4 and 6**). Along with these obvious advantages, one should also notice the problems in the application of the boriding of MARAGING steels, such as the occurrence of a soft zone below the boride layer, the presence of transverse cracks in the boride layer, and the risk of exceeding dimensional tolerances. Due to the achieved high hardness after boriding (prior to aging), it is not possible to correct dimensions and thus the property of "distortionless" heat treatment is lost.

3.3 Nitriding of MARAGING steels with and without a subsequent PVD coating procedure

An increased wear resistance of MARAGING steels can be successfully obtained by plasma nitriding [6,9,13,14] at temperatures of approximately 500 °C, which are in the range of aging temperatures of these steels. The application of solution annealing and plasma nitriding results in an improved resistance to abrasive and erosive wear compared with the application of standard solution annealing and aging (**Figure 4 and 6**). Also, all the other advantages of the application of MARAGING steels pointed out before are retained. Research results reported in [13] show that the corrosion resistance of MARAGING steels exposed to salt mist (salt-spray test with exposure of the test sample to the aqueous solution of sodium chloride at a concentration of 5 % NaCl) is increased by three times if plasma nitriding is applied compared to the solution annealed and aged condition. This result is expected in all the cases in which a zone of compounds (Fe nitrides) is formed on the MARAGING steel surface. Here, the formation of a single-phase layer of Fe_4N nitrides is recommended since, according to [14], these layers exhibit a good combination of high hardness and ductility.

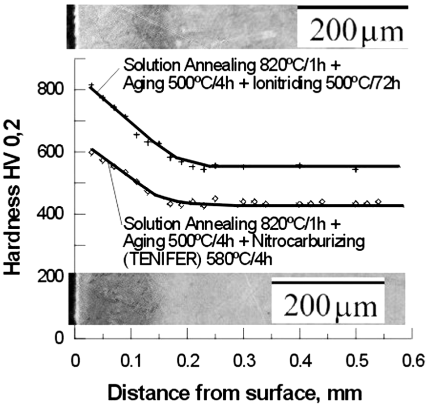

Figure 7: Microstructure and hardness distribution in the edge layer of test samples of MARAGING steel 14-10-5, nitrided in plasma and nitrocarburized in the TENIFER salt bath [10]

Slika 7: Mikrostruktura in porazdelitev trdote v robni plasti preizkušancev iz jekla MARAGING 14 10 5, ki so bili nitrirani v plazmi in karbonitrirani v solni kopeli TENIFER [10]

The application of nitriding and nitrocarburizing in gases, as well as nitrocarburizing in the Tenifer salt bath results in the overaging of the core due to a higher temperature of the treatment (550–600 °C). This phenomenon is reflected in hardness decrease of the base metal and in the hardness of the nitrided layer (**Figure 7**). The overaging of the core can have an influence on the decrease in the resistance to abrasive and erosive wear (**Figure 6**) [9,10].

The duplex treatment of plasma nitriding and of the physical vapour deposition (PVD) procedure seems to be of a particular interest regarding the improvement in wear resistance. In the case of the tested MARAGING steel 14 10 5, the thickness of the PVD TiN coating was 1.8 μm (**Figure 8**). In the plasma nitriding treatment it is possible to vary the parameters of the procedure in order

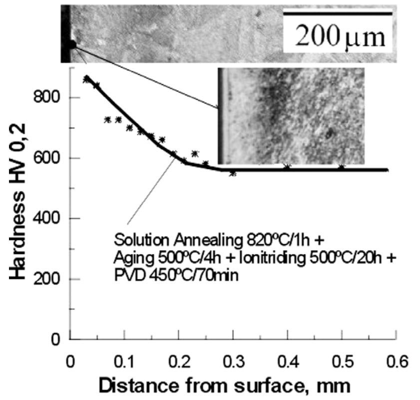

Figure 8: Microstructure and hardness distribution in the edge layer of test samples made of MARAGING steel 14-10-5, nitrided in plasma and coated by a PVD TiN coating [10]

Slika 8: Mikrostruktura in porazdelitev trdote v robni plasti preizkušancev iz jekla MARAGING 14 10 5, ki so bili nitrirani v plazmi in pokriti s plastjo PVD TiN [10]

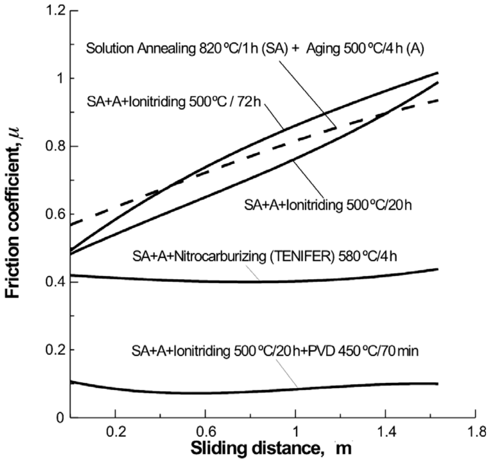

Figure 9: Friction coefficient determined in the adhesive wear testing of test samples made of MARAGING steel 14-10-5 with and without modifications of the surface [10]

Slika 9: Koeficient trenja pri preizkusu adhezivne obrabe preizkušancev iz jekla MARAGING 14 10 5 z modifikacijo površine in brez nje [10]

to obtain a boundary layer with or without a zone of compounds, and the PVD treatment produces a hard coating with the properties of a high resistance to abrasive, erosive and adhesive wear, together with an extremely low friction coefficient (**Figure 4 and 9**).

3.4 Repair of worn tools from MARAGING steels

Low carbon MARAGING steels can be welded, which is a good basis for the repair of worn tool surfaces and those with thermal fatigue cracks. A description of a successful welding procedure and the closure of surface microcracks in the MARAGING steel X 2 NiCoMoTi 12 8 8 with laser remelting (using a diode laser) without using a filler metal is given in [15]. Diode lasers with beam power of 1 kW to 2 kW are compact and easily controlled sources of light beams suitable for the repair and maintenance of tool surfaces, especially of large and expensive tools, such as moulds for die casting, dies, tools for pressing polymers, etc. For each repair case and type of MARAGING steel, one has to determine appropriate operating parameters, such as the power output and shift of the laser beam and its focusing points, the depth of remelting, and other parameters.

Diode lasers can find their application not only in tool repair procedures for remelting tool surfaces, but also in the manufacture of tools made of MARAGING steels in order to improve the wear resistance of the surface by applying coating and alloying procedures.

4 CONCLUSION

Good mechanical and technological properties and the heat treatment with almost no distortions make MARAGING tool steels suitable for the manufacture of moulds used in polymer processing, of dies for die-casting, drop-hammer dies, punches, matrices, and other non-cutting tools. In addition to the basic group of MARAGING steels with 18 % Ni, two special groups of steels resistant to temperatures of up to 600 °C and those used for tools exposed to corrosion have been developed.

In the investigation, it is confirmed that the rather poor wear resistance of MARAGING steels can be improved with thermo-chemical heat treatments, as nitriding, nitrocarburizing, boriding and carburizing.

The carburizing process improve the resistance to abrasion, however it cannot be recommended as a heat treatment process for the surface modification of these steels because the risk of exceeding the required dimensional tolerances and of shape changes (similarly as in the case of boriding) and the chip machining to be conducted prior to aging is made more difficult (thus, a major advantage has been lost).

The process of boriding significantly improves the resistance to abrasive and erosive wear, but transverse cracks occurring in the boride layer, a change in dimensions and the loss of "distortionless" heat treatment make this process, for the time being, unsuitable for the manufacture of tools.

Nitrocarburizing in gases and in salt baths produces good-quality layers, but since the process is carried out at very high temperatures (550–600 °C), this causes a significant decrease in the core hardness of standard MARAGING steels. This fact should be taken into account when the application of these processes is considered.

Plasma nitriding is the most suitable heat treatment process for the processing of MARAGING steels because the temperature of nitriding can be lower than (or equal to) the optimum temperature of ageing. Therefore, the process of ageing can be carried out during nitriding. As far as an improved resistance to abrasive, erosive and adhesive wear is concerned, the plasma nitriding of MARAGING steels proves to be more effective than solution annealing and aging, but still less effective than carburizing and boriding. It is to be expected that further improvements and the optimization of plasma nitriding parameters will produce layers with even a higher resistance to wear. In addition to the already mentioned advantages of the procedure, plasma nitriding results in some other favourable properties, such as an improved resistance to thermal fatigue, improved corrosion stability, and improved resistance to adhesion of the processed molten mixture. All this contributes to a conclusion that this procedure can be recommended in the manufacture of moulds made of MARAGING steels used for the processing of polymers and metals

Significant improvements in the resistance to erosion and adhesion of MARAGING steel 14 10 5 achieved by plasma nitriding followed by coating the metal by a TiN layer speak in favour of the application of this combination of processes for the manufacture of moulds that have to meet the requirement of an increased wear resistance.

It is expected that laser beams used for the modification and coating of surfaces will find their application in the manufacture of tools and in the repair of worn tool surfaces made of MARAGING steels, particularly if compact and portable diode lasers are used.

5 LITERATURE

[1] Novosel M., Cajner F., Krumes D.: Tool Materials, Faculty of Mechanical Engineering in Slavonski Brod, Slavonski Brod, Croatia, 1996 (book published on croatian)

[2] Cajner F., Krumes D.: MARAGING steels – new tool materials, Proceedings of symposium Modern technologies of heat treatment of steels, Zagreb, Croatia, 11. 6. 1998, 69–80

[3] ASM Handbook, Part 4, ASM International, Metals Park, Ohio, 1994

[4] Heberling J. M.: MARAGING steel: A dependable alloy, Heat Treating, (**1993**), Sept., 22–24

[5] Decker, R. F.: MARAGING steels: Getting better with age, AMP Metal Progress (**1988**) 6, 45–50

[6] Novosel M:, Cajner F.: Applicability of thermochemical treatment for MARAGING steels and use for manufacturing of the moulds for polymer processing, Proceedings of the 13th days of Polymer and Rubber Society, Zagreb, Croatia, 1995, 3–12

[7] Cajner F., Leskovšek V.: Influence of thermochemical treatment of MARAGING steel on wear resistance, Proceeding of international conference MATRIB'99, Trogir, Croatia, 1999, 15–22

[8] Kladarić, I., Cajner F., Krumes D.: Optimization of Parameters for Ageing of MARAGING Steel, Proceedings of the 8th Seminar of the International Federation for Heat Treatment and Surface Engineering, Dubrovnik-Cavtat, Croatia, 12–14. September 2001, 111–117

[9] Cajner F.; Landek D. Kladarić I.: Improvement of wear resistance of MARAGING steel by applying thermochemical processes, Proceedings of the 1st International Conference on Material & Tribology 2002., Dublin, Ireland, 2002

[10] Cajner F., Landek, D. Šolić S., Cajner H.: Effects of thermochemical treatments on properties of MARAGING steels, Surface Engineering, 22 (**2006**) 6, 468–471

[11] Johs F. W., Pumphrey W. I.: Free energy and metastabile in the iron-nickel and iron-manganese systems, Journal Iron and Steel Institute, 163 (**1949**), 121–128

[12] Goldštejn M. J., Gračev S. V., Veksler Y. G.: Specijalnie stali, Metalurgija, Moskva, 1985

[13] Shetty, K., Kumar, S., Raghothama, R.: Effect of ion nitriding on the microstructure and properties of Maraging steel (250 Grade), Surface & Coatings Technology 203 (**2009**), 1530–1536

[14] Yan, M.F., Wu, J. Y., Liu, R., L.: Plasticity and ab initio characterizations on Fe_4N produced on the surface of nanocrystallized 18Ni-maraging steel plasma nitrided at lower temperature, Applied Surface Science 255 (**2009**), 8902–8906

[15] Grum, J., Slabe, J. M.: Effect of laser-remelting of surface cracks on microstructure and residual stresses in 12Ni maraging steel, Applied Surface Science 252 (**2006**), 4486–4492

UDK 669.1.621.74
Original scientific article/Izvirni znanstveni članek

ISSN 1580-2949
MTAEC9, 44(2)93(2010)

TWO NUMERICAL MODELS OF THE SOLIDIFICATION STRUCTURE OF MASSIVE DUCTILE CAST-IRON CASTING

NUMERIČNA MODELA STRUKTURE STRJEVANJA MASIVNEGA DUKTILNEGA ŽELEZOVEGA ULITKA

Karel Stransky[1], Jana Dobrovska[2], Frantisek Kavicka[1], Vasilij Gontarev[3], Bohumil Sekanina[1], Josef Stetina[1]
[1]Faculty of Mechanical Engineering, Brno University of Technology,Technicka 2, 616 69 Brno, Czech Republic
[2]VSB – Technical University of Ostrava, Tr. 17. listopadu, 708 33 Ostrava, Czech Republic
[3]University of Ljubljana, Aškerčeva 12, 1000 Ljubljana, Slovenia
stransky@fme.vutbr.cz

Prejem rokopisa – received: 2009-07-02; sprejem za objavo – accepted for publication: 2009-11-26

An original three-dimensional (3D) model of solidification is used to describe the process of solidification and cooling of massive (500 × 1000 × 500) mm cast-iron sand moulds castings. The calculated mode of the kinetics of the temperature field of the casting was verified during casting with temperature measurements in selected points.
The sizes and positions (x_i, y_i, z_i, where i = 1, 2, 3 is the number of samples taken) of the experimental samples are exactly defined and corresponding with the decreasing rate of solidification. The experimental samples – 15 mm in diameter and 12 mm high – were metallographically analysed and also in terms of heterogeneity of chemical composition. The coordinates x_i, y_i, z_i characterise approximately – within an accuracy of ±5 mm – the centres of the samples. Successively, the local solidification time Θ (i.e. the time the specified position of the casting, defined by the coordinates x_i, y_i, z_i, remained within the temperature range between the liquid and solid curves) is also calculated using the 3 D model. The following dependences are later determined according to experimental and calculated data: the average size of graphite spheroids r_g and of graphite cells R_b as well as the average distances among the particles of graphite L_g – always as function of the local solidification time Θ [x_i, y_i, z_i]. Furthermore, it was founded that the given basic characteristics of the structure of the cast iron r_g, R_b and L_g are directly proportional to the logarithm of the local solidification time. The original spatial model of solidification can therefore be used therefore as first approximation for the assessment of the casting structure of massive cast iron parts. This paper creates the starting point for the estimation of the local mechanical properties and fracture behaviour of massive ductile cast iron castings.

Keywords: ductile cast-iron, solidification time, segregation, structural characteristics, model

Za opis procesa strjevanja in ohlajanja masivnih železovih ulitkov velikosti (500 × 1000 × 500) mm smo uporabili osnovni tridimenzionalni (3 D) model strjevanja. Ulitki so bili uliti v peščene forme. Izračunan kinetični model temperaturnega polja ulitka je bil preverjen med ulivanjem z meritvami temperature v izbranih točkah.
Velikosti in lege (x_i, y_i, z_i, kjer je i = 1, 2, 3 število vzetih vzorcev) poskusnih vzorcev so bile točno določene in so v skladu s padajočo hitrostjo strjevanja. Poskusni vzorci premera 15 mm in višine 12 mm so bili metalografsko analizirani in preverjena je bila tudi heterogenost kemijske sestave. Koordinate x_i, y_i, z_i označujejo sredino vzorcev s približno z natančnostjo ±5 mm. Lokalni čas strjevanja Θ (t. j. čas določenega položaja v vzorcu, definiranega s koordinatami x_i, y_i, z_i ostaja v temperaturnem območju med likvidusno in solidusno krivuljo) je bil tudi izračunan z uporabo 3D-modela. Kasneje so bile določene naslednje odvisnosti glede na eksperimentalne in izračunane podatke: srednja velikost kroglastega grafita r_g, grafitnih celic R_b in srednje razdalje med delci grafita L_g – vedno kot funkcije lokalnega časa strjevanja Θ [x_i, y_i, z_i]. Nadalje je bilo ugotovljeno, da so dane značilnosti strukture litega železa r_g, R_b in L_g direktno sorazmerne z logaritmom lokalnega časa strjevanja. Osnovni prostorski model strjevanja lahko tako uporabimo v prvem približku za ugotovitev lite strukture masivnih železovih ulitkov. Ta članek omogoča začetno stopnjo ocene lokalnih mehanskih lastnosti in vedenja pri zlomih masivnih duktilnih železovih ulitkov.

Ključne besede: siva litina s kroglastim grafitom, čas strjevanja, izcejanje, značilnosti strukture, modeliranje

1 INTRODUCTION

The problem of optimisation of properties and production technology for the casting of massive ductile cast-iron (spheroidal graphite) castings had been investigated into in the past few years and, besides an extensive number of publications both nationally as well as internationally, the results of the investigations have been published in the final report of this investigation [1]. During the investigations, the centre of focus were not only the purely practical questions relating to metallurgy and foundry technology, but mainly the verification of the possibility of applying two original models – the 3 D model of transient solidification and cooling of a massive cast-iron casting and the model of chemical and structural heterogeneity. Both models have only been applied to describing the temperature field, the control of solidification and the cooling of continually cast steel slabs, to the descriptions of their chemical heterogeneity and to determining the basic characteristics of their microstructure. The model of chemical and structural heterogeneity seems to be a suitable partner of the 3D model of the transient temperature field [2].

The original model and also an original application of the software ANSYS were one of the outcomes of this research. In this combination, it is possible to optimise the technology of casting cast-iron parts and successive cooling in order to achieve the most convenient microstructure. This includes a microstructure of spheroids of graphite, preferably with as high a density as possible and spread throughout the casting as evenly as possible, with a minimal ratio of particles of graphite marked as degenerated shapes.

The appropriate density of the spheroids of graphite is simultaneously one of the conditions of good mechanical properties of castings of ductile cast-iron, especially good ductility and contraction while maintaining good strength properties – yield point and tensile strength.

The discussed 3D model establishes a system via which it is possible to pre-simulate the method of eutectic crystallisation of the melt of ductile cast-iron. With the liquidus and solidus known, it is also possible – in selected parts of the casting (that would be suitably discretised) – to determine the time the temperature of the relevant part of the metal remained between the liquidus and solidus. This region is characterised by the coexistence of solid and liquid states – the so-called 'mushy zone'.

In describing the solidification of steel, the time for which the metal remains at a temperature between the liquidus and solidus is called the local solidification time, and the volume of metal corresponding to this time determined by the sizes of the dendrites [3,4]. When describing the solidification of cast-iron, including cast-iron with spheroidal graphite, the term 'local solidification time' has not been used, even despite the fact that the eutectic crystallisation of grey cast-iron always runs within a certain temperature interval and naturally even a time solidification interval dependent on time.

2 AIMS AND METHODOLOGY

The massive experimental cast-iron castings, produced within the research [5], had the following dimensions: width × length × height = (500 × 1000 × 500) mm. The verifying numerical calculation of the local solidification times θ/s – conducted according to the 3D model proved that, along the height, width and length of these massive castings, there are various points with differences in the solidification time of up to two orders.

The aim was to verify the extent to which the revealed differences in the local solidification time affect the following parameters:

a) The average size of spheroidal graphite particles;
b) The average density of spheroidal graphite particles;
c) The average dimensions of graphite cells, and
d) The chemical heterogeneity of elements in the cross-sections of individual graphite cells.

The relationships – among the given four parameters and the corresponding local solidification time – were determined in the series of samples that had been selected from defined positions of the massive casting.

2.1 Experimental cast-iron casting and selection of samples

The experimental casting was selected from a series of three castings and it was marked as casting No.1 [5]. The bottom part of its sand mould was lined with (a total number of) 15 cylindrical chills of a diameter of 150 mm and a height of 200 mm. The upper part of the mould was not lined with any chills. The average chemical composition of the cast-iron before casting is given in **Table 1**.

A (500 × 500 × 40) mm plate had been mechanically cut out of the middle of the length by two parallel transversal cuts. Then, further samples were taken from exactly defined points and tested in terms of their structural parameters and chemical heterogeneity. Samples in the form of testing test-samples for ductility testing, with threaded ends, were taken from the bottom part of the casting (A), from the middle part (C) and from the upper part (G). The 15 mm in diameter and 12 mm high cylindrical samples served the actual measurements in order to determine the structural parameters and chemical heterogeneity.

Table 1: Chemical composition of ductile cast-iron
Tabela 1: Kemijska sestava duktilne železove litine

Element	C	Mn	Si	P	S	Ti	Al	Cr	Ni	Mg
w/%	3.75	0.12	2.15	0.039	0.004	0.01	0.013	0.07	0.03	0.045

Table 2: Measured and calculated structural parameters and the coordinates *x, y, z* of the measured samples
Tabela 2: Merjeni in izračunani strukturni parametri ter koordinate *x, y, z* merjenih vzorcev

Sample	r_g/ μm	R_b/ μm	L_g/ μm	r_{ghm}/ μm	R_{bhm}/ μm	L_{ghm}/ μm	x/ mm	y/ mm	z/ mm	θ_{ls} / s	$\bar{I}_{het}$	$\bar{I}_s$
A	27.6 ± 3.6	82.8	165.6	28	83	110	190	50	507.5	48	0.952	3.34
C	36.4 ± 10.4	103.9	207.7	36	104	136	190	210	507.5	2509	1.091	4.52
G	38.9 ± 12.5	109.3	218.6	39	109	140	190	450	507.5	4542	0.916	3.98

Note: r_g, R_b, L_g – metallographic analysis (measured), r_{ghm}, R_{bhm}, L_{ghm} – chemical micro-heterogeneity (selected for analysis), $L_{ghm} \approx 2R_b - 2r_g$, θ_{ls} – local solidification time, $\bar{I}_{het}$ – arithmetic mean of heterogeneity index, $\bar{I}_s$ – arithmetic mean of segregation index of ten measured elements

In the points of the defined positions of the samples prepared in this way, the quantitative metallographic analysis was used to establish the structural parameters of cast-iron [6], the in-line point analysis to establish the chemical composition of elements [7] and numerical calculation using the 3D model to establish the local solidification time [1].

2.2 Quantitative metallographic analysis

Quantitative analysis of the basic micro-structural parameters in the samples, i.e. the radius of the spheroids of graphite – r_g, the distances between the particles of graphite – L_g and the radius of the graphite cells – R_b had been the subject of a special study [4]. The measurement of the size parameters of the graphite had been conducted on the Olympus CUE4 image analyzer under standard conditions, i.e. with a magnification of 100-times and on each sample a total number of 49 views were evaluated. The measurement results are given in **Table 2**.

2.3 Chemical heterogeneity of samples

The concentration of elements in each of the samples was measured between two particles of spheroidal graphite. The analyzed region in the sample structure had been selected in order for the structural parameters of graphite (r_{ghm}, R_{bhm}, L_{ghm} within the analyzed region) to approach the average parameters of graphite within the sample (r_g, R_b, L_g) measured using quantitative metallographic analysis. The differences of the average values of the parameters in the structures of samples and of parameters selected for analysis of their chemical micro-heterogeneity of elements are based on the comparison of values in **Table 2**. Then differences occur only between the values of L_g and L_{ghm}, which is given by the fact that parameter L_g represents the average distance between the particles of spheroidal graphite, whereas parameter L_{ghm} represents the measured length of the line between the edges of the graphite within the matrix. This distance was selected in order for the following relation to apply: $L_{ghm} \approx 2R_b - 2r_g$. The actual measurements of concentrations of ten elements – Mg, Al, Si, P, S, Ti, Cr, Mn, Fe, Ni – was carried out on the JEOL – JSM 840/LINK AN 10/85S analytical complex with an energy dispersive X-ray analyzer, an acceleration voltage of the electron beam of 25 kV and exposition time of 50 s. On each of the samples, the concentrations of all ten elements had been measured in three intervals with each individual step being 3 μm. By means of the Neophot light microscope, the interval was documented within which the concentrations were measured. The method of selection of measurement points is illustrated in **Figures 1** and **2** (from the same sample). The results of measurements of the chemical heterogeneity of elements in cells were evaluated also statistically with the aim to be able to predict the values of two parameters: the element heterogeneity index I_{het} (which is defined as the quotient of its standard deviation and its arithmetic mean) and the element segregation index I_S (which is defined as the quotient of maximal concentration of elements in the cell and its arithmetic mean).

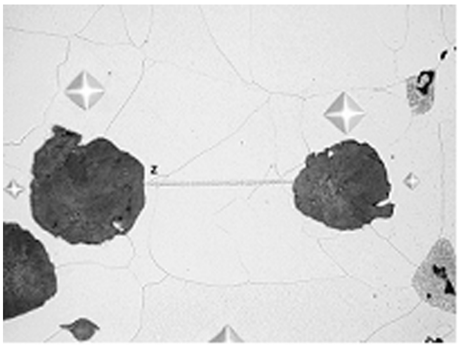

Figure 1: A micro-heterogeneity measurement of ductile cast-iron (the distance between two analysed graphites is 165 μm). Etched by 2 *% nital.*

Slika 1: Meritve mikroheterogenosti duktilne železove litine (razdalja med dvema analiziranima grafitnima zrnoma je 165 μm). Jedkano z 2-odstotnim nitalom.

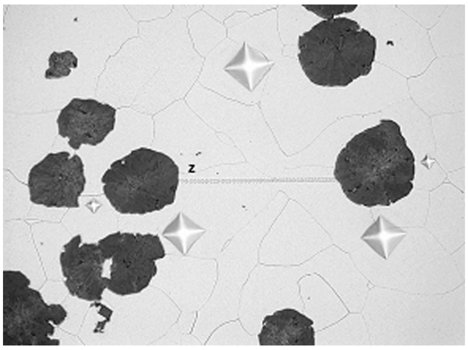

Figure 2: A micro-heterogeneity measurement of ductile cast-iron (the distance between two analysed graphites is 167 μm). Etched by 2 *% nital.*

Slika 2: Meritve mikroheterogenosti duktilne železove litine (razdalja med dvema analiziranima grafitnima zrnoma je 167 μm). Jedkano z 2-odstotnim nitalom.

The results of measurements of the chemical heterogeneity were evaluated statistically and entered into **Table 3** according to the analysed samples (x is the arithmetic mean of the concentration of the element within the measured interval, I_H is the element heterogenity index defined as the quotient of its standard deviation and its arithmetic mean, x_{max} is the maximum concentration of the element within the measured interval and I_H is the segregation index of the element defined by the quotient $I_S = x_{max} / x$.).

The macrostructure between the bottom and upper part of the massive casting shown in **Figures 3** and **4** was very different. The structure of the bottom of a massive casting is practically without foundry defects (see **Figure 3** and **Table 4** – local solidification time 48 s). On the other hand, in the structure of the upper part of the same casting numerous foundry defects, for example shrink hole, cavities and so on were identified (see **Figure 4** and **Table 4** – local solidification time 4572 s).

Table 3: Results of the chemical heterogeneity measurements – x, x_{max} (w/%), I_H, I_S
Tabela 3: Rezultati merjenj kemijske heterogenosti – x, x_{max} (w/%) I_H, I_S

Sample		Element									
		Mg	Al	Si	P	S	Ti	Cr	Mn	Fe	Ni
	r_{ghm} R_{bhm} L_{ghm}	x I_H x_{max} I_S	x I_H x_{max} I_S	x I_H x_{max} I_S	x I_H x_{max} I_S	x I_H x_{max} I_S	x I_H x_{max} I_S	x I_H x_{max} I_S	x I_H x_{max} I_S	x I_H x_{max} I_S	x I_H x_a $I_{S\,x}$
A	28 83 110	0.0652 0.984 0.201 3.083	0.1002 0.597 0.235 2.345	1.500 0.071 1.676 1.117	0.0151 1.805 0.120 7.947	0.0187 1.377 0.103 5.508	0.0118 1.718 0.068 5.763	0.0615 0.571 0.143 2.325	0.101 0.657 0.242 2.393	97.974 0.002 98.634 1.007	0.156 0.538 0.312 2.000
C	36 104 136	0.0387 1.550 0.260 6.718	0.0620 1.048 0.200 3.226	1.562 0.068 1.841 1.179	0.0151 2.306 0.164 10.861	0.0210 1.539 0.107 5.065	0.0065 2.382 0.061 9.385	0.0615 0.751 0.191 3.106	0.0695 0.815 0.193 2.777	97.981 0.002 98.297 1.003	0.184 0.453 0.349 1.897
G	39 109 140	0.0872 1.138 0.363 4.163	0.0761 0.815 0.216 2.838	1.396 0.076 1.650 1.182	0.0119 1.910 0.085 7.143	0.0282 1.264 0.124 4.397	0.0068 2.314 0.079 11.618	0.0959 0.4867 0.2222 2.315	0.107 0.637 0.283 2.645	98.025 0.002 98.491 1.005	0.166 0.513 0.417 2.512

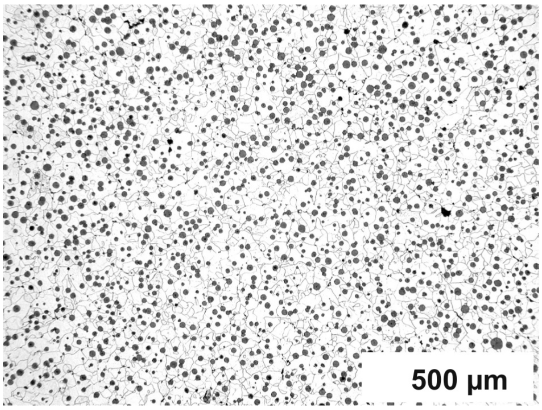

Figure 3: Macrostructure of the massive ductile iron casting in the bottom part is practically without foundry defects. Etched by 2 % *nital*.
Slika 3: Makrostruktura masovnega duktilnega železovega ulitka na spodnjem delu je praktično brez livnih napak. Jedkano z 2-odstotnim *nitalom.*

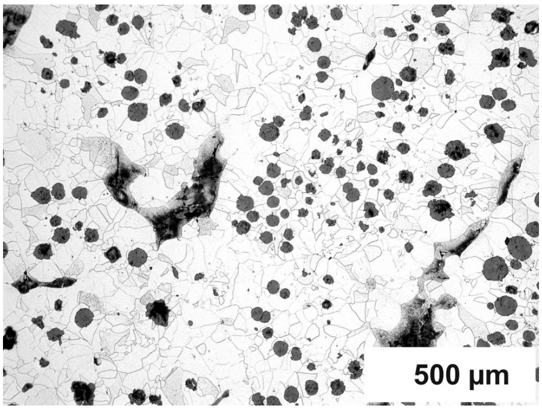

Figure 4: In the macrostructure of the upper part of the same casting is possible to find numerous foundry defects. Etched by 2 % *nital*.
Slika 4: Makrostruktura gornjega dela istega ulitka, kjer je lahko videti številne livne napake. Jedkano z 2-odstotnim *nitalom.*

2.4 Local solidification time

The local solidification times of the selected samples of known coordinates within the casting were calculated using an original in-house 3D model [2] and are given in **Table 2**. The calculation of the liquidus and solidus temperatures for a melt with a composition according to the data in **Table 1**, was performed using special software with the temperature values: 1130 °C (liquidus) and 1110 °C (solidus). The values of the local solidification time θ_{ls} given in **Table 2** therefore relate to the temperature difference between the liquidus and solidus (ΔT_{ls} = 20 °C). If the local solidification time is known, then it is possible to determine the average rate of cooling of the mushy zone as a quotient of the temperature interval and the local solidification time $w_{ls} = \Delta T_{ls} / \theta_{ls}$ /(°C/s).

3 EVALUATION OF RESULTS

It is obvious from the results in **Tables 2 and 3** that in vertical direction from the bottom of the massive casting (sample A: y = 50 mm) to the top (gradually samples C: y = 210 mm and G: y = 450 mm) the characteristic and significant relations are the following:

The average size of the spheroids of graphite, the average size of the cells of graphite and also the average distance between the individual particles of the graphite are all increasing. This relation was confirmed by quantitative metallographic analysis [6].

The chemical heterogeneity within the individual graphite cells is also increasing. The increase in the chemical heterogeneity is reflected most significantly in the increase in the indexes of segregation I_S for magnesium and for titanium, which are increasing in the direction from the bottom of the massive casting to the top in the following order: magnesium I_S^{Mg} = 3.08-to-

-6.72-to-4.16; titanium I_S^{Ti} = 5.76-to-9.39-to-11.62 (**Table 3**).

The local solidification time, which increases from the bottom of the casting to the top – from the value of 48 s more than 50-times (near the centre of the casting) and 95-times (at the top of the massive casting), increases very significantly.

The relationships between the structural characteristics of graphite in the casting 2L and the local solidification time were expressed quantitatively using a semi-logarithmic dependence. Despite the fact that, for the structural characteristics of graphite r_{ghm}, R_{bhm} and L_{ghm}, there are only three pairs of measured values, i.e. (r_{ghm},θ_{ls}), (R_{bhm},θ_{ls}) and (L_{ghm},θ_{ls}), the given dependences can be considered significant. As obvious from the research report [6], the quantitative metallographic analysis covers 49 measured views (with a magnification of 100-times) on each of the three 3D samples. This research can therefore be considered as statistically significant.

The relationship between the radius of the graphite spheroids r_{ghm} and the local solidification time θ_{ls}

$$r_{ghm} /\mu m = 19.08 + 2.274 \ln (\theta_{ls}/s) \tag{1}$$

had been found using the least-squares method. The correlation coefficient $r = 0.99$.

Similarly, the relation

$$R_{bhm} /\mu m = 61.33 + 5.567 \ln (\theta_{ls}/s) \tag{2}$$

was established between the radius of the graphite cells and the local solidification time – with a correlation coefficient of $r = 1.00$, and also between the average distance of graphite particles and the local solidification time there is the relation

$$L_{ghm}/\mu m = 84.50 + 6.586 \ln (\theta_{ls}/s) \tag{3}$$

As far as chemical heterogenity of the measured elements is concerned, an analogous relation was established only for the dependence of the segregation index of titanium on the local solidification time, which has a steadily increasing course from the bottom of the casting (sample A) all the way up to the top (sample G). The relevant relation was expressed in the form of a logarithmic equation:

$$\ln I_S^{Ti} /\mu m = 1.201 + 0.1410 \ln (\theta_{ls}/s) \tag{4}$$

where $r = 0.96$.

4 DISCUSSION

The local solidification time θ naturally affects the mechanical properties of cast-iron, however with regard to the dimensions of the test pieces, it is not possible to assign the entire body a single local solidification time. The samples for the testing of tensile strength were taken from the test-sample of the experimental casting in such a way that one had been taken from under the metallographic sample and the second was taken from above. In this way, the test-samples from along the entire height of the massive casting had been taken and marked: (1A2), (3C4) and (6G7). For example, according to the marking (3C4) test-sample 3 was to be found in experimental casting beneath the metallographic sample C and test-sample 4 above it. The mechanical values determined on these test-samples are arranged in **Table 4**. The last column contains the local solidification times relating to samples A, C and G.

Table 4: Mechanical properties of the samples from experimental casting

Tabela 4: Mehanske lastnosti eksperimentalno ulitih vzorcev

Test-sample		Yield point $R_{p0.2}$/MPa	Tensile strength R_m/MPa	Ductility A_5 /%	Local solidification time* θ_{ls}/s
(1A2)	1	262	388	21.4	48
	2	260	392	24.6	
(3C4)	3	261	394	20.6	2509
	4	266	390	19.4	
(6G7)	6	260	391	14.0	4572

Note: *) metallographic samples A, C, G

Table 4 indicates that in this case the local solidification time θ_{ls} does not affect the yield point $R_{p0.2}$ and the tensile strength R_m of the ductile cast-iron, however, it has significant influence on the ductility A_5. In terms of analytical approximation, the following relationship between the ductility and the local solidification time applies:

$$A_5/\% = 23.399 - 8.1703 (\theta_{ls}/h) \tag{5}$$

where $r = 0.91$. Simultaneously, it could be stated that for four degrees of freedom, which, according to **Table 4**, characterise the six statistically processed pairs (ductility, local solidification time), the correlation coefficient for this level of reliability is 0.917 [8]. In Eq. (5) the ductility is expressed in percentage and the local solidification time in hours. The equation indicates that the reduction in ductility of cast-iron in the state immediately after pouring is – in the first approximation – directly proportional to the square of the local solidification time.

5 CONCLUSION

It can be seen from previous experimentation and the evaluations of the results that led to equations (1) to (5) that – in the general case of the solidification of ductile cast-iron – there could be a dependence of the size of the spheroids of graphite, the size of the graphite cells and therefore even the distance among the graphite particles on the local solidification time, i.e. on the solidification time in which the considered point remains within the *mushy zone*. The described connection with the 3D model of a transient temperature field, which makes it possible to determine the local solidification time, seems to be the means via which it is possible to estimate the differences in structural characteristics of graphite in cast-iron and also the effect of the local solidification time on ductility in the poured casting. It is known that, for example, the density of spheroids of graphite also significantly influences the mechanical properties of cast-iron, especially contraction and ductility, where the influence of the local solidification time on ductility has been verified (**Equation 5**).

The application of the 3D model of the temperature field, together with the known and experimentally and quantitatively verified relation of microstructural characteristics of cast-iron, could become an effective tool for verifying the above relations in cases comprising complex and massive cast-iron castings.

6 REFERENCES

[1] Kavicka, F. et al.: Optimization of the properties and the technology of the production of massive cast-iron castings. Final Research Report for the GAČR Project No. 106/01/1164. VUT-FSI, Institute of Power Engineering, Brno 2003, 68 pages

[2] Dobrovska J., Kavicka F., Stetina J., Stransky K., Heger J.: Numerical models of the temperature field and chemical heterogenity of a concast steel slab. *Proceedings of the 21st Canadian Congress of Applied mechanics CANCAM 2007*, Toronto, Ontario, Canada, June 2007, 384–385

[3] Smrha, L.: Solidification and crystallisation of steel ingots. SNTL, Prague 1983, 305 pages

[4] Chvorinov, N.: *Crystallisation and heterogeneity of steels*. NČSAV, Prague 1954, 381 pages

[5] Kavicka F., Sekanina B., Stetina J., Stransky K., Gontarev V., Dobrovska J.: Numerical optimization of the method of cooling of a massive casting of ductile cast-iron. Materiali in tehnologie/Materials and technology 43 (**2009**) 2, 73–78

[6] Belko, J., Stransky, K.: Analysing Graphite in Cast-iron. Research Report (611–57, 811–28) VTUO Brno, Brno, November 2002

[7] Winkler, Z., Stransky, K.: Heterogeneity of the Compositions of Elements in Ductile Cast-iron Castings. Research Report (811-11-02) VTÚO Brno, Brno, December 2002

[8] Murdoch, J., Barnes, J. A. Statistical Tables for science, engineering, management and business studies. Macmillan, Cranfield 1970, 40 pages

UDK 620.197; 537.39; 539.8
Professional article/Strokovni članek

ISSN 1580-2949
MTAEC9, 44(2)99(2010)

CORRELATION BETWEEN THE CORROSION RESISTANCE AND THE HARDNESS SCATTERING OF STRUCTURAL METALS TREATED WITH A PULSED ELECTRIC CURRENT

KORELACIJA MED ODPORNOSTJO PROTI KOROZIJI IN RAZTROSOM TRDOTE PRI KONSTRUKCIJSKIH MATERIALIH, OBDELANIH S PULZIRANJEM ELEKTRIČNEGA TOKA

Anatoly Babutsky[1], A. Chrysanthou[2], J. Ioannou[2], Ilija Mamuzic[3]
[1]Institute for Problems of Strength, National Academy of Sciences of Ukraine, Timiyazevska 2 str., 01014 Kiev, Ukraine
[2]School of Aerospace, Automotive and Design Engineering, University of Hertfordshire, College Lane, Hatfield, AL10 9AB Herts, UK
[3]University of Zagreb Sisak, Croatia
bai@ipp.kiev.ua

Prejem rokopisa – received: 2009-09-25; sprejem za objavo – accepted for publication: 2009-10-05

The results of corrosion tests of two kinds of structural metals initially treated by a pulsed electric current of high density are presented. According to the data obtained, the treatment influences the corrosion of metals. There is a correlation between the corrosion test results and the hardness scattering of the metals.

Key words: corrosion, hardness scattering, pulse electric current

Predstavljeni so rezultati korozijskih preizkusov za dve vrsti kovin, ki sta bili obdelani s pulziranjem električnega toka z veliko gostoto. Dobljeni rezultati kažejo, da obdelava s tokom vpliva na korozijo kovin. Opredeljena je bila korelacija med rezultati preizkusov korozije in raztrosom meritev trdote.

Ključne besede: korozija, raztros trdote, pulzirajoči električni tok

1 INTRODUCTION

The interest relating to corrosion in structural metals remains high because it is related to considerable financial costs. Corrosion leads not only to a loss of metal, but also to the degradation of its mechanical and physical properties, which decreases the lifetime of components and sometimes leads to catastrophic failure. For example, a majority of failures in oil-field pipes occurs because of corrosion damage, and similar damage may occur in ships and other structures [1,2].

Existing methods of metal and alloy protection from corrosion include the use of coatings with deposition, electrochemical methods of protection (e.g., cathodic protection) and others. However, there is considerable interest in developing new and more effective corrosion-protection methods.

One of the common types of metal and alloy corrosion is electrochemical corrosion, which leads to damage in conductive environments (electrolytic solutions). In general, the electrochemical corrosion mechanism involves the appearance of short-circuited micro-galvanic elements on the metal surface with different values of e.m.f. as a result of the formation of anodic (with low electrode potential) and cathodic (with high electrode potential) zones [3]. These zones are generated by differences in the metal structure, surface roughness, the existence of protective films and other factors. The difference in the metal microstructure (due to a difference of the grain size, composition, crystal anisotropy, the emergence of dislocations on the surface, the presence of impurities, inclusions, non-uniform mechanical stresses) can activate the corrosion processes. The role of mechanical stresses is important because in presence of tensile stresses in the metal, anode zones can appear. These zones evolve to become corrosion centers [4].

It is known that a pulsed electric current (PEC) treatment causes the relaxation of the mechanical stresses in metals [5,6], and also the homogenization of their microstructure [7]. Based upon common considerations, these data can serve as a basis for the creation of a new technology for the corrosion protection of metals.

The structural homogeneity of a metal can be estimated by a measurement of its indentation hardness [8,9]. The specifics of the indentation hardness are based on the existence of a quantity correlation with other mechanical properties (e.g., tensile strength, fatigue limit). Consequently, if a representative array of hardness measurements is obtained, it is possible to assess the variation of the mechanical properties of the metal and its microstructural homogeneity. For example, the authors [9] have shown that the lowest level of hardness scattering corresponded to the metal with the most uniform microstructure in the initial state. On the other hand, the highest hardness scattering was registered for the metal with accumulated damage after long-term performance.

The results of the investigation presented here aim to clarify the possibilities of a PEC treatment to improve the corrosion resistance of steel and an aluminum alloy and also to define a correlation between the corrosion resistance and the hardness scattering in the metals after the treatment.

2 METHOD OF EXPERIMENTAL RESEARCH

Metallic sheet specimens of high-strength low-alloy steel HSLA of 100 mm length, 13 mm width and 1.1 mm thickness and an aluminum alloy 5182 of 100 mm length, 13 mm width and 1.4 mm thickness were used for the investigation (the compositions of the metals are in **Table 1**).

Table 1: Composition of the metals used (mass fraction, *w*/%)
Tabela 1: Sestava uporabljenih kovin (masni delež, *w*/%)

Specimens	w(Mn) /%	w(Mg) /%	w(Ti) /%	w(C) /%	w(S) /%	w(P) /%
Steel HSLA	0.25	–	0.30	0.02	0.02	0.02
Al-alloy 5182	0.3	4.5	–	–	–	–

The corrosion was performed at 35 °C (± 1.5 °C) in a salt-spray chamber using a 5 % NaCl solution (in distilled water) according to the ASTM B117-97. The total time of exposure was 1000 h. The treatment was carried out in hourly cycles that involved sequences of spraying the samples with a fog spray (salt spray) for 10 minutes at a flow rate of 0.7 L/h and 50 min of hot air (drying). The sequence was repeated every hour.

The samples were initially hand cleaned in hot water and further cleaned for 12 min in an ultra-sonic chamber with water at 48 °C. This process took place twice because a change of water was necessary. Then the specimens were washed with propanol and dried for 30 min at 70 °C, weighed and placed in the corrosion salt-spray chamber. At the end of the corrosion test the samples were cleaned in hot water to remove the deposits of salt and then washed with propanol and dried at 70 °C and weighed.

Table 2: Regimes of PEC treatment
Tabela 2: Režimi obdelave z električnim tokom

No.	Steel HSLA	Aluminum alloy 5182
	Current density, j(kA/mm^2)	
1	1.3	1.3
2	1.3	1.3
3	2	2
4	2	2
5	3	3
6	3	3

Remark: specimens No. 1, 3, 5 were treated using three pulses with a 1 min. interval, specimens No. 2, 4, 6 were treated using three pulses with a 3 min. interval

The PEC treatment of the samples was undertaken using a pulsed current generator [10]. Three electric current pulses were passed through each sample with the maximum current density as indicated in **Table 2**.

To obtain reliable values of the metal hardness and exclude the operator's mistakes, a computerized hardness tester COMPUTEST SC (ERNST, Switzerland) was used. The hardness *HRB* was measured before the PEC treatment and after the treatment under an indentation load of 49 N.

3 TEST RESULTS AND THEIR ANALYSIS

The corrosion test results are presented in **Table 3** and in **figures 1 a, 1 b and 2**. The different corrosion behavior of the steel and aluminum alloys must be considered. In the test result analysis on steel, the corrosion products (Fe_2O_3 oxides) flake off the base material causing the reduction of the specimen weight after the corrosion tests, while, in the case of the aluminum alloy, an increase in the specimen weight is observed after the corrosion tests because Al_2O_3 oxides have high adhesion to the base material.

The estimation of the influence of the PEC treatment on specimens corrosion was carried out in two steps. In the first step, the relative change, δ_m, of the weight of each specimen after the corrosion test was calculated,

$$\delta_m \,/\, \% = \frac{m_c - m_0}{m_0} \cdot 100$$

where m_0 and m_c are the weights of the samples before and after the corrosion test, respectively. In the second step, the influence factor of the PEC treatment on the specimen corrosion, k_c, was determined as:

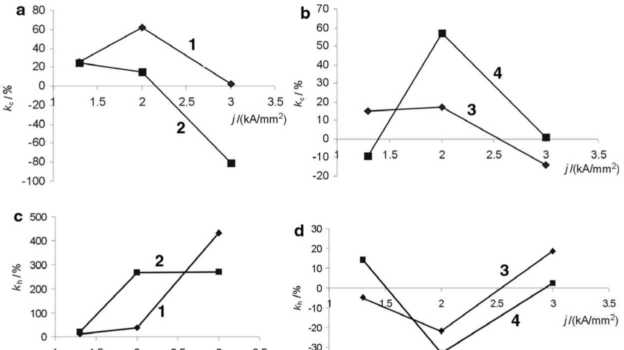

Figure 1: Change of the effect of PEC treatment on metal corrosion k_c (a, b) and hardness scattering k_h (c, d) against the metal (a, c – HSLA steel; b, d – aluminium alloy 5182), density of PEC, and interval between electric current pulses (1, 3 – 1 min interval; 2, 4 – 3 min interval).

Slika 1: Sprememba učinka obdelave z električnim tokom na korozijo kovine k_c (a, b) in raztros trdote k_h (c, d) v odvisnosti od kovine (a, c – konstrukcijsko jeklo; b,d – zlitina aluminija), gostota toka in interval med električnimi pulzi (1, 3 – 1 min interval; 2, 4 – 3 min interval)

$$k_{\mathrm{c}}\ /\ \% = \frac{\left|\delta_{m}^{\mathrm{untreat}}\right| - \left|\delta_{m}^{\mathrm{treat}}\right|}{\left|\delta_{m}^{\mathrm{untreat}}\right|} \cdot 100$$

where $\delta_m^{\mathrm{untreat}}$ is the relative change of the weight of the untreated specimens (the mean value of the 6 specimens in the bottom row in **Table 3**) and $\delta_m^{\mathrm{treat}}$ is the relative change of the weight in percent of the six specimens treated by PEC (**Table 3**).

Table 3: Results of the corrosion tests
Tabela 3: Rezultati korozijskih preizkusov

No. (corresponds to **table 2**)	Steel HSLA		Aluminum alloy 5182	
	After PEC treatment			
	δ_m/%	k_c/%	δ_m/%	k_c/%
1	–0.5224	+26	+0.1217	+15
2	–0.5310	+25	+0.1571	–9
3	–0.2706	+62	+0.1188	+17
4	–0.60 10	+15	+0.0614	+57
5	–0.6890	+2	+0.1640	–14
6	–1.2729	–81	+0.1426	+1
Without PEC treatment				
Mean for 6 specimens	δ_{m}/%		δ_{m}/%	
	–0.7050		+0.1437	

The corrosion test results suggest that the PEC treatment with the above regimes substantially influences the behavior of the investigated metals. The treatment causes considerable deceleration of the corrosion processes for both the HSLA and aluminum alloy 5182. Here, the results presented show that the regimes of the PEC treatment with maximum effect exist.

Table 4: Results of indentation tests
Tabela 4: Rezultati meritev trdote

No. (corresponds to table 2)	Steel HSLA σ_μ	Steel HSLA k_h/%	Aluminum alloy 5182 σ_μ	Aluminum alloy 5182 k_h/%
1 – untreated	0.0152	+11	0.0615	–5
1 – treated	0.0168		0.0584	
2 – untreated	0.0120	+20	0.0501	+14
2 – treated	0.0144		0.0572	
3 – untreated	0.0153	+39	0.0751	–22
3 – treated	0.0212		0.0587	
4 – untreated	0.0171	+267	0.0847	–33
4 – treated	0.0627		0.0566	
5 – untreated	0.0186	+431	0.0531	+19
5 – treated	0.0986		0.0630	
6 – untreated	0.0150	+271	0.0512	+2
6 – treated	0.0557		0.0525	

The indentation test results are presented in **Table 4** and in **Figures 1 c, 1 d**. On average, 120 measurements of hardness per condition (treated and untreated) were fulfilled for each specimen. The results were processed and a relative value σ_μ, with σ as the standard deviation and μ as the hardness average were calculated for each specimen and condition. Then the influence factor of the PEC treatment on the metal hardness scattering, k_{h}, was determined, as presented below:

$$k_h = \frac{\sigma_\mu^{\mathrm{treat}} - \sigma_\mu^{\mathrm{untreat}}}{\sigma_\mu^{\mathrm{untreat}}} \cdot 100\%$$

The indentation test results demonstrate the sensitivity of the hardness scattering to the regimes of PEC treatment and the corrosion resistance. The PEC-treated HSLA sample sets 4 and 5 showed a lower increase of the corrosion resistance than the sample sets 1, 2 and 3, and the set 6 showed an increase of corrosion (**Table 3** and **Figure 1 a**). At the same time, the samples sets 4, 5 and 6 exhibited a substantial increase in the hardness scattering (**Table 4** and **Figure 1 c**). In the case of the aluminum alloy 5182, the effect of the PEC treatment on the corrosion resistance is mixed as shown in **Table 3** and **Figure 1 b** with the PEC-treated sample sets 1, 3 and 4 with a lower corrosion intensity, sets 2 and 5 with a stronger corrosion, while the values for set 6 are practically similar. At the same time, the PEC-treated sample sets that corroded less (1, 3 and 4), also exhibited a lower level of scattering of the hardness value, indicating a more homogeneous composition and microstructure (**Table 4** and **Figure 1 d**). On the other hand, sets 2 and 5 corroded more, but showed a higher degree of scattering of the hardness data, implying a less uniform structure and composition.

Macrographs of the surface appearance of the investigated HSLA specimens after the corrosion tests are

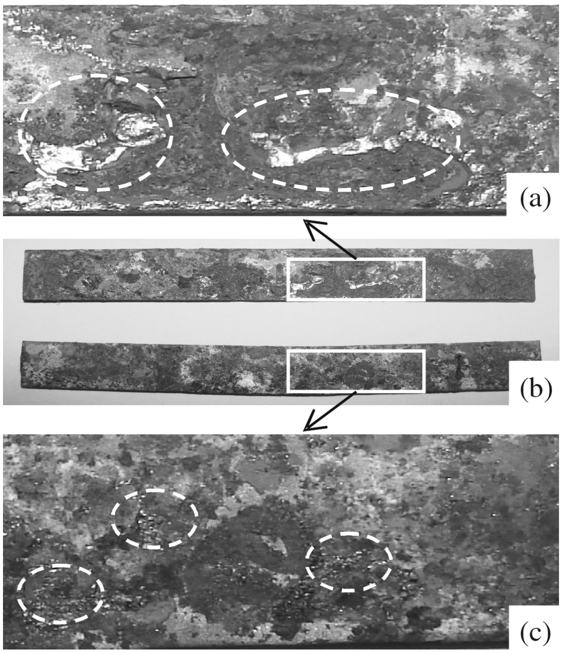

Figure 2: Surface appearances of HSLA steel specimens after corrosion tests: a, b (top photo) – metal in initial condition; b (bottom photo), c – after PEC treatment

Slika 2: Videz površine konstrukcijskega jekla po korozijskem preizkusu: a, b (zgornja slika) – kovina pred preizlkusom; b (slika spodaj), c – po obdelavi s tokom presented in **Figure 2** (the difference in the appearance of the treated and untreated specimens in the case of the aluminum alloy specimens is visibly insignificant). A substantial difference in the corrosion damage of the alloy surface took place for the HSLA specimens; in the case of the specimens without the PEC treatment, zones with selective, localized corrosion are visible in **Figure 2 b** (top) and more obviously it is visible in the areas bordered by the dashed lines in **Figure 2 a**. The PEC treatment was observed to cause weaker, more uniform and homogeneous corrosion on the whole surface of specimen, see **Figure 2 b** (bottom). Only small pittings are visible there, see the areas bordered by the dashed lines in **Figure 2 c**.

The obtained results may be related to the different microstructure and the surface homogeneity of the treated and untreated specimens. The differences may arise during the production of the sheet with the cold-working that builds up non-uniform residual stresses. On the other hand, the PEC treatment may relieve these stresses, providing a more homogeneous material.

4 CONCLUSIONS

The results of the investigation have shown that the PEC treatment influences the corrosion behavior of structural metals. Based on these observations, the following conclusions can be drawn:

The regimes of the PEC treatment causing the deceleration of the corrosion with maximum effect exist for both the HSLA and aluminum alloy 5182.

A correlation between the corrosion resistance and the hardness scattering of the PEC-treated metals exists. The specimens with the lower hardness scattering show the better corrosion resistance.

As a result of the PEC treatment, the corrosion on the surface of HSLA steel samples became smaller and more homogenous and the zones of localized corrosion observed on the untreated samples are absent on the surface of PEC-treated HSLA.

The investigation was based on one sample per variant of PEC treatment. Further research will be carried out using more samples, aiming to accumulate experimental data on the influence of the PEC treatment on the characteristics of the corrosion of structural metals, as well as to investigate the reasons and physical mechanisms of such effects.

5 REFERENCES

[1] Emi, H.; Kumano, A.; Baba, N.; et al.: *A study on life assessment of ships and offshore structures (Part 1: basic study)*, J. Soc. Nav. Archit. Jpn., 169 (**1991**), 443–454

[2] Emi, H.; Yuasa, M.; Kumano, A.; et al.: *A study on life assessment of ships and offshore structures (3rd report: corrosion control and condition evaluation for a long life service of the ship)*, J. Soc. Nav. Archit. Jpn., 174 (**1993**), 735–744

[3] Isaev, N. I.: *Theory of corrosion processes*, Publishing house *Metallurgy*, Moscow 1997 (in Russian)

[4] http://www.cathedral.ru/cathedra/num2/demidov (in Russian)

[5] Baranov, Y. V., Troitskiy, O. A., et al.: *Physical bases of electro-pulse and electro-plastic treatments and new materials*, Publishing house *MGIU*, Moscow 2001 (in Russian)

[6] Stepanov, G.; Babutsky, A.; Krushka, L.: *Metal behavior under passage of impulse electric current*, J.Phys. IV France, 110 (**2003**), 577–582

[7] Stepanov, G. V.; Babutsky, A. I.; Chyzhyk G. V.: *Estimation of impulse electric current influence on strength of metallic materials*, Metals science and treatment (Metaloznavstvo ta obrobka metaliv), (**2005**) 2, 64–68 (in Ukrainian)

[8] Lebedev, A. A.; Muzyka, N. R.; Volchek N. L.: *Determination of damage accumulated in structural materials by the parameters of scatter of their hardness characteristics*, Strength of Materials 34 (**2002**) 4, 312–321

[9] Lebedev, A. A.; Muzyka, N. R.; Volchek N. L., et al.: *Monitoring of current state of pipe metal in active gas pipelines. Experimental method and results*, Strength of Materials, 35 (**2003**) 2, 122–127

[10] Stepanov, G. V.; Babutskii, A. I.; Mameev, I. A.: *High-density pulse current-induced unsteady stress-strain state in a long rod*, Strength of Materials, 36 (**2004**) 4, 377–381